Università degli studi di Genova

Scuola di Scienze M.F.N.

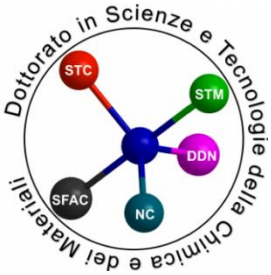

Scuola di dottorato in Scienze e Tecnologie della Chimica e dei Materiali

Curriculum Scienza e Tecnologia dei Materiali

XXXII ciclo

Marzo 2020

Title:

Large-Area Plasmonics on Self-Organized Wrinkled Nanopatterns

PhD Candidate: Matteo Barelli

Supervisor: Prof. Francesco Buatier de Mongeot

Coordinator: Prof. ssa Adriana Saccone / Prof. ssa Renata Riva

Contents

Introduction

The focus of my PhD project consisted in the development of self-organized, large area, industrially scalable physical methods based on wrinkling instabilities to nanopattern and functionalize tunable plasmonic polymeric polydimetilsyloxane (PDMS) and solid-state glass surfaces, both transparent, non-toxic and cheap materials, for applications of significant technological interest in photonics and bio-sensing.

This research topic can be located in the framework of the vast, emerging field of nanotechnology. When one of the dimensions of matter is restricted to the nanoscale (10^{-9} m), extraordinary properties, radically different from their bulk counterparts, may manifest under both the physical and chemical point of view. This is due to the increase in the ratio of surface-to-volume atoms and to electronic quantum confinement. Being able to control and tailor matter morphology at the nanoscale can thus lead to the study and engineering of the most diverse and striking properties and effects, which are of high interest in a multitude of scientific and technological interdisciplinary fields. A plethora of nano-research topics emerged in the past couple of decades, investigating a broad range of properties and applications, e.g. mechanic and tribologic [1,2], biologic and medical [3–5], magnetic [6,7], electric [8], optic and photonic [9–11].

Of primary relevance to my PhD research work is the field of plasmonics, which studies the interaction between electromagnetic radiation and metallic/semiconductive nanostructured systems [10–15]. Plasmonic materials enable the concentration and manipulation of electromagnetic fields well beyond the diffraction limit through resonant and coherent oscillations of free electrons. Plasmonic resonances enhance photonic absorption and scattering efficiency, allowing for the far field manipulation of electromagnetic wavefront propagation, a crucial property for the development of optical and photonic applications [16,17]. In addition, plasmonic excitation enables the near field concentration of electromagnetic energy into subwavelength nanoscopic volumes, greatly enhancing light-matter interaction. This property enables several applications, e.g. the enhancement of photonic absorption in thin film optoelectronic devices [18,19], refractive index sensing, subwavelength microscopy [11] and enhanced optical non-linear emission [20]. Moreover, the near field localization of electromagnetic energy can enhance by several orders of magnitude the weak signal of bio-molecules in different spectroscopic techniques [21], allowing for the

development of Surface Enhanced Raman Spectroscopy (SERS) [22], Surface Enhanced Infrared Absorption (SEIRA) [23] and Plasmon Enhanced Fluorescence (PEF) [24]. Plasmons can also decay non-radiatively, generating hot electrons which can be injected from the plasmonic material into a semiconductor through a Schottky barrier formed at their interface. This allows for the engineering of optoelectronic devices which can operate at sub-bandgap photon energies [25,26], a very promising property in particular for photocatalysis [27] since typical semiconductors with photocatalytic properties (e.g. TiO_2) show high band gaps which cause most sun light to be lost.

In nanotechnology in general, and in plasmonics in particular, sought-for peculiar properties and effects are intimately related to matter size and geometry [28]. A great deal of effort is constantly dedicated by the scientific community and high-tech companies to the development of nanofabrication techniques, which can be classified into two distinct families generally referred as (i) top-down and (ii) bottom-up fabrication methods. Top-down, lithographic techniques rely on the selective removal of matter to acquire strictly controlled morphological designs. A laser or a particle beam may be focused and maneuvered to directly remove matter from a surface (e.g. Focused Ion Beam - FIB, Laser nanolithography), or impress a resist (e.g. Electron Beam Lithography - EBL), with nanometric resolution in a serial production process. In this way masks can be produced, enabling parallel nanofabrication techniques such UV/X-ray and nanoimprint lithographies. Scanning probe techniques such as STM (Scanning Probe Microscopy) and AFM (Atomic Force Microscopy) have also been used to directly manipulate matter at the nanoscale. However, the fabrication costs of top down approaches are generally hefty, they are slow and limited to small areas (in the order of μm^2). This limits their implementation mainly to prototyping and research laboratories. Another important purpose of nanotechnology, along with the investigation of extraordinary properties and effects, would be the huge economic and environmental gain made possible by extreme miniaturization. The development of cost effective, fast and large area nanofabrication techniques is thus a crucial, fundamental need for industry and real world applications. Under this point of view, great promise is shown by so called bottom-up, self-organized nanofabrication methods. In this case no geometrical order is imposed from above like in top-down methods. On the contrary, a given physiochemical system spontaneously reacts to an external macroscopically controlled stimulus with a self-organized modification of its morphology at the nanoscale. For example, a temperature controlled chemical reaction can change the nanoscale morphology of the involved chemical species (e.g. block co-polymers) creating

characteristic patterns [29]. Other examples of bottom-up nanofabrication methods are molecular beam epitaxy, physical and chemical vapor deposition, colloidal chemistry and, particularly relevant to my PhD thesis, ion beam sputtering [30,31] and nanoscale wrinkling of soft matter [32]. The great challenge with bottom-up approaches is refining the degree of control on the self-organization process, which is highly dependent on the physio-chemical properties of the materials involved and the stimulus applied, to achieve a controlled and homogeneous tailoring of its nanoscale morphological features. The main advantages of bottom-up methods reside on cheap, fast, large area (in the order of cm^2 or more) parallel processes, naturally suited to industrial scaling.

The approach I followed to nanopattern PDMS samples is based on soft-matter buckling instabilities which lead to the formation of wrinkles on the surface when a stiff, harder layer compared to the bulk is formed on top of the material [32]. This is a very well know phenomenon also in the macroscopic world, which leads to the formation of isotropic wrinkles, e.g. in dry paint or desiccated fruit. It is indeed possible to induce tunable nanoscale wrinkles in plasma treated and ion bombarded PDMS surfaces [33,34], and to impose a uniaxial anisotropic morphology to the wrinkles by applying a pre-stretching to the samples [35]. This leads to the fabrication of quite ordered and monodisperse nanopatterned templates over cm^2 areas. These uniaxial modulations are the ideal platform for the confinement of plasmonic nanowire (NW) arrays by grazing angle Au thermal deposition. The NW transverse Localized Surface Plasmon Resonances (LSPR) of dipolar and multipolar character can be widely and easily tuned from the visible to the infrared range, from 600 to 1200 nm, by playing with the width and height (aspect ratio) of the NW. This makes these samples ideal candidates for SERS bio-sensing, where it's desirable to use less energetic pump lasers to match the surface plasmonic resonance, in order to avoid molecules damage and fluorescence background.

To nanostructure glass surfaces I employed an approach based on Ion Beam Sputtering (IBS). It is known that the irradiation of crystalline and amorphous metallic and dielectric surfaces by defocused low energy ion beams may lead to the formation of large area uniaxial rippled morphologies [30,31]. Normally, however, these modulations show very low vertical dynamic (few nm) and aspect ratio (in the order of 0.1 - defined as height divided by width of the ripples), making the controlled confinement of plasmonic structures a challenging task. Recently, in the laboratory

which hosted me, a variant of the IBS nanopatterning technique has been developed, in which a glass sample is kept at high temperatures during ion irradiation [36]. Surprisingly under these conditions the glass substrate develops a buckling instability which is commonly associated with soft matter, greatly enhancing the vertical dynamic (in the range of 100 nm), aspect ratio (now in the order of 1) and long range order of soda-lime uniaxial rippled templates. Moreover, the glass ripples show an asymmetric faceted profile and very well defined slopes. I exploited such enhanced large area nanopatterned IBS glass substrates as self-organized templates to implement four radically different plasmonic functionalizations:

(a) Au NW arrays can be confined on the glass uniaxial modulations by grazing angle thermal deposition, in analogy with the PDMS experiments previously described. Engineering of the NW LSP resonance this time is limited to the visible range due to the narrower morphologic tunability of the IBS glass templates compared to the PDMS case. However, due to the stronger thermal stability of the solid state soda-lime glass, it's possible to grow a dielectric SiO_x layer by Radio Frequency Sputtering and then another Au layer over the original NW matrix, creating self-organized anisotropic metal-insulator-metal (MIM) structures in the so-called gap plasmon configuration [37]. To my knowledge this is the first demonstration of fully self-organized, large area nanostructures of this kind. These MIM "nanosandwiches" show two hybrid plasmonic modes, a higher energy electric mode and a lower energy magnetic mode, the latter showing exceptional near field enhancement factors for both the electric and magnetic component of incident radiation. The magnetic mode is tunable in the near-infrared (NIR) range of the spectrum making the nanosandwiches again excellent candidates for large area SERS bio-sensing applications.

(b) I exploited the unique rippled morphology of the glass template to confine an array of Au NW on one side of the ripples profile and an array of Ag NW on the other, with a dielectric SiO_x gap layer separating them. In this way I achieved an interdigitated array composed of alternating of Ag/Au nanowires with uniaxial orientation over the whole sample area (cm^2). Due to the spectral detuning of the transverse LSPR of Au and Ag arrays, and to their alternating tilt, upon normal incidence illumination with a polychromatic spectrum a certain band of frequencies of an incoming polychromatic wavefront will be scattered to the left side of the sample while another band of frequencies will be scattered to the right [38]. This spatial separation of wavelengths is called color

routing, a property of fundamental importance for a broad range of photonic applications. Normally this effect is achieved through the complex engineering of the near field interference of optical modes of single or multi-element optical antennas [16,39], and this typically requires the use of high cost top-down fabrication methods to be achieved. The innovative approach I explored offers instead an easily tunable, bottom-up, large area approach to flat-optics color routing, based on the unique opportunity to build cross-tilted antenna arrays supported on the faceted glass templates.

(c) By reducing the ion dose during the IBS induced buckling of soda-lime glass substrates and by tailoring the ion beam illumination geometry it's possible to create templates characterized by particularly short uniaxial ripples. On these templates it's thus possible to confine Au antennas with reduced length below 1 μm which show a transverse LSPR in the visible range and a longitudinal LSPR mode in the IR range [40]. We exploited the longitudinal IR resonance to enhance the infrared absorption signal of octadecanethiol (ODT) monolayers in SEIRA measurements. These samples showed a remarkable SEIRA signal, comparable or better than that of lithographic nanoantennas, and signal homogeneity extended over their whole macroscopic area, a crucial feature in the constant search for effective and reproducible large area SEIRA platforms.

(d) A continuous thin nanometric film of Au is grown on the surface of the hot IBS glass nanopattern. The slanted grating properties of the asymmetric nanorippled surface enables the unidirectional excitation of a tunable, counter-propagating Surface Plasmon Polariton (SPP) when the sample is illuminated with polychromatic radiation in the visible and NIR range, both under normal incidence as well as under tilted conditions. The sample has been tested in SERS experiments with methylene blue molecules, showing remarkable gains in the order of 10^3, for both 638 nm and 785 nm pump lasers [41]. Normally, tunable SPP are excited over dielectric/metal interfaces by complex experimental geometries (e.g. Kretschmann and Otto configurations) or lithographic made gratings. I investigated the remarkable opportunity to achieve tunable SPP excitation, interesting for a broad range of applications, at the interface metal/dielectric interface of Au thin films grown on our self-organized, large area, sub-wavelength asymmetric soda-lime gratings.

The thesis is organized as follows:

Chapter 1 will concisely outline the basic theoretical background supporting my experimental work. The first section of the chapter will describe the theory behind the self-organized, large area, wrinkling based nanopatterning techniques I employed to fabricate nanorippled PDMS and soda-lime glass surfaces for plasmonic functionalization. The second section of the chapter will present the theoretical basics about localized surface plasmons and propagating surface plasmon polaritons, with an emphasis on the effects having the most relevant technological implications and stronger correlation with the different plasmonic functionalities at core of the following thesis experimental chapters.

Chapter 2 will describe the self-organized, large area nano-wrinkling of PDMS surfaces by air plasma treated pre-stretched samples. The morphological analysis and the optical characterization of the tunable plasmonic properties of the Au NWs grown on top of the uniaxial nanorippled PDMS modulations are presented. The mechanical characterization of the Au/PDMS nanowire arrays against tensile strain will be also investigated.

Chapter 3 will illustrate the fabrication of MIM (metal-insulator-metal) plasmonic "nanosandwiches" on top of the wrinkling-enhanced IBS soda-lime glass templates, by a natural lithography method. The nanosandwiches and rippled glass template morphology are investigated by means of atomic force microscopy and scanning electron microscopy. The chapter will then describe the tunable plasmonic and field enhancement properties of the hybrid plasmonic modes that the dimers can sustain, in the so called gap-plasmon configuration.

Chapter 4 will describe bimetallic antenna arrays grown on top of the IBS nanorippled glass surfaces. This chapter will introduce a novel approach to color routing, that is the wavelength selective directional scattering of an incoming electromagnetic field, by the development of unique self-organized fabrication technique. The optical scattering properties and directivity of the bimetallic antennas arrays are investigated along with the morphological features of the large-area, self-organized, passive plasmonic color router.

Chapter 5 will introduce a modified wrinkling enhanced IBS process compared to the other chapters, which allows to guide the growth of shorter Au nanowires supporting two localized plasmonic modes; a transversal mode in the visible range and a longitudinal mode in the infrared range. The optical characterization of these plasmonic modes is presented along with the

morphological analysis of the nanostructured glass template and short Au antennas. The chapter will also discuss striking results obtained in SEIRA measurements of octadecanethiol monolayers grown on the samples.

Chapter 6 will discuss how the IBS rippled soda-lime glass templates can operate as large area, subwavelength, quasi-1D blazed gratings for the unidirectional excitation of propagating Surface Plasmon Polaritons, when a thin metallic film is grown on top of them. The optical characterization of the samples demonstrating the SPP attribution is presented and discussed along with the comparison of experimental data with a simple theoretical model.

References:

(1) Bruschi, L.; Fois, G.; Pontarollo, A.; Mistura, G.; Torre, B.; Buatier de Mongeot, F.; Boragno, C.; Buzio, R.; Valbusa, U. Structural Depinning of Ne Monolayers on Pb at T < 6.5 K. *Physical Review Letters* **2006**, *96* (21). https://doi.org/10.1103/PhysRevLett.96.216101.

(2) Buzio, R.; Boragno, C.; Biscarini, F.; Buatier De Mongeot, F.; Valbusa, U. The Contact Mechanics of Fractal Surfaces. *Nature Materials* **2003**, *2* (4), 233–236. https://doi.org/10.1038/nmat855.

(3) Ertorer, E.; Vasefi, F.; Keshwah, J.; Najiminaini, M.; Halfpap, C.; Langbein, U.; Carson, J. J. L.; Hamilton, D. W.; Mittler, S. Large Area Periodic, Systematically Changing, Multishape Nanostructures by Laser Interference Lithography and Cell Response to These Topographies. *Journal of Biomedical Optics* **2013**, *18* (3), 035002. https://doi.org/10.1117/1.JBO.18.3.035002.

(4) Goldberg, M.; Langer, R.; Jia, X. Nanostructured Materials for Applications in Drug Delivery and Tissue Engineering. *Journal of Biomaterials Science, Polymer Edition* **2007**, *18* (3), 241–268. https://doi.org/10.1163/156856207779996931.

(5) Pedraz, P.; Casado, S.; Rodriguez, V.; Giordano, M. C.; Mongeot, F. B. de; Ayuso-Sacido, A.; Gnecco, E. Adhesion Modification of Neural Stem Cells Induced by Nanoscale Ripple Patterns. *Nanotechnology* **2016**, *27* (12), 125301. https://doi.org/10.1088/0957-4484/27/12/125301.

(6) Bisio, F.; Moroni, R.; Buatier de Mongeot, F.; Canepa, M.; Mattera, L. Isolating the Step

Contribution to the Uniaxial Magnetic Anisotropy in Nanostructured Fe / Ag (001) Films. *Physical Review Letters* **2006**, *96* (5). https://doi.org/10.1103/PhysRevLett.96.057204.

(7) Moroni, R.; Sekiba, D.; Buatier de Mongeot, F.; Gonella, G.; Boragno, C.; Mattera, L.; Valbusa, U. Uniaxial Magnetic Anisotropy in Nanostructured C o / C u (001) : From Surface Ripples to Nanowires. *Physical Review Letters* **2003**, *91* (16). https://doi.org/10.1103/PhysRevLett.91.167207.

(8) Ellmer, K. Past Achievements and Future Challenges in the Development of Optically Transparent Electrodes. *Nature Photonics* **2012**, *6* (12), 809–817. https://doi.org/10.1038/nphoton.2012.282.

(9) Yu, N.; Capasso, F. Flat Optics with Designer Metasurfaces. *Nature Materials* **2014**, *13* (2), 139–150. https://doi.org/10.1038/nmat3839.

(10) Gramotnev, D. K.; Bozhevolnyi, S. I. Plasmonics beyond the Diffraction Limit. *Nature Photonics* **2010**, *4* (2), 83–91. https://doi.org/10.1038/nphoton.2009.282.

(11) Kawata, S.; Inouye, Y.; Verma, P. Plasmonics for Near-Field Nano-Imaging and Superlensing. *Nature Photonics* **2009**, *3* (7), 388–394. https://doi.org/10.1038/nphoton.2009.111.

(12) Lal, S.; Link, S.; Halas, N. J. Nano-Optics from Sensing to Waveguiding. *Nature Photonics* **2007**, *1* (11), 641–648. https://doi.org/10.1038/nphoton.2007.223.

(13) Maier, S. A.; Atwater, H. A. Plasmonics: Localization and Guiding of Electromagnetic Energy in Metal/Dielectric Structures. *Journal of Applied Physics* **2005**, *98* (1), 011101. https://doi.org/10.1063/1.1951057.

(14) Muhlschlegel, P. Resonant Optical Antennas. *Science* **2005**, *308* (5728), 1607–1609. https://doi.org/10.1126/science.1111886.

(15) Maier, S. A. *Plasmonics: Fundamentals and Applications*; Springer: New York, 2007.

(16) Shegai, T.; Chen, S.; Miljković, V. D.; Zengin, G.; Johansson, P.; Käll, M. A Bimetallic Nanoantenna for Directional Colour Routing. *Nature Communications* **2011**, *2* (1). https://doi.org/10.1038/ncomms1490.

(17) Curto, A. G.; Volpe, G.; Taminiau, T. H.; Kreuzer, M. P.; Quidant, R.; van Hulst, N. F. Unidirectional Emission of a Quantum Dot Coupled to a Nanoantenna. *Science* **2010**, *329* (5994), 930–933. https://doi.org/10.1126/science.1191922.

(18) Atwater, H. A.; Polman, A. Plasmonics for Improved Photovoltaic Devices. *Nature Materials* **2010**, *9* (3), 205–213. https://doi.org/10.1038/nmat2629.

(19) Atwater, H. A.; Polman, A. Erratum: Plasmonics for Improved Photovoltaic Devices. *Nature Materials* **2010**, *9* (10), 865–865. https://doi.org/10.1038/nmat2866.

(20) Kauranen, M.; Zayats, A. V. Nonlinear Plasmonics. *Nature Photonics* **2012**, *6* (11), 737–748. https://doi.org/10.1038/nphoton.2012.244.

(21) Anker, J. N.; Hall, W. P.; Lyandres, O.; Shah, N. C.; Zhao, J.; Van Duyne, R. P. Biosensing with Plasmonic Nanosensors. *Nature Materials* **2008**, *7* (6), 442–453. https://doi.org/10.1038/nmat2162.

(22) Nie, S. Probing Single Molecules and Single Nanoparticles by Surface-Enhanced Raman Scattering. *Science* **1997**, *275* (5303), 1102–1106. https://doi.org/10.1126/science.275.5303.1102.

(23) Neubrech, F.; Huck, C.; Weber, K.; Pucci, A.; Giessen, H. Surface-Enhanced Infrared Spectroscopy Using Resonant Nanoantennas. *Chemical Reviews* **2017**, *117* (7), 5110–5145. https://doi.org/10.1021/acs.chemrev.6b00743.

(24) Li, J.-F.; Li, C.-Y.; Aroca, R. F. Plasmon-Enhanced Fluorescence Spectroscopy. *Chemical Society Reviews* **2017**, *46* (13), 3962–3979. https://doi.org/10.1039/C7CS00169J.

(25) Brongersma, M. L.; Halas, N. J.; Nordlander, P. Plasmon-Induced Hot Carrier Science and Technology. *Nature Nanotechnology* **2015**, *10* (1), 25–34. https://doi.org/10.1038/nnano.2014.311.

(26) Knight, M. W.; Sobhani, H.; Nordlander, P.; Halas, N. J. Photodetection with Active Optical Antennas. *Science* **2011**, *332* (6030), 702–704. https://doi.org/10.1126/science.1203056.

(27) Clavero, C. Plasmon-Induced Hot-Electron Generation at Nanoparticle/Metal-Oxide Interfaces for Photovoltaic and Photocatalytic Devices. *Nature Photonics* **2014**, *8* (2), 95–103. https://doi.org/10.1038/nphoton.2013.238.

(28) Muskens, O.; Christofilos, D.; Fatti, N. D.; Vallée, F. Optical Response of a Single Noble Metal Nanoparticle. *Journal of Optics A: Pure and Applied Optics* **2006**, *8* (4), S264–S272. https://doi.org/10.1088/1464-4258/8/4/S28.

(29) Cheng, J. Y.; Mayes, A. M.; Ross, C. A. Nanostructure Engineering by Templated Self-Assembly of Block Copolymers. *Nature Materials* **2004**, *3* (11), 823–828. https://doi.org/10.1038/nmat1211.

(30) Valbusa, U.; Boragno, C.; Mongeot, F. B. de. Nanostructuring Surfaces by Ion Sputtering. *Journal of Physics: Condensed Matter* **2002**, *14* (35), 8153–8175. https://doi.org/10.1088/0953-8984/14/35/301.

(31) Chan, W. L.; Chason, E. Making Waves: Kinetic Processes Controlling Surface Evolution during Low Energy Ion Sputtering. *Journal of Applied Physics* **2007**, *101* (12), 121301. https://doi.org/10.1063/1.2749198.

(32) Genzer, J.; Groenewold, J. Soft Matter with Hard Skin: From Skin Wrinkles to Templating and Material Characterization. *Soft Matter* **2006**, *2* (4), 310. https://doi.org/10.1039/b516741h.

(33) Park, H.-G.; Jeong, H.-C.; Jung, Y. H.; Seo, D.-S. Control of the Wrinkle Structure on Surface-Reformed Poly(Dimethylsiloxane) via Ion-Beam Bombardment. *Scientific Reports* **2015**, *5* (1). https://doi.org/10.1038/srep12356.

(34) Kim, P.; Hu, Y.; Alvarenga, J.; Kolle, M.; Suo, Z.; Aizenberg, J. Rational Design of Mechano-Responsive Optical Materials by Fine Tuning the Evolution of Strain-Dependent Wrinkling Patterns. *Advanced Optical Materials* **2013**, *1* (5), 381–388. https://doi.org/10.1002/adom.201300034.

(35) Barelli, M.; Repetto, D.; de Mongeot, F. B. Infrared Plasmonics via Self-Organized Anisotropic Wrinkling of Au/PDMS Nanoarrays. *ACS Applied Polymer Materials* **2019**, *1* (6), 1334–1340. https://doi.org/10.1021/acsapm.9b00138.

(36) Giordano, M. C.; de Mongeot, F. B. Anisotropic Nanoscale Wrinkling in Solid-State Substrates. *Advanced Materials* **2018**, *30* (30), 1801840. https://doi.org/10.1002/adma.201801840.

(37) Giordano, M. C.; Longhi, S.; Barelli, M.; Mazzanti, A.; Buatier de Mongeot, F.; Della Valle, G. Plasmon Hybridization Engineering in Self-Organized Anisotropic Metasurfaces. *Nano Research* **2018**, *11* (7), 3943–3956. https://doi.org/10.1007/s12274-018-1974-3.

(38) M. Barelli, A. Mazzanti, M.C. Giordano, G. Della Valle, F. Buatier de Mongeot. Large Area Color Routing via Cross-Polarized Detuned Plasmonic Nanoantennas. *submitted to Nature Communications*

(39) Li, J.; Verellen, N.; Vercruysse, D.; Bearda, T.; Lagae, L.; Van Dorpe, P. All-Dielectric Antenna Wavelength Router with Bidirectional Scattering of Visible Light. *Nano Letters* **2016**, *16* (7), 4396–4403. https://doi.org/10.1021/acs.nanolett.6b01519.

(40) M. C. Giordano, M. Tzschoppe, M. Barelli, J. Vogt, C. Huck, F. Canepa, A. Pucci, F. Buatier de Mongeot, Self-Organized Nanorod Arrays for Large-Area Surface Enhanced Infra-Red Absorption. *Accepted by ACS Applied Materials & Interfaces*

(41) M. Barelli, P.G. Gucciardi, F. Buatier De Mongeot, Large area blazed nanogratings for unidirectional Surface Plasmon Polariton excitation and SERS detection. *in preparation*

In particular, the following publications are related to my thesis work:

- Barelli, M.; Repetto, D.; de Mongeot, F. B. Infrared Plasmonics via Self-Organized Anisotropic Wrinkling of Au/PDMS Nanoarrays. *ACS Applied Polymer Materials* **2019**, *1* (6), 1334–1340. https://doi.org/10.1021/acsapm.9b00138.

- Giordano, M. C.; Longhi, S.; Barelli, M.; Mazzanti, A.; Buatier de Mongeot, F.; Della Valle, G. Plasmon Hybridization Engineering in Self-Organized Anisotropic Metasurfaces. *Nano Research* **2018**, *11* (7), 3943–3956. https://doi.org/10.1007/s12274-018-1974-3.

- M. Barelli, A. Mazzanti, M.C. Giordano, G. Della Valle, F. Buatier de Mongeot. Large Area Color Routing via Cross-Polarized Detuned Plasmonic Nanoantennas. *submitted to Nature Communications*

- M. C. Giordano, M. Tzschoppe, M. Barelli, J. Vogt, C. Huck, F. Canepa, A. Pucci, F. Buatier de Mongeot, Self-Organized Nanorod Arrays for Large-Area Surface Enhanced Infra-Red Absorption. *Accepted by ACS Applied Materials & Interface*

- M. Barelli, M.C. Giordano, P.G. Gucciardi, F. Buatier De Mongeot, Large area blazed nanogratings for unidirectional Surface Plasmon Polariton excitation and SERS detection. *in preparation*

CHAPTER 1

Wrinkling assisted nanofabrication and plasmonics fundamentals

This chapter will concisely describe the basic theoretical background supporting the experimental work of my thesis. As already mentioned in the Introduction, one of the main focus of my PhD program is the nanofabrication of plasmonic surfaces following bottom-up, self-organized, large area methods. I focused my work on the nanopatterning of rigid, inorganic soda-lime glass and flexible, organic polydimetilsiloxane (PDMS) surfaces for plasmonic functionalization. Both PDMS and soda-lime glass are materials owning crucial features for several applications such as transparency, non-toxicity and low cost.

The first section of this chapter will describe the theory behind the nanofabrication techniques I employed to fabricate PDMS and soda-lime surfaces ideal for plasmonic confinement. I will start by briefly recalling a simple model describing the formation of wrinkling instabilities. I will show how this very common, and typically undesired, phoenomenon in the macroscopic world can indeed be exploited for the bottom-up, large area micro- and nano- patterning of PDMS surfaces and soft matter in general. I will then proceed by describing the most authoritative model on the nanopattering of amorphous surfaces by Ion Beam Sputtering (IBS). It will be shown how the wrinkling instabilities typically associated with soft organic matter can improve the IBS method to fabricate enhanced, beyond the IBS state of the art, inorganic soda-lime glass nanorippled templates. I thoroughly exploited these exceptional templates, developed by the lab which hosted me, for plasmonic confinement throughout my PhD work.

The second section of the chapter will present the theoretical basics required for the description of localized surface plasmons and propagating surface plasmon polaritons, with an emphasis on the effects which are exploited in the most relevant technological applications, and on the phenomena which are more strongly correlated with the different plasmonic functionalities at the core of the thesis experimental chapters.

1.1 – Wrinkling: from the macro to the nanoscale

Wrinkled organic surfaces are very common in the macroscopic world. Some of the most obvious

examples are wrinkles found on the surface of dry fruits, plastic sheets and, unfortunately, aging human skin. Macroscopic wrinkling is normally associated with mechanical failures or other undesired degradation processes. However, at the micro- and nano-scale, wrinkled surfaces offer outstanding functionalization opportunities, of high interest for a huge number of research and technological fields from photonics, to super-hydrophobic surfaces, electronics, and biology [1,2].

A great deal of effort is thus dedicated by the scientific community to develop methods capable of controllably tailoring wrinkles size and morphology both at the micro- and nano-scale level. All wrinkling processes share the same fundamental mechanisms: the presence of a thin, harder, compressively stressed layer on top of a softer, compliant bulk substrate. Wrinkling is commonly associated with soft organic matter, as it's very uncommon to find such elastic mismatches in inorganic solid state materials. However, the first serious studies about wrinkling instabilities emerged in the aerospace field. During WWII allied forces conceived the first airplane supported by wings with a "sandwich" design, that is, wings made up by an inner core of softer and lighter balsa wood covered by a more robust plywood external layer (Havilland ''Mosquito''aircraft) [1]. Since then the "sandwich" design of wings became a technology standard leading to the development of composite layered materials: wrinkling instabilities constitute a very delicate weak point of this technology, thus the need to carefully evaluate them and to develop important studies.

In the past decades a simple continuum model has been used to describe wrinkling instabilities over a skin layer resting on top of an elastic, compilant foundation [1–3]. Let's consider a surface skin layer having width *w* and thickness *h*, strongly bounded to a semi-infinite elastic foundation (Fig. 1).

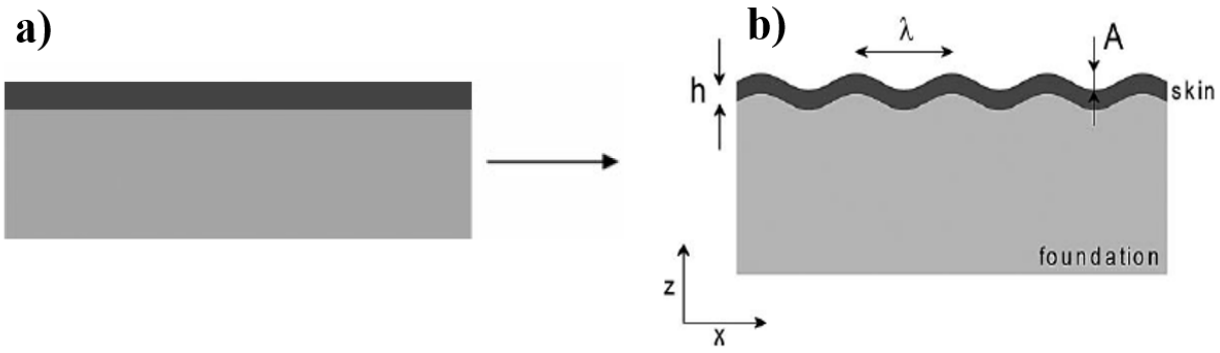

Figure 1 *– Sketch of a compressively stressed skin layer on a compilant elastic foundation for a*

a) relaxed and b) wrinkled system.

If shear stress between skin and bulk is negligible the compressive force in the skin layer is:

$$F = E_s \left[\left(\frac{\pi}{\lambda} \right)^2 \frac{wh^3}{3(1-v_s^2)} + \frac{\lambda E_f w}{4\pi(1-v_f^2)E_s} \right] \quad (1)$$

Where E_f and E_s are the Young moduli of the foundation and skin respectively, v_f and v_s are their Poisson ratios and λ is the wavelength of the sinusoidal profile that the skin layer shows along the direction of the compressive force acting on the elastic bulk. When *F* exceeds the critical value F_C wrinkling instabilities occur. The wrinkles wavelength, obtained imposing $\left(\frac{dF}{d\lambda}\right) = 0$, is:

$$\lambda_c = 2\pi h \left(\frac{(1-v_f^2)E_s}{3(1-v_s^2)E_f} \right)^{1/3} \quad (2)$$

The wavelength of the wrinkles thus depends on the thickness of the skin layer and on the mechanical properties of both skin and foundation, while it is independent from the applied stress/strain. The wrinkle period is thus very small for small h and E_s/E_F and can be shrinked down to few nm, while it increases steeply with h and E_s/E_F up to macroscopic scale values**.** For the wrikles amplitude *A*, the following relation is found:

$$A = h\sqrt{\frac{\varepsilon_{strain}}{\varepsilon_c} - 1} \quad (3)$$

Where:

$$\varepsilon_c = 0.25 \left(\frac{3(1-v_s^2)E_f}{(1-v_f^2)E_s} \right)^{2/3} \quad (4)$$

ε_c is the crital strain which activates the buckling instability. The amplitude A of the wrinkles thus indeed depends both on the mechanical properties of the materials and on the externally applied strain parallel the skin and bulk interface, expressed as the relative deformation ε_{strain}. This model is actually in good agreement with experiments only for very small ε_{strain} in the order of 5% or less. For greater deformations the wrinkles wavelength λ_c becomes proportional on the applied prestrain ε_{strain} [4]. The model can of course become much more complex in the case of different

geometries, beyond the planar thin film case, and for anisotropic materials and strains.

Of particular interest to this thesis is the micro- and nano- wrinkling of polydimethylsiloxane (PDMS), a low cost, transparent, non-toxic, hydrophobic material with captures the interest of a plethora of nanotechnology fields. Isotropic, brain-like nanowrinkling can be achieved on PDMS by irradiating its surface with ion plasmas [5]. The ion bombardment modifies the surface due to the cleavage of Si−CH3 groups and the formation of a denser and harder SiOX-rich, glass-like, skin layer [6,7]. This provides both the stiffness mismatch between skin and bulk, and the thin enough hardened skin layer required to activate nanoscale buckling instabilities. By introducing a uniaxial prestrain during the ion bombardment of the PDMS surface it's possible to accurately tune the height and wavelenght of the wrinkles and, even more importantly, to impose an anisotropic uniaxial wrinkle morphology over macroscopic areas [8]. During my PhD work I followed this approach to create anisoptropic nanowrinkled PDMS templates, which are the ideal candidates for the confinement of self organized, large area plasmonic nanowire arrays, endowed with remarkable range order and IR optical properties [9]. The work on this topic is presented in chapter 2 of this thesis.

1.2 Ion Beam Sputtering of amorphous surfaces

Ion Beam Sputtering (IBS) is a self-organized, bottom-up technique which enables large area anisotropic nanopatterning of surfaces by a defocused ion beam. The processes of erosion, diffusion and redeposition can induce the formation, in a few minutes, of nanoripples on a macroscopic surface area illuminated by the ion beam. These nanorippled morphologies recall the ones formed by wind over sand or clouds. The ripples morphology and size strongly depend on variables such as ion dose, angle of incidence of the ion beam, temperature, ion energy and surface chemical composition and structure (amorphous, crystalline, poly-crystalline) [10–12]. In view of technological developments arising from my work, I stress that ion sources employed in my lab covered uniformly a diameter of few cm, while already available commercial ion sources can illuminate spots extending well over 0.5 m, thus making realistic the upscaling of the results in real world applications.

Over the course of my PhD thesis I employed IBS to nanopattern amorphous, soda-lime glass

substrates. The first part of this chapter will be dedicated to the Bradley-Harper model, a theoretical classic describing the IBS of amorphous surfaces [13]. Then we will proceed showing some recent results obtained in the lab which hosted me, exploring the role of temperature in the IBS of soda-lime glass. It has been found that wrinkling instabilities, commonly associated with soft matter as already mentioned in the previous section of this chapter, can enhance the ripples vertical dynamic of IBS nanopatterned rigid soda-lime glasses at high temperatures, a counter-intuitive concept which defies conventional thermodynamic interpretation [14]. During my PhD thesis I extensively exploited this novel wrinkling-assisted IBS technique to produce nanostrucured templates for different plasmonic functionalizations presented in the next chapters of this thesis.

1.2.1 – Bradley-Harper model for the IBS of amorphous surfaces

The effects of ion bombardment are strongly dependent of the bonds between the surface atoms. Models describing the process are thus different in the case of amorphous, crystalline and poly-crystalline materials. In this chapter the model proposed in 1988 by Bradley and Harper regading the IBS of amorphous surfaces will be described [13].

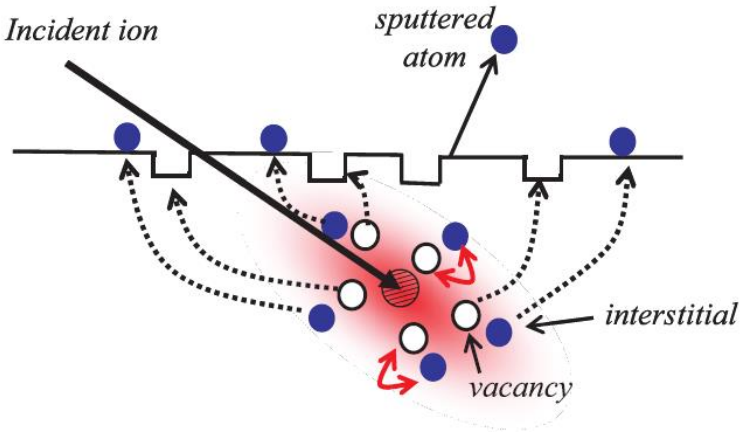

Figure 2 – *Sketch of the different events produced by ions impact on the surface.*

Upon impact, ions transfer their energy to surface atoms through direct and secondary collisions. A little fraction of the atoms involved in the collision will leave the surface and their number per incident ion is defined as *sputtering yield, Y*. A larger amount of atoms gets closer to the surface, these atoms acquire mobility but they don't get expelled. Their number per incident ion is called *adatom yield*. This quantity depends on the erosion rate and thus on the dissipated power at each

surface coordinate. In the low ion energy limit it is assumed that an ion impacting on the surface in a point O (Fig. 3) will dissipate an energy distributed over a Gaussian profile:

$$E(\vec{r}) = \frac{\varepsilon}{\frac{3}{(2\pi)2\alpha\beta^2}} e^{\frac{(z+a)^2}{2a^2}} e^{-\frac{x^2+y^2}{2\beta^2}} \quad (5)$$

Where *a* is the average penetration depth of the ions, α and β are the longitudinal and lateral dimensions, respectively, where the energy ε is dissipated. For simplicity a 1+1 dimensional system is considered (Fig. 3); the direction of the incoming ions lies on the plane formed by the h and y axes, at an angle θ with respect to the h axis, normal to the surface. The angle φ is formed between the incoming ions direction and the local normal to the surface, which is assumed to show a local curvature radius R_x, positive for convex surfaces and negative for concave ones.

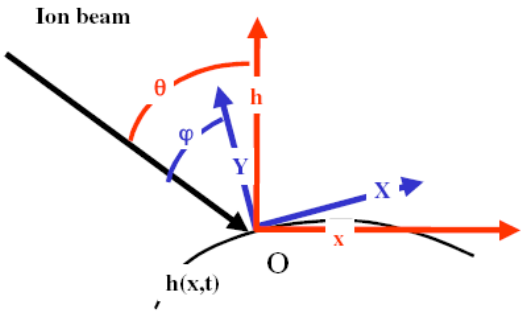

Figure 3 *– Sketch of the curved surface and of the coordinates system in the 1+1 dimensional model.*

The sputtering yield is then:

$$Y(\varphi) = \frac{nv(\varphi,R_x)}{J\cos\varphi} \quad (6)$$

Where J is the incoming ion flux and n is the atomic density of the amorphous material. In the limit $R_x >> a$ the modulations of the height profile $h(x,y)$ evolve slowly with respect to the penetration depth of the incoming ions. The erosion rate can be approximated to the first order:

$$v(R_x, R_y, \varphi) = \frac{J}{n} Y_0(\varphi)\left[\cos\theta - \Gamma_x(\varphi)\frac{a}{R_x} - \Gamma_y(\varphi)\frac{a}{R_y}\right] \quad (7)$$

$Y_0(\varphi)$ is the sputtering yield of a flat surface ($R_x = \infty$). The factors Γ_i account for the local

curvature dependence of the erosion speed, and they are function of α, β and φ. If α=β then:

$$\Gamma_{x,y} = \sin^2(\varphi)\sin^2\left(\frac{\varphi}{2}\right) - \cos^2\left(\frac{\varphi}{2}\right) \quad (8)$$

The coefficients $\Gamma_i(\varphi)\frac{a}{R_i}$ in Eq. 7 are positive for crests and negative in valleys. The erosion rate and the sputtering yield are thus maximum in the valleys, in agreement with experimental evidence. It is however necessary to account for the diffusion of adatoms and vacancies which opposes to erosion, trying to minimize free energy by flattening the surface. The diffusion coefficient D is a function of temperature (Arrhenius law):

$$D = D_0 e^{-\frac{E_{att}}{kT}} \quad (9)$$

The Bradley-Harper model, accounting for both erosive and diffusive processes, allows to describe the time dependent morphological evolution of the ion bombarded surface:

$$\frac{\partial h}{\partial t} = -v_0(\theta) + \frac{\partial v_0(\theta)}{\partial \theta}\frac{\partial h}{\partial x} + v_x(\theta)\frac{\partial^2 h}{\partial x^2} + v_y(\theta)\frac{\partial^2 h}{\partial y^2} - K\nabla^2(\nabla^2 h) + \eta(x,y,t) \quad (10)$$

In this differential equation $v_0(\theta) = \frac{J}{n}Y_0(\theta)\cos\theta$ quantifies the erosion rate of a flat surface, θ is the fixed angle formed between the incident ions direction and the surface normal and $v_i(\theta) = \frac{Ja}{n}Y_0(\theta)\Gamma_i$ quantifies the contibution by the local surface curvature. The coefficient K depends upon the free energy per unit area γ, the atoms per unit area which diffuse through the surface and the diffusivity D:

$$K = \frac{2D\gamma\sigma}{n^2 k_b T} \quad (11)$$

η is a Gaussian white noise funtion which accounts for the stocastical distribution of ion impacts. The competition between erosive and diffusive terms in Eq. 10 leads to the formation of ripples on the amorphous surface. The model predicts the ripples wavevector to be parallel with respect to the ion direction under the critical angle θ_c, and a perpedicular wavector for grazing angles larger than θ_c. These conclusion are in agreement with a large set of experimental data. Moreover, the model predicts the wavelength of the ripples:

$$\lambda_{i=}2\pi\sqrt{2K/|v_i|} \quad (12)$$

Where i is the direction in which the relative v_i is the highest. The model also predicts and an exponential increase of the ripples height with time. The Bradley-Harper model shows a good agreement with experiments as long as they are performed at low ion doses. For high ion doses the ripples height gets close the ripples width; the low amplitude approximation on which the model is based doesn't hold anymore. In this case the increase in high is much more intense than the model's predictions, and also the ripples width increases in time while it's supposed to be constant in the model [15]. For ion near normal incidence angles a random orientation of mounds should in principle be observed while in practice one predominantly observes the occurrence of ion induced smoothing due to ballistic effects (downward momentum transfer from the ions to the surface atoms), which is neglected in the simplest form of the BH equation. Many evolutions of the Bradley-Harper theory have been proposed in the past decade, adding new terms in Eq. 10 to account for experimental deviations from the model predictions [16]. In particular, the compressive stress on the surface caused by high ion doses is quite relevant, and causes the ripples heigh growth rate to increase [17,18].

1.2.3 – Wrinkling-assisted hot Ion Beam Sputtering of soda-lime glass

IBS of amorphous surfaces at room temperature leads to the development of low ripples (in the order of 1-10 nm) and quite disordered patterns [11]. This low aspect ratio (in the order of 0.1, defined as ripples heigh divided by their width) ripples are not the ideal cadidates for the confinement of well tailored plasmonic structures. Over the last years, in the lab which hosted me, an IBS based process has been developed to produce enhanced nanopatterned soda-lime glass surfaces, in the regime of incident ion angles lower than θ_c. One of the most striking results is the observation that fixing the soda-lime glass temperature near it's glass transition threshold during the IBS process leads to an enhanced ripples vertical dynamic (higher by an order of magnitude, increasing their aspect ratio to about 1), to a higher degree of long range morphological order and to an overall faster nanopatterning process. This is a counter-intuitive result, as one would expect that increasing the temperature would lead to the flattening of the surface, not to higher roughness. It's been found that this phenomenon is compatible with temperature activated wrinkling instabilities, that enhance the IBS nanopatterning of glass with a mechanism typically associated to soft matter. Moreover, the nanoripples show well defined facets, with selected slopes, opening

unique functionalization opportunities [14]. These cheap and transparent templates endowed with high aspect ratio anisotropic nanoripples are excellent candidates for well controlled plasmonic functionalization. In the following chapter I will show and comment the most relevant features of these glass nanorippled templates which I routinely fabricated to support most of the plasmonic functionalizations I will present in the following chapters of the thesis.

Effect of temperature and ion dose

AFM topographies of Fig. 4a, b, d refer to different IBS experiments performed on soda-lime glass, where all the parameters were fixed except for temperature. The ion energy (Ar+) is 800 ev, the incident ion beam angle with respect to the sample surface is 35° and the ion fluency was set at 10^{19} ions/cm^2 (corresponding to an hour long experiment). It can be clearly seen how the ripples elongation and degree of lateral coordination increase with temperature, reaching a maximum for the 880 K sample (Fig. 4d). The wavelenght λ and RMS roughness of the structures *w* monotonically increase with temperature to reach a remarkable maximum around 790 K, and then they start to decrease (Fig. 4c).

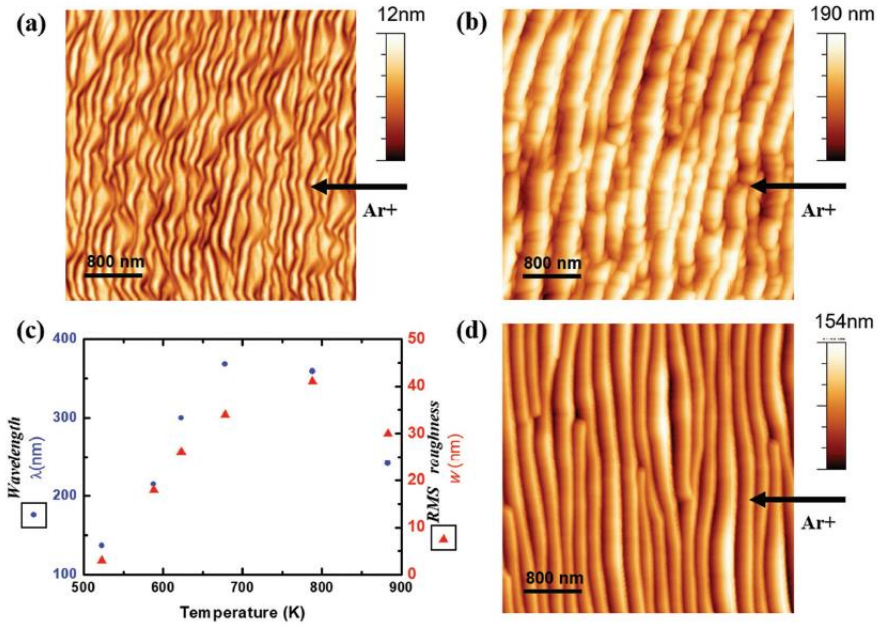

Figure 4 – *a, b, d) AFM topographies of IBS nanorippled soda-lime glass at T=520 K, T= 680 K and T=880 K, respectively, for sputtering time t=3600 s and angle of incedence of the ion beam θ=35 °. c) RMS roughness w (red triangles) and wavelength λ (blue dots) of the rippled patterns*

as a function of the sample temperature.

For temperatures under 600 K we get very low ripples with typical wavelenght λ=140 nm and RMS roughness *w*=3 nm; typical values of room temperature state of the art experiments. Heating the substrate over 600 K, keeping all the other conditions fixed, leads to the amplification of the vertical dynamic of the ripples of more than an order of magnitude as can be clearly seen by the comparison of the AFM topographies of the 520 K (Fig. 4a) and 680 K (Fig. 4b) samples, with ripples aspect ratio approaching unity. This suggest that raising temperature activates additional instabilities which enhance the IBS nanopatterning process, instead of leading to the flattening of the surface as prevailing thermodynamical arguments would suggest. To investigate the issue experiments as a function of the ion dose at the fixed temperature of 680 K have been performed.

In figure Fig. 5a and Fig. 5b the ripples wavelenght λ and RMS roughness *w* are respectively plotted for experiments performed as a function of time at 680 K (red triangles) and at 520 K (blue dot).

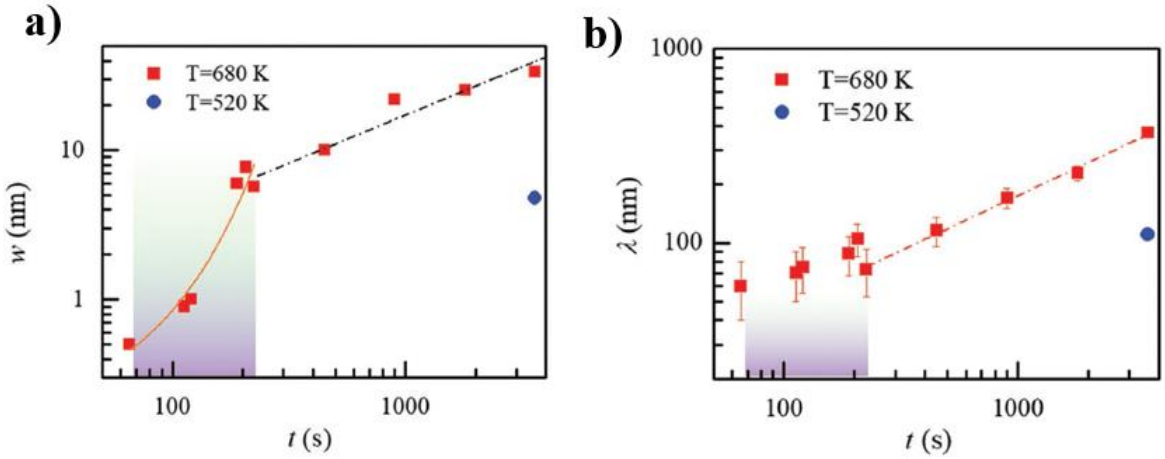

Figure 5 *– a) RMS roughness w and b) wavelength λ of the ripple patterns plotted as a function of sputtering time.*

The first thing to underline is that at high T a RMS roughness comparable to the low T case is reached about an order of magnitude faster. Considering the same sputtering time t=3600s, in the high T case the RMS roughness is about an order of magnitude higher compared to the low T case. For the high T case when the sputtering time increases from 65 s to 207 s, *w* increaes by more than an order of magnitude from 0.5 to 7.7 nm. The RMS roughness then evolves following the exponential relation $w_{(t)} = w_0 \times t^{rt}$, where w_0=0.14 nm and growth rate $r = 1.8 \times 10^{-2} s^{-1}$

(orange line in Fig. 5a). In the same time interval, the ripples wavelength λ remains essentially constant at λ=70±20 nm after the initial pattern formation. This behaviour is in agreement with the Bradley-Harper model in the limit of small vertical amplitudes. After t=200 s the trend starts to follow a power law for both *w* and λ of the form $w_{(t)} = w_0 \times t^{\alpha}$ and $\lambda_{(t)} = w_0 \times t^{\gamma}$, with α=0.6±0.1 and γ=0.57±0.2. The small amplitude approximation doesn't hold anymore and additional non linear terms start to influence the process. As α and γ are compatible within error this means the aspect ratio of the ripples is essentially preserved in the non-linear regime, as sputtering time increases. Also, these coefficients show a value which is almost doubled compared to room temperature experiments [15].

Solid state wrinkling effects unveiled

These experiments showed how the morphology enhancement due to high temperature is caused mainly in the early stages of the IBS experiment, when the RMS roughness grows exponentially with time. This observation is compatible with the activation of wrinkling instabilities as an additional patterning mechanism acting in synergy with ion bombardment. As I commented extensively in section 1.1, wrinkling instabilities typically manifest in soft matter when a compressively stressed surface layer is formed on top of a compilant substrate. It is known that Ar+ bombardment can create a compressively stressed surface layer in soda-lime glasses**,** by depleting the surface of Na ions, while enriching it of Ca ions [19]. This modified, hardened layer, can extend over a depth *h* which can reach up to 15 nm due to high temperature conditions, well beyond the Ar +ions penetration depth of about 3 nm for 800 eV of energy in soda-lime glass [20]. The dramatic viscosity drop of the glass bulk, from 10^{19} to 10^{10} Pa, when temperature increases in the 600-800 K range, closer to the glass transition threshold, provides the other fundamental ingredient of wrinkling instabilities i.e. the presence of a compliant substrate on which efficient mass transport toward the surface is enabled**.** Using the simple continuum model already discussed in section 1.1 it's possible to calculate the typical wavelenght of the glass wrinkles under the previous assumptions:

$$\lambda_c = 2\pi h \left(\frac{(1-\nu_f^2)E_s}{(1-\nu_s^2)E_f}\right)^{1/3} \quad (13)$$

Where *h* is the compressively stressed layer thickness, ν_s and ν_f are the Poisson ratios of the

surface skin layer and bulk respectively, while E_s and E_f are their Young moduli. For *h*=15 nm, $v_s = 0.2196$, $v_f = 0.2081$, $E_s = 7.40 \times 10^{10}$ Pa, and $E_f = 6.40 \times 10^{10}$ Pa [21] a characteristic ripples wavelengh $\lambda_c \approx 60$ nm is found. The order of magnitude of this value is in good agreement with the experimental wavelength λ=70±20 nm, measured for high temperature experiments in the early stages of ion irradiation (Fig. 5a) near the end of the BH linear regime. Ion irradiation experiments were also performed on alkali-free borosilicate glass substrates and no pattern enhancement could be achieved increasing the substrate temperature. No compressively stressed surface layer could be formed by the ion bombardment due to the absence of alkali ions and, due to higher glass transition threeshold, no mass transport from the bulk could be activated in the temperature range explored for soda-lime glasses.

Amorphous glass ripples faceting

As previously mentioned, in the late stages of the nanopattering process the ripples profile evolves into an asymmetric saw-tooth shape which shows highly selected facets slopes. This is surprising because ripples faceting is normally observed in IBS experiments only for crystalline materials. This effect can be clearly seen in the AFM ripples line profiles plotted in Fig. 6a for different sputtering times. The black profile (top panel) corresponds to t=207 s of irradiation and shows a rounded profile, while the blue curve (t=1800 s) presents the characteristical asymmetric sawtooth profile. In Fig. 6b we report the slopes histograms derived by the analysis of AFM topograpies for different sputtering times, to follow the time evolution of the ripples facets.

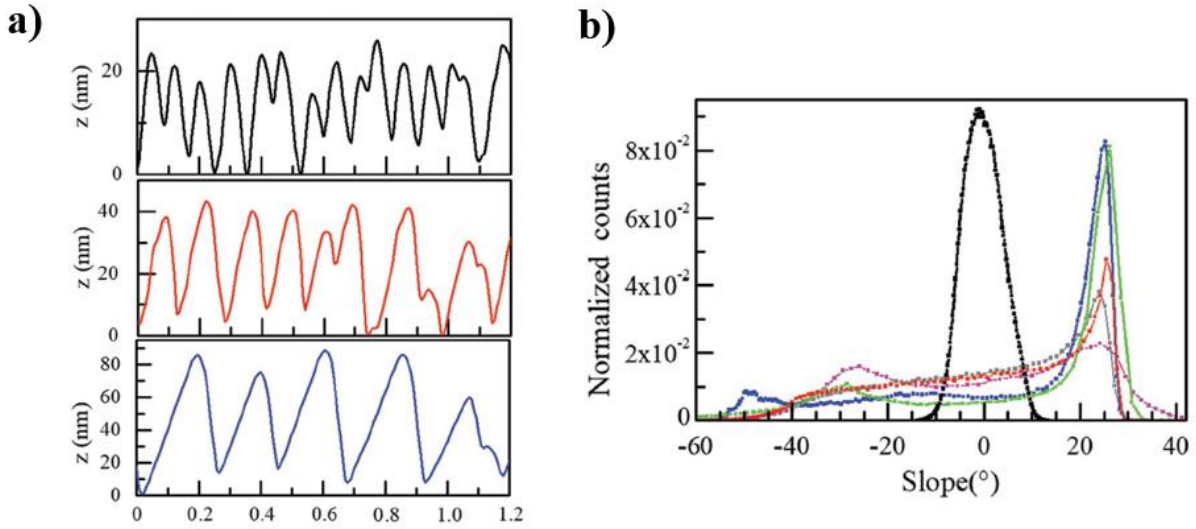

Figure 6 - *a) AFM line profiles for increasing sputtering times: t = 207 s (black line), t = 450 s*

(red line), t = 1800 s (blue line). b) Histograms of slopes with respect to the average plane for differente sputtering times: black line (t =121 s), pink line (t =207 s), grey line (t =225 s), red line (t =450 s), blue line (t =1800 s), green line (t =3600 s). All the experiments where perfomed at T=680 K and θ=35°.

A t=120 s (black curve) we observe a unimodal gaussian distribution peaked at 0°. The average slope is below 5°, corresponding to very shallow ripples. At t=207 s (pink curve) the distribution remarkably broadens in the -40°/+30° range. When time is increased beyond the linear regime, starting from t=225 s (grey curve), a characteristic slope peak is formed at 25° which continues to grow with ion dose (red and blue curves for t=450 s and t=1800 s respectively). This striking feature is caused by the preferential growth of tilted facets which face the opposite direction with respect to the ion incidence. The ripple ridges directly facing the ion beam form very steep but less selected slopes peaked at about 50°. Tip convolution effects may lead to an underestimation of such steep grooves.

This faceted ripples growth in amorphous glass is not predicted by the Bradley-Harper model and defies simple interpretation. Recently, a theoretical model has been proposed predicting the evolution of faceted ripples in amorphous substrates for ions low angle of incidence [22]. In particular, in analogy to our experimental observations, the model predicts the evolution of asymmetric saw-tooth profiles with the steeper ridges facing the ion beam. While quantitatively the model is not consistent with experiments, the qualitative agreement is remarkable and will stimulate further theoretical work.

Nonetheless these faceted, high aspect ratio glass nanorippled templates represent the ideal candidate for large area functionalization with plasmonic nanostructures and beyond.

1. 3 Plasmonics fundamentals

The field of plasmonics, which constitutes a major part of the larger field of nanophotonics, investigates the subwavelength confinement of electromagnetic fields through resonant oscillations of conductance electrons plasmas. Plasmonics can be generally understood exclusively by classical physics arguments and has been formally described as early as 1900 by Gustav Mie

[23]. In this chapter the theoretical basics of the two most important plasmonic phoenomena will be briefly treated, underlining their most important features with respect to this thesis work and to their main technological implications. First *Localized Surface Plasmons* (LSP) will be described, which are standing, non-propagating modes excited over subwavelenght nanostructures by direct illumination. These plasmons have been indirectly known since antiquity; gold and silver nanoparticles with LSP resonances in the visible range are responsible for the bright colors of Roman and middle ages stained glass windows and manufacts (e. g. the famous Lycurgus cup), due to the increase of absorption and scattering cross sections associated with LSP resonances. Then I will proceed describing *Surface Plasmon Polaritons* (SPP), propagating, dispersive electromagnetic modes confined at the interface between a conductive and a dielectric material. This plasmonic mode can't be excited directly by an incident electromagnetic field and particular strategies have to be adopted, as will be shown in the following chapters.

1.3.1 Localized surface plasmons

In this chapter dedicated to Localized Surface Plasmons first we will show how these non-propagating resonant modes arise simply by considering the scattering problem of a subwavelenght, spherical, conductive nanoparticle in a homogeneous oscillating electromagnetic field. Using the so called quasi-static approximation we will show how the nanosphere plasmonic resonant frequency depends only on the chemical composition of the conductive nanoparticle material and the sorrounding medium electronic properties. The electric near field confinement and amplification due to the plasmonic resonance, a crucial aspect in sight of technological applications, will be described along with the enhancement of the nanoparticle scattering and absorption cross sections. Then we will show how changing the shape of the nanoparticle enables tunable, multiple plasmonic modes. Lastly we will consider how bigger particles, relaxing the quasi-static approximation, change the picture by introducing retardation/depolarization effects.

Spherical particles – near field enhancement and scattering of the incident electric field

If a nanoparticle shows a subwalenght diameter compared to the incident electromagnetic radiation ($\lambda <<< d$), their interaction can be analysed in the framework of the so-called quasi static model.

This approximation implies that the phase of the incident electromagnetic field is considered constant over the whole nanoparticle volume. The problem thus becomes electrostatic and time dependence can be treated separetely [24].

Let's consider an homogeneous and isotropic sphere of radius a, placed at the origin of the electrostatic field $E = E_0\hat{z}$. The sorrounding medium is isotropic and non-absorbing, with dielectric constant ε_m. The electric field lines are parallel to the z axis at a sufficient distance from the sphere. The dielectric function of the sphere is described by the complex function $\varepsilon_{(\omega)}$.

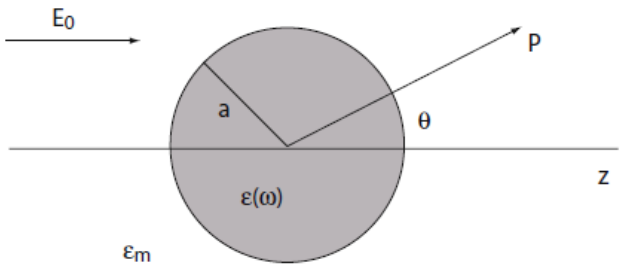

Figura 7 – Sketch of a nanosphere in a homogenous electric field.

The Laplace equation for the electrostatic potential $\nabla^2\Phi = 0$ must be solved to compute the electric field $E = -\nabla\Phi$. Laplace equation solutions read as follows for the sphere internal and external potential, respectively:

$$\Phi_{in} = -\frac{3\varepsilon_m}{\varepsilon+2\varepsilon_m}E_0 r\cos\theta \tag{14}$$

$$\Phi_{out} = -E_0 r\cos\theta + \frac{\vec{p}\cdot\vec{r}}{4\pi\varepsilon_0\varepsilon_m r^3} \tag{15}$$

Where $\vec{p}$ is the dipole moment of the spherical nanoparticle:

$$\vec{p} = 4\pi\varepsilon_0\varepsilon_m a^3 \frac{\varepsilon-\varepsilon_m}{\varepsilon+2\varepsilon_m}\vec{E}_0 \tag{16}$$

a is the radius of the sphere. Let's introduce a new quantity, the nanosphere electric polarizability:

$$\alpha = 4\pi a^3 \frac{\varepsilon-\varepsilon_m}{\varepsilon+2\varepsilon_m} \tag{17}$$

Then $\vec{p}$ reads:

$$\vec{p} = \varepsilon_0 \varepsilon_m \alpha \vec{E}_0 \tag{18}$$

The sphere polarizability (Eq. 17) shows a maximum when the quantity $|\varepsilon_{(\omega)} + 2\varepsilon_m|$ is minimum. If the imaginary part of $\varepsilon_{(\omega)}$ is small or nearly constant near resonance (an imaginary part of $\varepsilon_{(\omega)}$equal to 0 would imply a divergence), the polarizability maxima is verified when:

$$\mathrm{Re}[\varepsilon_{(\omega)}] = -2\varepsilon_m \tag{19}$$

A localized surface plasmon resonance is excited when the so-called Frölich condition (Eq. 19) is satisfied.

The dielectric function of a sphere in vacuum (or approximately in air) considering only free electrons reads:

$$\varepsilon_{(\omega)} = 1 - \frac{\omega_p^2}{\omega^2 + \iota\gamma\omega} \tag{20}$$

ω_p is the plasma frequency of the material forming the sphere and γ is a damping factor. In analogy with the physical picture of an harmonic oscillators, γ determines the spectral width of the resonance. If γ is small, and assuming $\varepsilon_m \cong 1$, the Frölich condition is met when the incoming electric field shows the frequency $\omega_0 = \frac{\omega_p}{\sqrt{3}}$. ω_p is defined as:

$$\omega_p = \sqrt{\frac{Ne^2}{\varepsilon_0 m^*}} \tag{21}$$

Where *N* is the density per unit of volume of free electrons in the material, *e* is the elementary charge, ε_0 is vacuum dielectric constant and m^* is the effective electrons mass. It can be easily understand how changing the sphere material shifts the plasmonic resonance as a function of free carrier density. Noble metal nanospheres in vacuum/air will typically show localized plasmonic resonances into the visible range of the spectrum, while lower carrier density material such as semiconductors will show plasmonic resonances in the infrared range. This underlines a first important point: plasmonic resonances can indeed be tuned with the choice of the nanosphere and delectric medium chemical composition.

From equations 14 and 15 we can compute the electric field inside and outside the sphere at the localized plasmon resonant frequency:

$$\overrightarrow{E_{in}} = \frac{3\varepsilon_m}{\varepsilon+2\varepsilon_m}\vec{E}_0 \tag{22}$$

$$\overrightarrow{E_{out}} = \vec{E}_0 + \frac{3\hat{n}(\hat{n}\cdot\vec{p})-\vec{p}}{4\pi\varepsilon_0\varepsilon_m}\frac{1}{r^3} \tag{23}$$

Both the sphere internal and external electric fields are amplified under plasmonic resonant conditions. This is one of the most interesting effects associated with localized plasmonic resonances. This near field amplification provides the enhanced light-matter interaction at the basis of several technological applications e.g. light trapping in optoelectronic devices and surface enhanced spectroscopies (PEF, SEIRA, SERS). Electric near field enhancement can be measured directly by a spectroscopic technique known as Scanning Near Field Optical Microscopy (SNOM).

At this point time dependency may be introduced. The time dependent incident electric field is:

$$\vec{E}(\vec{r},t) = \vec{E}_0(\vec{r})e^{\iota\omega t} \tag{24}$$

The spherical particle subject to this electromagnetic plane wave can be treated as an oscillating dipole with $\vec{p}$:

$$\overrightarrow{p} = \varepsilon_0\varepsilon_m\alpha\vec{E}_0e^{\iota\omega t} \tag{25}$$

Where the sphere polarizability $\alpha_{(\omega)}\alpha_{(\omega)}$ is the same function as in the electrostatic scenario. An oscillating dipole emits an electric field, expressed by the second term of Eq. 23. Exploiting the relations describing the field emitted by an oscillating dipole, it's possible to compute the particle absorbance and scattering cross sections, defined as the ratio between the incident and absorbed/scattered power:

$$C_{sct} = \frac{k^4|\alpha|^2}{6\pi} = \frac{8\pi}{3}k^4a^6\left|\frac{\varepsilon-\varepsilon_m}{\varepsilon+2\varepsilon_m}\right|^2 \tag{26}$$

$$C_{abs} = k\,\mathrm{Im}[\alpha] = 4\pi k a^3\,\mathrm{Im}\left[\frac{\varepsilon-\varepsilon_m}{\varepsilon+2\varepsilon_m}\right] \tag{27}$$

Where k is the wavevector of the resonant wavelenght. A peak in both absorbance and scattering cross section manifest when the Frölich condition is met and a localized plasmon is excited. When

the sphere radius *a* is much smaller than λ, absorbance dominates as it depends on a^3. On the other hand, when the particle volume gets bigger scattering becomes dominant, as it depends on a^6. Moreover, because of this a^6 dependency, a few large particles are sufficient for scattering to be prevalent in multi-particle systems. It has to be underlined that Eq. 26 and 27 are perfectly valid also for dielectric particles. It is very important to note that both the absorbance and scattering cross sections of resonant plasmonic nanoparticles are considerably greater than their geometrical one. Plasmonic nanoparticles can thus act as energy absorbers/concentrators and optical antennas, crucial features in a plethora of already mentioned optical and photonic applications.

Ellipsoidal particles– tuning of the localized plasmonic resonance with shape and size

Let's consider now an ellipsoidal particle with semi-axis $a_1 \leq a_2 \leq a_3$, described by the equation $\frac{x^2}{a_1} + \frac{x^2}{a_2} + \frac{x^2}{a_3} = 1$. Three different values are now found for the particle polarizability (i=1,2,3):

$$\alpha_i = 4\pi a_1 a_2 a_3 \frac{\varepsilon_{(\omega)} - \varepsilon_m}{3\varepsilon_m + 3L_i(\varepsilon_{(\omega)} - \varepsilon_m)} \tag{28}$$

L_i is a geometrical factor defined as:

$$L_i = \frac{a_1 a_2 a_3}{2} \int_0^\infty \frac{dq}{(a_i^2 + q) f(q)} \tag{29}$$

Where $f(q) = \sqrt{(q + a_1^2)(q + a_2^2)(q + a_3^2)}$. These geometrical factors satisfy the condition $\sum L_i = 1$. It worth to note that for the case of a sphere where $a_1 = a_2 = a_3$, then $L_1 = L_2 = L_3 = \frac{1}{3}$, giving back eq. 2.4; that is, an isotropic polarizability and a single localized plasmon resonant frequency. An important class of ellipsoid are prolate spheroids, which show two equal minor axes and a major axis ($b = c\,; a > c$). In this case the particle polarizability will show two distinct maxima for two different frequencies of the incident field and, consequently, two different localized plasmon resonances: a "short" axis mode and a "long" axis mode, which will be excited by the component of the incident electric field oscillating along their respective directions [25]. Fixing a prolate spherical nanoparticle volume and modulating their shape as a function of their aspect ratio (defined as shorter axis c divided by major axis a), show how the two different plasmonic frequencies shift compared to the nanosphere case (Fig. 8).

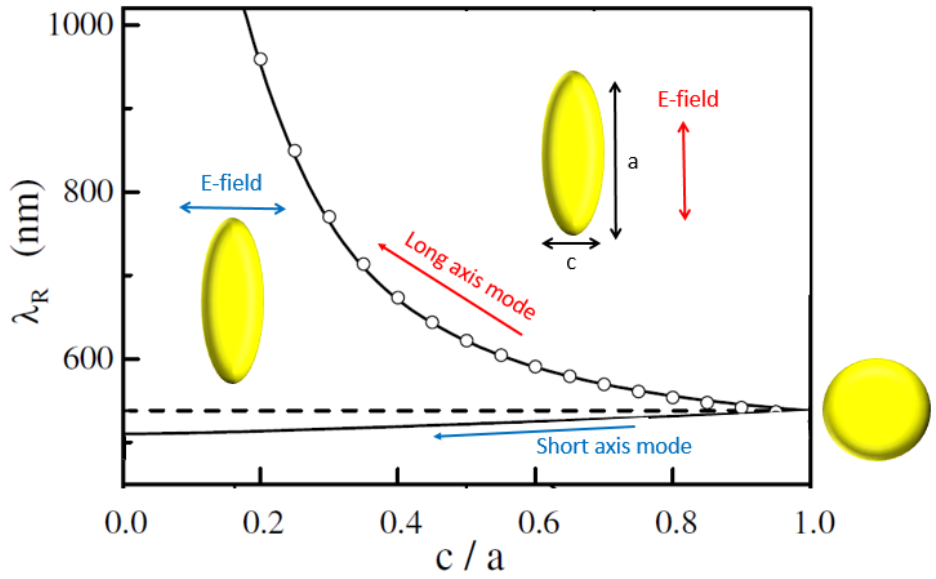

Figure 8 – "Short axis" and "long axis" mode plasmonic resonant wavelentgh for a prolate spheroid as function of its aspect ratio.

The long axis mode red-shifts remarkably to lower frequencies compared to the nanosphere case by decreasing its aspect ratio. The short axis mode blue-shifts to higher frequencies instead, with a much lesser efficiency.

All this to evidence a very general crucial point. The LSPR of a nanoparticle can be spectrally tuned by engineering its shape, as well as its chemical composition. Moreover, the plasmonic response of a nanoparticle can show a strong anisotropic behavior. These are all fundamentals points for every technological application of plasmonics, largely investigated in this thesis work.

Relaxation of the quasi-static approximation for large nanoparticles – Mie theory

The quasi-static approximation model well predicts experimental data only for significatively subwavelength nanoparticles. When structures start to have one of their characteristic size exceeding about 100 nm, the agreement is progressively lost, due to so-called retardation effects caused by the dephasing of the incident electric field over the nanoparticle volume. To take this effects into account a more complete electromagnetic description of the problem has to be considered, provided by Gustav Mie theory for a spherical particle, which expands the electric field inside and outside the particles into series of multipolar optical modes [23]. The dipolar mode is the first term in a power series expansion of the scattering and absorbance coefficients computed

in the context of the theory. The particle polarizability approximated to the first order in this multipolar approach reads [24]:

$$\alpha_V = \frac{1-\frac{1}{10}(\varepsilon-\varepsilon_m)x^2+O(x^4)}{(\frac{\varepsilon_m)}{3\,(\varepsilon-\varepsilon_m)}-\frac{1}{30}(\varepsilon+10\varepsilon_m)x^2-i\frac{4\pi^2{\varepsilon_m}^{3/2}V}{3\lambda_0^3}+O(x^4)} \quad (30)$$

The parameter $x = \frac{\pi a}{\lambda_0}$ correlates the particle radius to the incident electric field wavelength in vacuum, and ultimately quantifies retardation effects (for $x << 1$, Eq. 30 reduces to the dipolar quasi-static nanosphere polarizability of Eq. 17). Thus for a Drude metal nanosphere the LSPR red-shift by increasing the particle volume. Moreover, increasing the volume also spectrally broadens and weakens the plasmonic resonance because of the imaginary term in the denominator of Eq. 30, which is linearly proportional to the particle volume and quantifies the damping due to electron-phonon elastic scattering. These retardation effects can be exploited to engineer noble metal nanostructures showing a LSPR into the infrared range as the experimental work presented in chapter 2 of this thesis will demonstrate.

1.3.2 Surface plasmons polaritons

Surface plasmons polaritons are electromagnetic modes propagating at the interface between a conductive and an insulating material. They are confined at the interface, decaying evanescently away from it. Their propagating nature makes them interesting for waveguiding applications, which are in general not enabled by localized plasmons [24,26]. SPP can be excited by photons, thus confining their energy in subwavelength volumes at the interface. This however can't be done by direct illumination as for localized surface plasmons. In this chapter first we will compute the Surface Plasmon Polaritons dispersion relation using relations directly derived by Maxwell equations. We will then consider how SPP can be experimentally coupled to an external electromagnetic wave. Lasty we will make some consideration about the spatial profile and features of these propagating modes.

Surface plasmons polariton excitation and main features

The simplest geometry which can sustain the excitation of a propagating Surface Plasmon Polariton (SPP) consists in a flat interface between a semi-infinite metal and dielectric half-space

(Fig. 9). The metal half space is characterized by a complex, isotropic and frequency dependent dielectric function $\varepsilon_{1(\omega)}$. The non-absorbing dielectric half space is characterized by a positive, real, isotropic dielectric constant $\varepsilon_2 > 0$.

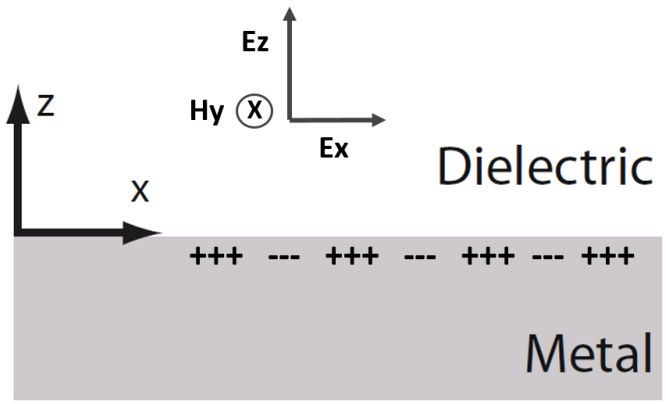

Figure 9 – Sketch of the SPP equations coordinates system, field components and charge distribution.

We search for wave solutions confined at the metal/dielectric interface propagating along the *X* direction (Fig. 9). The SPP must show an evanescent field decay away from the surface in both half-spaces. We consider TM polarized wave solutions. In a wave of this kind the magnetic field is perpericular the the plane of incidence, defined by the SPP propagation direction and the normal to the surface. For TE waves, where the electric field vector is perpendicular to the plane of incidence, it's been demonstrated that no appropriate solution exists; SPP are indeed exclusively TM waves [24,26]. Directly following from Maxwell equations, solutions of this form are found for the electric field vectors E and for the magnetic field vector H, for z>0 (dielectric half-space):

$$H_y(z) = A_2 e^{i\beta x} e^{-k_2 z} \tag{31}$$

$$E_x(z) = iA_2 \frac{1}{\omega\varepsilon_0\varepsilon_2} k_2 e^{i\beta x} e^{-k_2 z} \tag{32}$$

$$E_z(z) = -A_1 \frac{\beta}{\omega\varepsilon_0\varepsilon_2} e^{i\beta x} e^{-k_2 z} \tag{33}$$

And for z<0 (metal half space) we get:

$$H_y(z) = A_1 e^{i\beta x} e^{k_2 z} \tag{34}$$

$$E_x(z) = -iA_1 \frac{1}{\omega\varepsilon_0\varepsilon_1} k_1 e^{i\beta x} e^{k_1 z} \tag{35}$$

$$E_z(z) = -A_1 \frac{\beta}{\omega\varepsilon_0\varepsilon_1} e^{i\beta x} e^{k_1 z} \tag{36}$$

Where k_i $(i = 1,2) \equiv k_{i,z}$ is the wavevector along the z direction inside the two half-spaces (1=metal, 2=dielectric), ε_o is the dielectric constant of vacuum, $\beta = k_x$ for readabiliy is the SPP wavevector along the x direction, and A_1 and A_2 are the two wave amplitude coefficients inside the two media. The wavevector z component reciprocal value $1/|k_{z,i}|\,\hat{z}$ quantifies the evanescent field decay length orthogonal to the surface, in the two half-spaces, and thus the wave interface confinement. Continuity at the interface of H_y, $\varepsilon_1 E_z$ and $\varepsilon_2 E_z$ imposes that $A_1 = A_2$, and:

$$\frac{k_2}{k_1} = -\frac{\varepsilon_2}{\varepsilon_1} \tag{37}$$

Exploiting a condition imposed by Maxwell equations on H_y, it can be demonstrated that:

$$k_1^2 = \beta^2 - k_0^2\varepsilon_1 \tag{38}$$

$$k_2^2 = \beta^2 - k_0^2\varepsilon_2 \tag{39}$$

By combining these equations with and Eq. 37 we find:

$$\beta = \frac{\omega}{c}\sqrt{\frac{\varepsilon_1\varepsilon_2}{\varepsilon_1+\varepsilon_2}} = k_x = k_{SPP} \tag{40}$$

This is dispersion relation of the SPP, correlating it's frequency to it's wavevector k_{SPP}. In Figure 10, the SPP dispersion relation for a undamped metal/dielectric interface is shown along with the dispersion of a photon travelling parallel to the interface inside the dielectric half space:

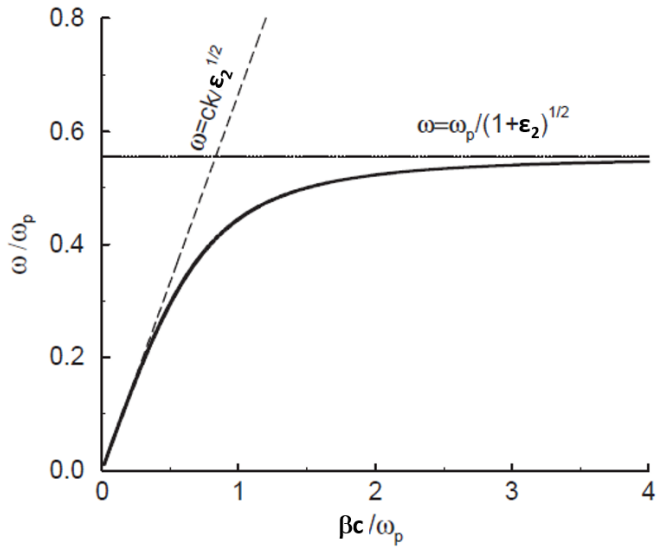

Figure 10 – Dispersion relation of the SPP (solid line) and light line of a photon travelling into the dielectric medium parallel to the dielectric/metal interface (dashed line).

For $k_x \rightarrow \infty$ the SPP dispersion approaches the characteristic frequency $\omega_{spp} = \frac{\omega_p}{\sqrt{1+\varepsilon_2}}$ while the group velocity $v_g \rightarrow 0$, and thus the mode becomes of an electrostatic nature. It is worth to note how the wavelength of an SPP can be smaller than an equal energy photon's wavelenght, enabling subwavelentgh confinement, a key property of SPPs for photonic circuits miniaturization. For small k_x instead the SPP dispersion lies close to light line of the photon travelling parallel to the interface into the dielectric medium, but they never cross. This means that a photon must acquire an additional momentum to excite an SPP. This can be done in the so called Otto and Kretschmann configurations, sketched in Fig. 11a and 11b respectively.

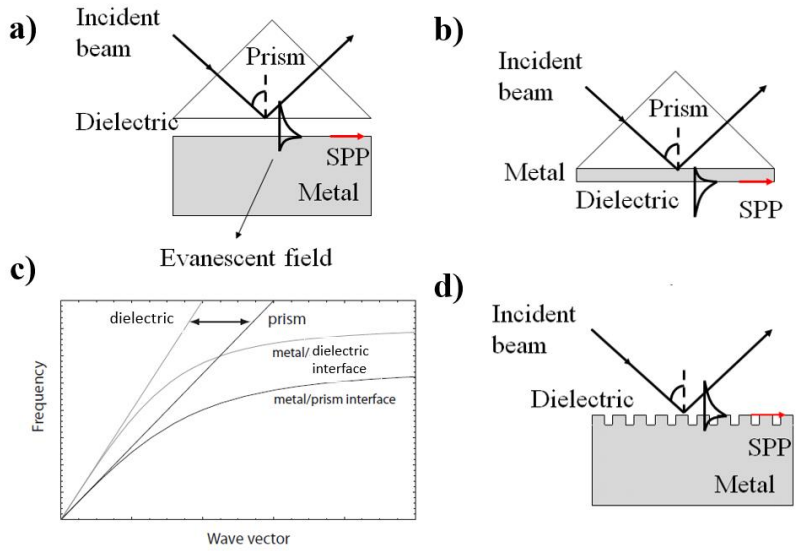

Figure 11- a,b) Sketches of Otto and Kretschmann configurations, respectively. c) Light travelling parallel to the interface into the prism can couple evanescently at the metal/dielectric interface in both Otto and Kretschmann case. d) Photon-SPP coupling through momentum exchange with a diffraction grating at the metal/dielectric interface.

Light is shined through a prism separated from a metal surface by a thin gap of dielectric (Otto) or through a prism with a thin metal film directly grown on it's surface (Kretschmann). Light is shined at such an angle to produce total internal reflection inside the prism. In both configurations, the evanescent field of the photon internally reflected parallel to the prism surface can evanescently couple to an SPP at the dielectric/metal inteface where the two dispersion relations cross, as shown is Fig. 11c. Coupling condition depends on the refractive index of the prism, which determines the light line, and on the dispersion curve of the SPP, determined by the dielectric functions of the metal and dielectric gap or environment. Another way to couple photons to SPPs is to consider a diffraction grating at the metal/dielectric interface (Fig. 11d), which transers a momentum to the incoming photons equal to:

$$k_G = \pm n\frac{2\pi}{a} \tag{41}$$

Where n is an integer number and *a* is the periodicity of the grating. The photon dispersion curve as a function of k_x is thus rigidly translated of an amount $\pm k_G$ following the relation:

$$k_{x-photon} = |k_{photon}| \sin\theta \pm n\frac{2\pi}{a} \quad (42)$$

Where $\sin\theta$ in the photon incident angle with respect to the surface normal. If $k_{x-photon} = k_{SPP}$, and the photon's energy matches the SPP's, a surface plasmon polariton is exctied along the metal/dielectric interface. This phonomena is particoularly relevant to this thesis and will be more deeply argumented in chapter 6.

Taking into account the imaginary part of the metal complex dielectric function it is possible to computer the SPP propagation length intensity L:

$$L = \frac{1}{2\mathrm{Im}[\beta]} \quad (43)$$

For relatively undamped metals with complex dielectric function $\varepsilon_{1(\omega)} = \varepsilon_{1(\omega)}' + \varepsilon_{1(\omega)}''$ with $|\varepsilon_{1(\omega)}''| << < |\varepsilon_{1(\omega)}'|$:

$$\mathrm{Im}[\boldsymbol{\beta}] = \frac{\omega}{c}\sqrt{\frac{\varepsilon_{1(\omega)}'\varepsilon_2}{\varepsilon_{1(\omega)}'+\varepsilon_2}}\,\frac{\varepsilon_{1(\omega)}''\varepsilon_2}{2\varepsilon_{1(\omega)}'(\varepsilon_{1(\omega)}'+\varepsilon_2)} \quad (44)$$

L is typically between 10 and 100 μm, depending on the materials involved. It is worth to comment further on the SPP field confinement $z=1/|k_{z,i}|$ (i=1 metal side, i=2 dielectric side) where $|k_{z,i}|$ is:

$$k_{z.i} = \sqrt{\boldsymbol{\beta}^2 - (\frac{\omega}{c})\varepsilon_i} \quad (45)$$

As the SPP frequency rises the field confinement, and thus the field enhancement and energy localization, improves while the propagation length decreases due to increased damping. For example, at an air silver/interface, for SPP wavelenght λ = 450 nm, $L \approx 16$ μm and $z \approx 180$ nm into the dielectric. At $\lambda \approx 1.5$ μm instead, $L \approx 1080$ μm and $z \approx 2.6$ μm. This trade-off between field confinement and loss is typical of plasmonics. In general it's possible to note that field confinement below the diffraction limit of half the photon wavelength in the dielectric can be achieved close to ω_{spp}. Furthermore we can lastly comment that the field confinement is asymmetric in the metal and dielectric half spaces. Indeed in the metal the SPP field typically decays completely over distances on the order of 20 nm in the visible/IR range, while on the dielectric side in can extend

to hundreds of nm, as we saw for the air/Ag case. This means that most of the incoming field energy will be confined on the metal side of the propagating SPP.

REFERENCES

(1) Genzer, J.; Groenewold, J. Soft Matter with Hard Skin: From Skin Wrinkles to Templating and Material Characterization. *Soft Matter* **2006**, *2* (4), 310. https://doi.org/10.1039/b516741h.

(2) Khang, D.-Y.; Rogers, J. A.; Lee, H. H. Mechanical Buckling: Mechanics, Metrology, and Stretchable Electronics. *Advanced Functional Materials* **2009**, *19* (10), 1526–1536. https://doi.org/10.1002/adfm.200801065.

(3) Landau, L. D.; Lifšic, E. M.; Landau, L. D. *Theory of Elasticity*, 3. engl. ed., rev.enlarged, reprint.; Course of theoretical physics; Elsevier: Amsterdam, 2008.

(4) Song, J.; Jiang, H.; Liu, Z. J.; Khang, D. Y.; Huang, Y.; Rogers, J. A.; Lu, C.; Koh, C. G. Buckling of a Stiff Thin Film on a Compliant Substrate in Large Deformation. *International Journal of Solids and Structures* **2008**, *45* (10), 3107–3121. https://doi.org/10.1016/j.ijsolstr.2008.01.023.

(5) Park, H.-G.; Jeong, H.-C.; Jung, Y. H.; Seo, D.-S. Control of the Wrinkle Structure on Surface-Reformed Poly(Dimethylsiloxane) via Ion-Beam Bombardment. *Scientific Reports* **2015**, *5* (1). https://doi.org/10.1038/srep12356.

(6) Nania, M.; Matar, O. K.; Cabral, J. T. Frontal Vitrification of PDMS Using Air Plasma and Consequences for Surface Wrinkling. *Soft Matter* **2015**, *11* (15), 3067–3075. https://doi.org/10.1039/C4SM02840F.

(7) Owen, M. J.; Smith, P. J. Plasma Treatment of Polydimethylsiloxane. *Journal of Adhesion Science and Technology* **1994**, *8* (10), 1063–1075. https://doi.org/10.1163/156856194X00942.

(8) Kim, P.; Hu, Y.; Alvarenga, J.; Kolle, M.; Suo, Z.; Aizenberg, J. Rational Design of Mechano-Responsive Optical Materials by Fine Tuning the Evolution of Strain-Dependent Wrinkling Patterns. *Advanced Optical Materials* **2013**, *1* (5), 381–388. https://doi.org/10.1002/adom.201300034.

(9) Barelli, M.; Repetto, D.; de Mongeot, F. B. Infrared Plasmonics via Self-Organized Anisotropic Wrinkling of Au/PDMS Nanoarrays. *ACS Applied Polymer Materials* **2019**, *1* (6), 1334–1340. https://doi.org/10.1021/acsapm.9b00138.

(10) Navez, M.; Sella, C.; Chaperot, D. Etude de l'attaque Du Verre Par Bombardement Ionique. *C. R. Acad. Sci. Paris* **1962**, *254*, 240-248.

(11) Valbusa, U.; Boragno, C.; Mongeot, F. B. de. Nanostructuring Surfaces by Ion Sputtering. *Journal of Physics: Condensed Matter* **2002**, *14* (35), 8153–8175. https://doi.org/10.1088/0953-8984/14/35/301.

(12) Chan, W. L.; Chason, E. Making Waves: Kinetic Processes Controlling Surface Evolution during Low Energy Ion Sputtering. *Journal of Applied Physics* **2007**, *101* (12), 121301. https://doi.org/10.1063/1.2749198.

(13) Bradley, R. M.; Harper, J. M. E. Theory of Ripple Topography Induced by Ion Bombardment. *Journal of Vacuum Science & Technology A: Vacuum, Surfaces, and Films* **1988**, *6* (4), 2390–2395. https://doi.org/10.1116/1.575561.

(14) Giordano, M. C.; de Mongeot, F. B. Anisotropic Nanoscale Wrinkling in Solid-State Substrates. *Advanced Materials* **2018**, *30* (30), 1801840. https://doi.org/10.1002/adma.201801840.

(15) Toma, A.; Buatier de Mongeot, F.; Buzio, R.; Firpo, G.; Bhattacharyya, S. R.; Boragno, C.; Valbusa, U. Ion Beam Erosion of Amorphous Materials: Evolution of Surface Morphology. *Nuclear Instruments and Methods in Physics Research Section B: Beam Interactions with Materials and Atoms* **2005**, *230* (1–4), 551–554. https://doi.org/10.1016/j.nimb.2004.12.099.

(16) Cuerno, R.; Barabási, A.-L. Dynamic Scaling of Ion-Sputtered Surfaces. *Physical Review Letters* **1995**, *74* (23), 4746–4749. https://doi.org/10.1103/PhysRevLett.74.4746.

(17) Chan, W.-L.; Zhao, K.; Vo, N.; Ashkenazy, Y.; Cahill, D. G.; Averback, R. S. Stress Evolution in Platinum Thin Films during Low-Energy Ion Irradiation. *Physical Review B* **2008**, *77* (20). https://doi.org/10.1103/PhysRevB.77.205405.

(18) Medhekar, N. V.; Chan, W. L.; Shenoy, V. B.; Chason, E. Stress-Enhanced Pattern

Formation on Surfaces during Low Energy Ion Bombardment. *Journal of Physics: Condensed Matter* **2009**, *21* (22), 224021. https://doi.org/10.1088/0953-8984/21/22/224021.

(19) Arnold, G. W. Ion-Implantation-Induced Stress in Glasses: Variation of Damage Mode Efficiency with Changes in Glass Structure. *Nuclear Instruments and Methods in Physics Research Section B: Beam Interactions with Materials and Atoms* **1988**, *32* (1–4), 504–507. https://doi.org/10.1016/0168-583X(88)90261-3.

(20) Miotello, A.; Mazzoldi, P. Sputtering Process during Ion Implantation in Glasses: Mathematical and Physical Analysis. *Journal of Physics C: Solid State Physics* **1983**, *16* (1), 221–228. https://doi.org/10.1088/0022-3719/16/1/024.

(21) Johnston, I. D.; McCluskey, D. K.; Tan, C. K. L.; Tracey, M. C. Mechanical Characterization of Bulk Sylgard 184 for Microfluidics and Microengineering. *Journal of Micromechanics and Microengineering* **2014**, *24* (3), 035017. https://doi.org/10.1088/0960-1317/24/3/035017.

(22) Pearson, D. A.; Bradley, R. M. Theory of Terraced Topographies Produced by Oblique-Incidence Ion Bombardment of Solid Surfaces. *Journal of Physics: Condensed Matter* **2015**, *27* (1), 015010. https://doi.org/10.1088/0953-8984/27/1/015010.

(23) Mie, G. Beiträge zur Optik trüber Medien, speziell kolloidaler Metallösungen. *Annalen der Physik* **1908**, *330* (3), 377–445. https://doi.org/10.1002/andp.19083300302.

(24) Maier, S. A. *Plasmonics: Fundamentals and Applications*; Springer: New York, 2007.

(25) Muskens, O.; Christofilos, D.; Fatti, N. D.; Vallée, F. Optical Response of a Single Noble Metal Nanoparticle. *Journal of Optics A: Pure and Applied Optics* **2006**, *8* (4), S264–S272. https://doi.org/10.1088/1464-4258/8/4/S28.

(26) Zayats, A. V.; Smolyaninov, I. I.; Maradudin, A. A. Nano-Optics of Surface Plasmon Polaritons. *Physics Reports* **2005**, *408* (3–4), 131–314. https://doi.org/10.1016/j.physrep.2004.11.001.

CHAPTER 2

Large area infrared plasmonics via anisotropic wrinkling of flexible Au/PDMS nanoarrays

Introduction

Recently a strong interest rose towards the integration of plasmonic devices onto flexible polymeric surfaces [1,2] having in mind a huge amount of applications like e.g. stretchable electronics [5], tunable optofluidic devices [6], microfluidic devices for biology, pharmacy and tissue engineering [7–11], membranes for organic solvent nanofiltration [12], analytical chemistry [13], protective marble coatings [14], strain gauges and pressure sensors [15]. Thus, if flexibility represents a key property, elastomers like polydimethylsiloxane (PDMS) are particularly convenient due to their relatively low modulus (~1.6 MPa) [3], near incompressibility (the Poisson ratio reads ~0.5) [3], and large fracture strain (~160%) [4]. Additionally, PDMS shows several other desirable properties such as biocompatibility, hydrophobicity, high oxygen permeability, transparency, non-toxicity and low-cost.

Several fabrication approaches, both top-down and bottom-up, have been explored to modify and engineer the PDMS surface for device fabrication [16]. The production of rough surfaces containing micro-, and nano-composite features is made possible by one-step laser etching. The structured surface shows super-hydrophobic properties and could be used for lossless liquid transport and microfluidic devices fabrication [17]. However, in these examples the pattern is isotropic and the modified PDMS surface is not suitable to be used as a template for the confined growth of well-defined metal structures. The experiments described in section 1.2.3 of this thesis have demonstrated that solid state, inorganic soda lime glasses exposed to irradiation with noble gas ions at non-normal incidence angles undergo a uniaxial wrinkling instability, when kept at a temperature close to their glass transition threshold. The formation of large area, self-organized anisotropic periodic channels on the surface is much more suited to the controlled confinement of metal structures when compared to isotropic patterns [18]. The same grazing ion incidence protocol, if applied to PDMS substrates, does instead lead to the formation of an isotropic meandering

pattern analogous to the results of Park et al. [19]. This is because the ion range in the material (few nm) is much smaller than the typical scale of the wrinkles (fractions of micrometer).

In a previous work, the laboratory which hosted me obtained uniaxial modulations on PDMS by a replica molding process using the low cost IBS soda-lime glass as "masters" [20]. This soft lithographic fabrication method enabled large area production of nanostructured hydrophobic PDMS surfaces ideal for the growth of high density, pillar-like Au clusters, well suited for applications such as Surface Enhanced Raman Spectroscopy (SERS). The resulting PDMS anisotropic templates however showed poor degree of order, low height/width aspect ratios and limited morphological tunability, with wavelength periodicity in the range of 200 nm. Given the glancing angle deposition conditions employed, the Au cluster widths are limited well below 100 nm range where the quasistatic approximation still holds and depolarization effects produced on big particles, described in section 1.3 of the thesis, cannot be exploited for redshifting the LSP resonance deep into the NIR range. For this reason, the resonant wavelength of the LSP dipolar excitation could be tailored in a limited range around 600-700 nm and no multipolar plasmon resonances could be excited. Similar conclusions were reached when Au evaporation was directly performed on the rippled glass templates produced by self-organized ion beam sputtering (see e.g. [21] and references therein cited) since the periodicity of the template is limited in the range below 200 nm. Alternatively, highly ordered anisotropic PDMS patterns have been prepared by replica molding recurring to top-down approaches based on Electron Beam Lithography (EBL) for the fabrication of the master [22]. However, the high costs and limited working area of EBL represent a drawback for device fabrication at the industrial level.

In my PhD work I exploited PDMS templates with a uniaxial wrinkle pattern obtained by air plasma irradiation of a pre-stretched substrate, following an approach similar to Kim et al [23]. The rippled PDMS substrates are endowed with remarkably long range order, high aspect ratios, and tunable morphology. The wrinkled PDMS thus constitutes an ideal template for the confinement of uniaxially ordered and finely tailored arrays of noble metal (Au) nanowires by grazing angle thermal deposition over cm^2 areas. The shape, size and orientation of the Au nanostructures are tailored by controlling the periodicity of the rippled PDMS template from about 300 nm to 1 um, the height of the ripples from 50 nm to 350 nm, and the metal deposition parameters. In this way, we are able to increase the width of Au NWs up to 285 nm, substantially above the quasistatic

limit, where strong depolarization effects come into play and multipolar plasmon excitation becomes observable. For light polarized orthogonal to the NW axis, the LSP resonant wavelength can be tuned over a remarkably large spectral range which spans from about 600 nm to 1200 nm. For light polarized in the longitudinal direction the optical response is equivalent to a continuous film since the NW have lengths in the 10 μm range and form a percolated network. Finally, we show that is possible to conjugate on the same flexible PDMS sample remarkable electrical transport properties with low sheet resistance in the 15 Ohm/sq range, semi-transparency and plasmonic properties thus making them suitable for a broad range of optoelectronic, energy harvesting, and sensing applications.

2.1 – Results and discussion

Wrinkling of air plasma treated pre-stretched PDMS surfaces

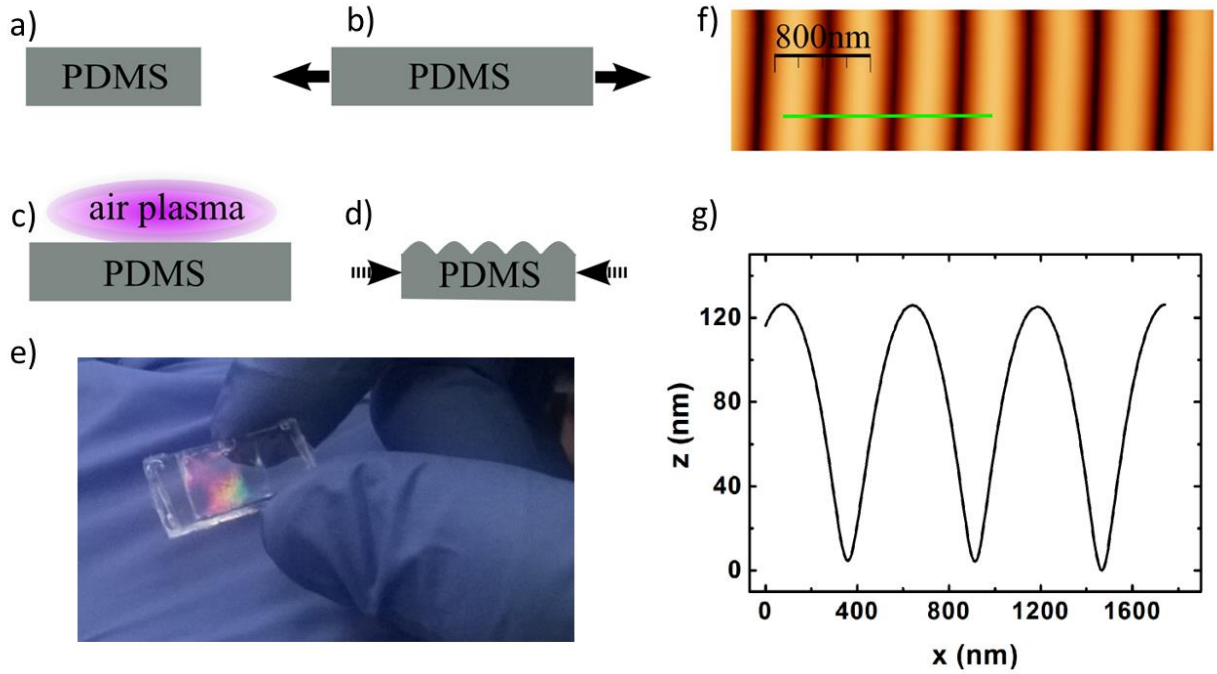

Figure 1: *a)-d) Sketch of the fabrication process of nanostructured PDMS substrates. e) Periodic corrugations on the PDMS surface give rise to grating diffraction effects over macroscopic areas. f) AFM image of a rippled PDMS substrate. g) Line profile along the AFM image shown in f).*

The formation of PDMS templates with uniaxial periodic modulations is achieved by exposing a

pre-stretched sample to an air plasma as outlined in the sketches of Fig. 1a-1d: a PDMS sample (see the Experimental section for details) is stretched in a controllable way (Fig. 1b) and then placed in a vacuum chamber for the plasma treatment (Fig. 1c). Exposure of the polymer surface to the air plasma leads to the formation of a compressively stressed skin layer with increased bulk elastic modulus due to the cleavage of $Si–CH_3$ groups and the formation of a denser, SiO_X-rich glass-like surface layer [23,24]. After removing the sample from the chamber, and once the stretching is released, an undulated pattern appears on the surface (Fig. 1d). The formation of a periodic pattern can be understood in the context of continuum elastic models which describe wrinkling of elastic films bound by a compressively stressed hard skin as described in section 1.1 of the thesis [25,26]. It is worth to note that no substantial differences in the surface morphology have been observed in our experiments by using an oxygen plasma instead of an air plasma (this allows of course a further decrease of the fabrication costs).

Morphological characterization and Au nanowires confinement

Atomic Force Microscopy (AFM) measurements (Fig. 1f) demonstrate that a regular periodic nanoripple pattern is formed on the polymer surface exposed to the plasma, while the grating light scattering effects evident in the photograph of Fig. 1e reveals that the motif extends over large cm^2 areas. The periodicity (λ) and height (A) of the ripples (respectively 550 nm and 120 nm) highlighted in the AFM line profile of Fig. 1g, are derived from a statistical analysis of the AFM images by means of WSxM software [27]. The ripple morphology of Fig. 1f-g is determined by the main experimental parameters: applied pre-stretching (S=40%), RF plasma power (P=50 W) and time (t=60 s) of the plasma process [28] as discussed further ahead. The extremely high degree of order of the rippled PDMS template is quantitatively demonstrated by the self-correlation of AFM images (Fig. 8 in Experimental section) which show higher order oscillations exceeding the 10^{th} harmonic. The PDMS samples endowed with such steep periodic grooves can be considered as ideal templates for the confinement of metallic nanowires (NW), when Au deposition takes place at grazing angles with respect to the surface normal.

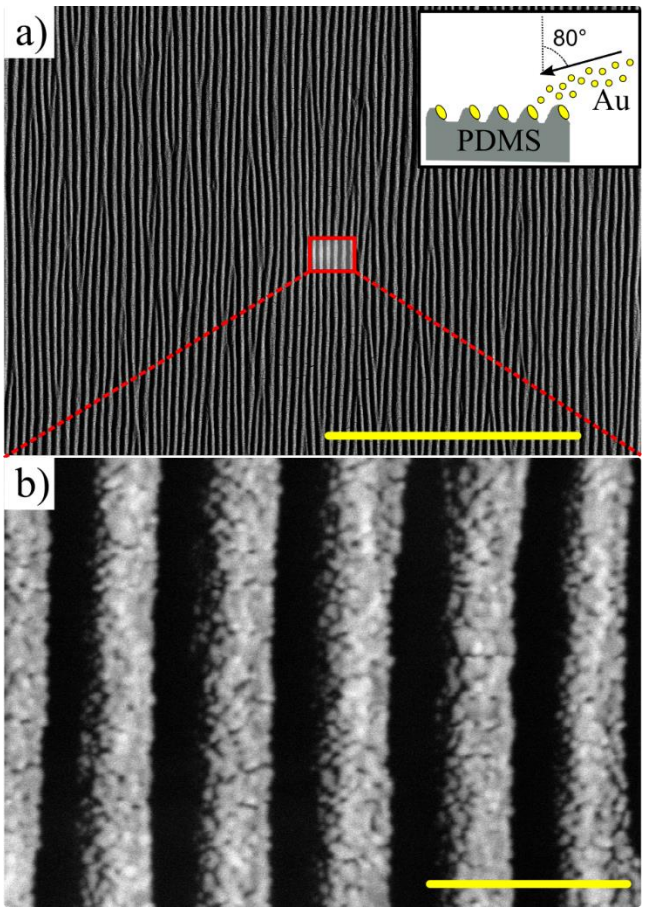

Figure 2: *a) SEM image of 10 nm Au deposited at grazing incidence on rippled PDMS substrate. Deposition geometry is sketched in the inset: the Au flux direction is perpendicular to the ripple long axis and forms an 80° angle with the substrate normal. SEM image acquired in the backscattered channel with a primary beam energy of 15kV and a magnification of 5k; the yellow scale bar corresponds to 10 µm. b) Zoom-in of the image shown in a) in which the polycrystalline structure of the Au wires is well visible. SEM image acquired in the backscattered channel with a primary beam energy of 15kV and a magnification of 80k; the yellow scale bar corresponds to 500 nm.*

Fig. 2 shows an array of NW obtained by the physical vapour deposition of 10 nm of Au on rippled PDMS at a grazing angle of 80° as highlighted in the inset of Fig. 2a. Simple geometrical arguments, derived from the AFM line profile of the sinusoidal template, allow to derive the height h of the tilted NW given the Au thickness (h_0) evaporated on a flat substrate facing the source at normal incidence and the average slope of the illuminated facet θ as $h=h_0\times\cos(80°-\theta)=10.6$ nm.

The PDMS template in this case was obtained by air plasma treatment with pre-stretching S=30%, P = 20 W, t = 15 s and the resulting periodicity and amplitude read respectively λ=310 nm and A=50 nm.

Due to the glancing evaporation conditions here adopted, the gold nanostripes decorate only the "illuminated" ripple facets, separated by alternating gaps in the shadowed regions. Scanning Electron Microscope (SEM) images (Fig. 2a) were statistically analysed by means of ImageJ software suite in order to determine the average NW transversal width $w_{//}$ projected on the horizontal plane (Fig. 9 in the experimental section). The width w of the tilted NWs is in turn found by taking into account the average slope θ of the Au covered PDMS ripples with respect to the horizontal plane, derived from the AFM profile, as $w=w_{//} / \cos(\theta)$. For the sample of Fig. 2, w=145 nm (see Table 1). SEM images also show that NW length can extend up to several tens of micrometers. A look at higher magnification evidences the polycrystalline structure of the Au wires, with grain sizes in the range of 30 nm (Fig. 2b).

Excitation of tunable dipolar and multipolar LSP modes in the Vis and NIR spectral range

The optical properties of the NW have been investigated by transmission (extinction) measurements at normal incidence. With light polarized parallel to the NW long axis, the electrons are free to oscillate unconstrained along the connected metallic nanostructures and the optical spectrum is similar to that of a continuous film (TE signal, black line in Fig. 3). When light is polarized along the NW short axis, electron confinement effects become relevant, and a Localized Surface Plasmon Resonance (LSPR) at 620 nm becomes clearly visible in the spectrum (TM signal, red line in Fig. 3).

The strongly dichroic optical response confers to the NW array the performance of a wire grid polarizer in the IR spectral region while in the visible spectral range the response is dominated by the LSP resonance in TM polarization.

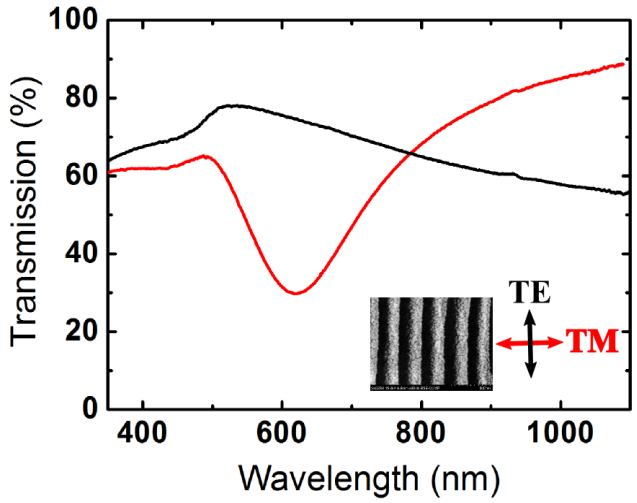

Figure 3: *Optical extinction spectra with polarized light in TE (black line) and TM (red line) directions, measured on the Au nanowires of Fig. 2. The measurements are normalized to the ones made on a bare and flat PDMS sample.*

Different PDMS templates with tailored ripple morphology have been fabricated by varying the parameters of the air plasma treatment. A summary of the experiments is reported in Table 1 where the air plasma induced nanostructures (samples A, C, D) are compared with those obtained by irradiation with a defocused Ar+ Ion Beam (sample B). In the latter case, the polymer sample was pre-stretched at S=30% before being introduced in a vacuum chamber and then irradiated for 15 seconds with Argon ions at an energy of 80 eV and 4.0×10^{-4} mbar of pressure (gas purity N5.0). The base pressure in the vacuum chamber in the order of 10^{-7}mbar. As a general rule, by increasing the energy deposited in the air plasma treatment (the product between P and t) a thicker modified surface layer is formed, endowed with a higher Young modulus (in the range of 1.5 GPa) compared to the untreated bulk material (1.5 MPa), and correspondingly both the height and the wavelength of the ripples increase. On the other hand, by increasing the amount of sample pre-stretching, higher ripples of shorter wavelength can be formed on the surface [23].

Sample	S(%)	P(W)	t(s)	λ(nm)	A(nm)	θ(°)	h (nm)	w (nm)	h/w	LSPR(nm)
A	30	20	15	310	50	20	10.6	145	0.073	620
B	30	80 V(*)	15	450	80	21	10.7	170	0.063	725
C	40	50	60	550	120	25	11.0	190	0.058	800
D	50	100	60	900	340	34	12.0	285	0.042	1150

Table 1: *Localized Surface Plasmon Resonance (LSPR), Au nanowire width (w) and height (h) as a function of the morphological features of the PDMS template, ripple period (λ), height (A), local slope (θ) and of the NW aspect ratio (h/w). Also shown are the parameters employed for the plasma treatment of the PDMS template, pre-stretching (S), power (P) and time (t).*

Simple geometrical arguments, assuming a sinusoidal template profile, suggest that the width of the NW supported on the facets illuminated by the Au beam is directly proportional to the period of the PDMS ripple (column "w" vs column "λ" in Table 1). By increasing the NW width (w) one can monotonically decrease the NW height/width aspect ratio (defined as h/w) since the NW height has been kept almost fixed in these experiments.

In Figure 4 we show the optical spectra (TM polarization) for the NW samples grown on the PDMS templates prepared under different plasma conditions. The NW width increase monotonically from 145 nm (black curve, sample A) up to 285 nm (green curve, sample D). Since in these experiments the NW thickness h is kept nearly constant, we can easily tune their aspect ratio h/w which decreases from 0.073 down to 0.042. The dipolar LSP resonance (marked by a circle) is systematically redshifted from 620 nm up to the maximum measured value of 1150 nm for the broadest NW sample.

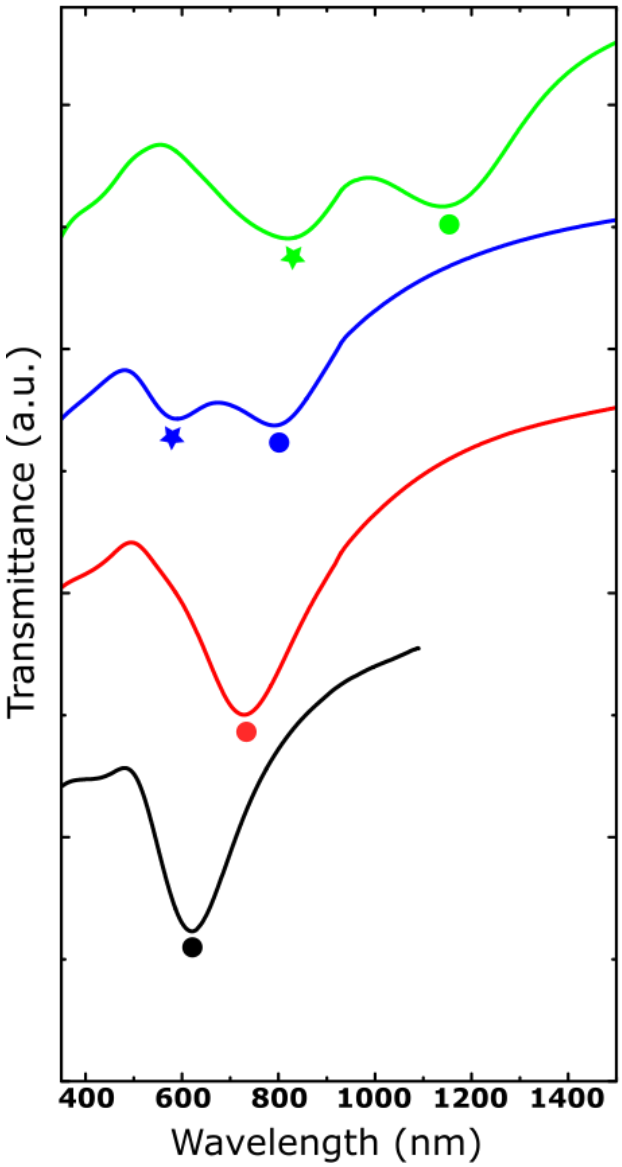

Figure 4: *Optical extinction spectra of TM polarized light for samples A (black curve), B (red curve), C (blue curve) and D (green curve). The circles identify the position of the dipolar LSPR resonance (n=1) while the stars identify the multipolar resonance (n=3).*

For the NW samples whose widths w exceeds 170 nm (sample C and D) it is also relevant the presence of an additional extinction peak marked by a star, respectively centred around 600 nm and 820 nm, which is blueshifted with respect to the dipolar excitation. These peaks are assigned to the excitation of multipolar plasmon modes of odd order (n=3); the even multipolar mode (n=2) is not observed due to the light polarization here employed [[29–31]]. For all the transmission spectra shown in Fig. 4 we employed as a reference the spectrum of a flat PDMS sample.

These results are summarized in Fig. 5, where the plasmon resonance wavelengths are plotted versus the NW width w, both for the dipolar (n=1) as well as for the multipolar (n=3) modes. For NW of increasing width an almost linear redshift of the dipolar mode (n=1) as well as of the multipolar mode (n=3) is observed.

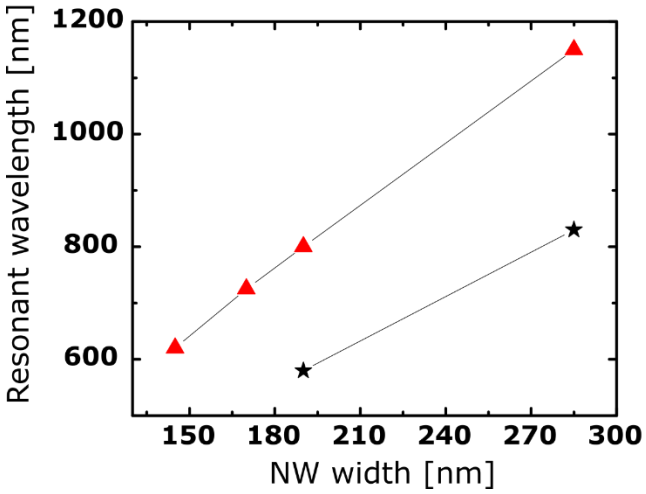

Figure 5: *Localized Surface Plasmon Resonance wavelength of dipolar modes (red triangles) and multipolar modes (black stars) as a function of the NW width.*

This demonstrates that by increasing the periodicity of the PDMS wrinkles towards the submicrometer range, it is possible to easily confine the growth of tilted Au nanowires whose width exceeds several hundred nm, well beyond the quasistatic limit, for which strong depolarization effects become relevant [32]. This enables a very effective redshift of the LSP resonance from the VIS to the NIR range of the EM spectrum.

Additonally we notice that, when the width of the Au nanostripes decreases, the multipolar resonances blueshift and their cross section is depressed as also observed in similar experiments performed on Au nanorods [39]. Moreover, when the higher order resonances are blueshifted below the onset of the Au interband transitions, in the range of 550 nm, a very effective decay channel becomes available and the multipolar resonances become strongly damped. In practical terms this means that the multipolar modes are observable only for nanostripes with a width exceeding about 180 nm as also reported in [38] for lithographically prepared nanorods of variable length.

Robustness of the Au/PDMS nanoarrays plasmonic properties under mechanical strain

The robustness of the plasmonic and optical properties of the Au NW/PDMS against mechanical deformation of the polymer template has been verified by comparing the optical response after repeating mechanical stress cycles. In Fig. 6 we show the optical spectra and the LSPR wavelength measured of Sample A in-situ under tensile strain conditions up to 30%. Fig 6a refers to transmittance of the sample when strain is applied orthogonally to the NW axis. After the strain cycle is completed and stress is released, the transmittance spectrum (dashed black curve) differs by less than a 5% relative to the unstretched sample (solid black curve). We highlight that the LSPR wavelength is essentially unchanged regardless of the amount of stretching applied as evidenced by Fig. 6b. Fig 6c shows the optical transmittance of the sample when tensile strain is applied parallel to the NW axis. After the stress cycle is completed and stress is released, transmittance (dashed black curve) again differs by less than a 5% with respect to the unstretched sample (solid black curve). The LSPR wavelength is stable within 1% in comparison to the unstretched sample LSPR wavelength. This demonstrates the robustness of the rippled PDMS/Au NW system under the investigated mechanical stress conditions. We also highlight that the LSPR wavelength doesn't change appreciably even if the periodicity of the underlying PDMS grating is changed accordingly by up to 30% during the strain cycles. This further demonstrates that the transmission dips attributed to the plasmon resonances are characterized by a localized and non-dispersive nature.

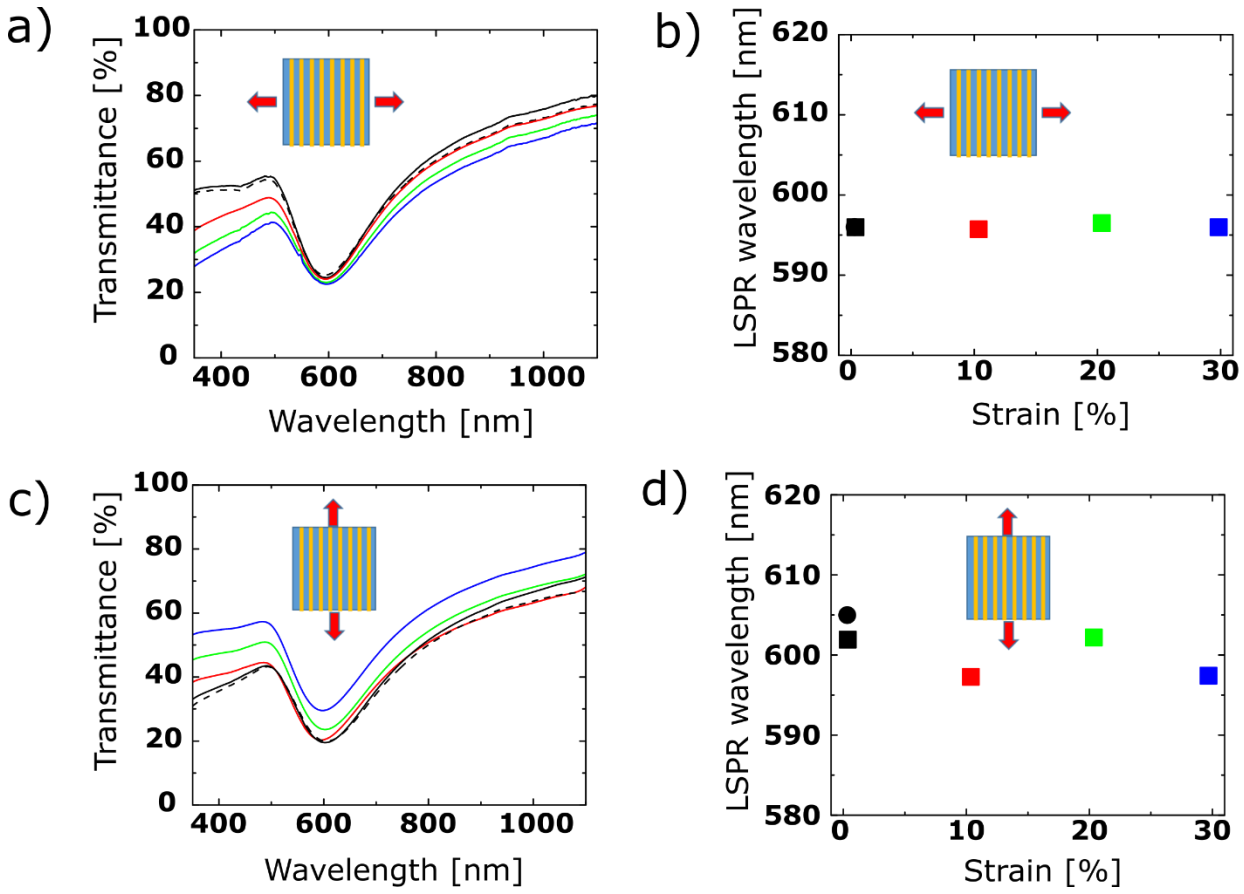

***Figure 6**: (a, c) Transmittance spectra acquired while tensile strain is applied to the Au NW axis, either orthogonal (a) or parallel to their axis (c). The different curves are associated with different relative stretching amounts: 0% (solid black curve), 10% (red curve), 20% (green curve), 30% (blue curve), 0% after one stress cycle is performed (dashed black curve). (b, d) Peak position of LSPR excitation as a function of the applied strain either orthogonal (b) or parallel (d) to their axis. 0% (black square) and 0% after one stress cycle (black circle) essentially coincides in middle panel of Fig. 6b, while the are distinguishable in Fig. 6d.*

The possibility to produce substrates doped with metal NW arrays supporting localized plasmon resonances in the NIR spectral range is of particular interest in view of Raman SERS applications when a low fluorescence background is mandatory. Indeed, a red-shift of the pump laser wavelength from the more conventional 532 nm or 633 nm excitation wavelengths towards 785 nm and 1064 nm in general allows to shift the characteristic Raman lines out from the substrate

fluorescence manifold, but at the expense of a substantial drop of the Raman signal intensity which follows a $1/\lambda^4$ trend. The use of substrates doped with plasmonic nanoarrays whose plasmon resonances can be tuned to match the pump laser wavelength would thus allow to increase the EM intensity in the near-field regions to compensate the decrease of Raman cross section at higher wavelengths [33]. The SERS experiments performed on Au/PDMS templates prepared by soft lithography [20] suggest that substantial Raman amplification factors in the range of 10^4 should be expected also for the Au nanostripes on wrinkled PDMS. More in general, the availability of flexible templates capable of shifting the plasmonic resonance from the VIS deep into the NIR spectral range appears relevant in view of plasmon-enhanced applications for bio-sensing and opto-electronics applications [34–36].

Au/PDMS nanoarrays as semi-transparent, flexible plasmonic electrodes

In view of a possible application of the Au NW arrays supported on PDMS as flexible semi-transparent electrodes, their electrical transport properties have been tested by measuring the sheet resistance between two electrodes separated by macroscopic distances in the range of 5 mm (see inset of Fig. 7). In Fig. 7 we also show the TM (red curve) and TE (black curve) optical spectra acquired on a PDMS substrate after the growth of Au NW with h= 50 nm, a high dose which is well beyond the electrical percolation threshold. Such a sample exhibits a longitudinal sheet resistance as low as 15 Ω/sq, a figure which is competitive with the best transparent conductive oxides based on ITO or on metal NW electrodes [37]. Previous experiments performed under comparable glancing angle deposition conditions on less ordered glass templates evidenced that the electrical percolation threshold shifts to lower coverages in the range of 20 nm [38]. This delay of percolation at higher Au doses on the PDMS templates is due to the extreme order of their ripple pattern in comparison to the glass case, where the inter-wire percolation is in fact favoured by the presence of dislocations and defects which separate individual NWs. The shadowing evaporation conditions ensured by the highly ordered PDMS ripple pattern on one hand hinder the lateral connection of adjacent NW (and thus electrical percolation), but on the other ensures a controllable degree of optical transparency in the uncovered portions of the PDMS pattern. In the example of Fig. 7, despite the considerable amount of deposited Au, the sample is still semi-transparent with a mean transmission of about 20%. In properly optimized experiments, which go beyond the scope of this work, one could expect to increase the optical transparency of the NW electrodes in the

60% range while still keeping the sheet resistance below 50 Ω /sq by simply acting on the template morphology, on the Au deposition angle and on Au dose [38].

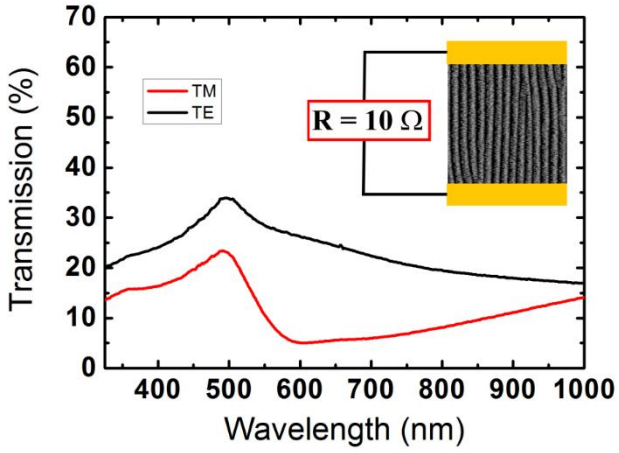

Figure 7: *Extinction spectra with polarized light in TE (black line) and TM (red line) directions, measured on thick Au NW (h=50 nm). The longitudinal sheet resistance of this sample measures 15 Ω/sq.*

Summing up the wrinkled PDMS samples doped with Au NW arrays own multifunctional properties (conductivity, transparency, tunable plasmonic response, flexibility, substrate nanostructuration) that make them appealing in a broad range of applications extending from optoelectronics, to energy harvesting and sensing applications [34–36]. As a case in point, we mention that noble metal NW matrixes confined on the rippled surface of flexible polymeric (PDMS) substrates have recently been employed as the core building blocks of ultra-sensitive capacitive pressure sensors [39,40]. In these approaches, a complex multi-step process involving the alignment of Au nanowires from solution has been employed to form the top electrode on a rippled PDMS interface. Our experimental approach can be easily tailored to offer a single step and cost effective alternative to fabricate these novel sensing platforms on large area substrates employing standard equipment scalable at the industrial level.

2.2 - Conclusions

Anisotropic wrinkling of Polydimethylsiloxane polymer templates has been achieved recurring to air plasma treatment on pre-stretched samples. The rippled templates are employed for the

confinement of anisotropic plasmonic nanostructures. Ordered self-organized polycrystalline gold nanowires (NW) with length up to tens of micrometers are formed by thermal deposition at grazing incidence. The investigation of the optical properties of the NW arrays showed a strong dichroic response of the Au NW/PDMS in the visible-near infrared spectral region. For light polarization parallel to the NW long axis the optical response resembles that of continuous flat films. For polarized light in the direction orthogonal to the NW long axis, Localized Surface Plasmon Resonance of both dipolar and multipolar nature are excited. The LSPR wavelength can be tailored in a broad spectral range extending from 600 nm up to 1150 nm in the IR range of the spectrum, by modifying the NW aspect ratio and the periodicity and height of the PDMS undulations. The possibility to efficiently tune the Au structures LSPR into the infrared range of the spectrum makes these samples excellent candidates for molecular and biosensing applications like e.g. in SERS: in this respect we exploited the retardation effects which become significant when the width of the Au NWs exceeds beyond the quasi-static limit. The optical and plasmonic properties of the Au NW/PDMS are preserved even after considerable tensile mechanical stress is exerted upon the system. Excellent electrical transport properties are observed in the direction parallel to the NW while still preserving sample transparency. The results suggest that the Au NW/PDMS could be employed in a broad range of applications, like e.g. wire grid polarizers, substrates for plasmon-enhanced spectroscopies and as flexible transparent electrodes.

2.3 - Experimental section

PDMS template fabrication

A 10:1 weight ratio mixture of PDMS pre-polymer and curing agent (Sylgard 184, Dow Corning) was prepared and left 20 min at room temperature (RT) for degassing. Afterwards, the solution was casted on a flat glass slide, confined by a rectangular Teflon stamp (2 mm thick). After further 20 min of degassing at RT, a second flat glass slide was positioned on top, in order to obtain a PDMS sample with two parallel surfaces. In this way, it is possible to avoid artefacts in the optical measurements.

The sample was left 12 hours at RT followed by a final annealing at 70°C for 2 h in order to complete the polymer reticulation process. After that, both glass slides were removed and a flat PDMS sample (approximately 10 mm x 20 mm x 2 mm) was obtained.

Wrinkling of the PDMS surface

Two methods have been employed to fabricate rippled surfaces: (i) air and oxygen plasma treatment was performed in a Tucan 1 Gambetti Chamber at the pressure of 0.5 mbar with variable power and time. (ii) Ion Beam Sputtering (IBS) was performed in a High Vacuum (HV) chamber by means of Ar+ ion irradiation at normal incidence by a defocused beam at 4.0×10^{-4} mbar of pressure (5.0N purity), generated from a gridded multi-aperture ion source (TECTRA), at the energy of 800 eV. The base pressure in the vacuum chamber was in the order of 10^{-7}mbar. In both processes, the PDMS sample was stretched by a home-made setup (with an accuracy of 0.1 mm) before being introduced into the chambers and undergoing the treatment.

Substrate morphology analysis

The sample morphology was characterized by a commercial Atomic Force Microscope (AFM, Nanosurf S Mobile), operating in tapping mode. In Fig. 8(a-d) top panels we show AFM topographies of the different rippled PDMS samples A, B, C and D. We also show self-correlation functions (middle panels) and lines profiles (bottom panels) extracted from the AFM topographies. From the statistical analysis of this data we derived the templates average periodicity λ (self-correlation functions), amplitude A (line profiles), and ripples local slopes θ for samples A, B, C and D reported in Table 1 in the "Results and discussion section".

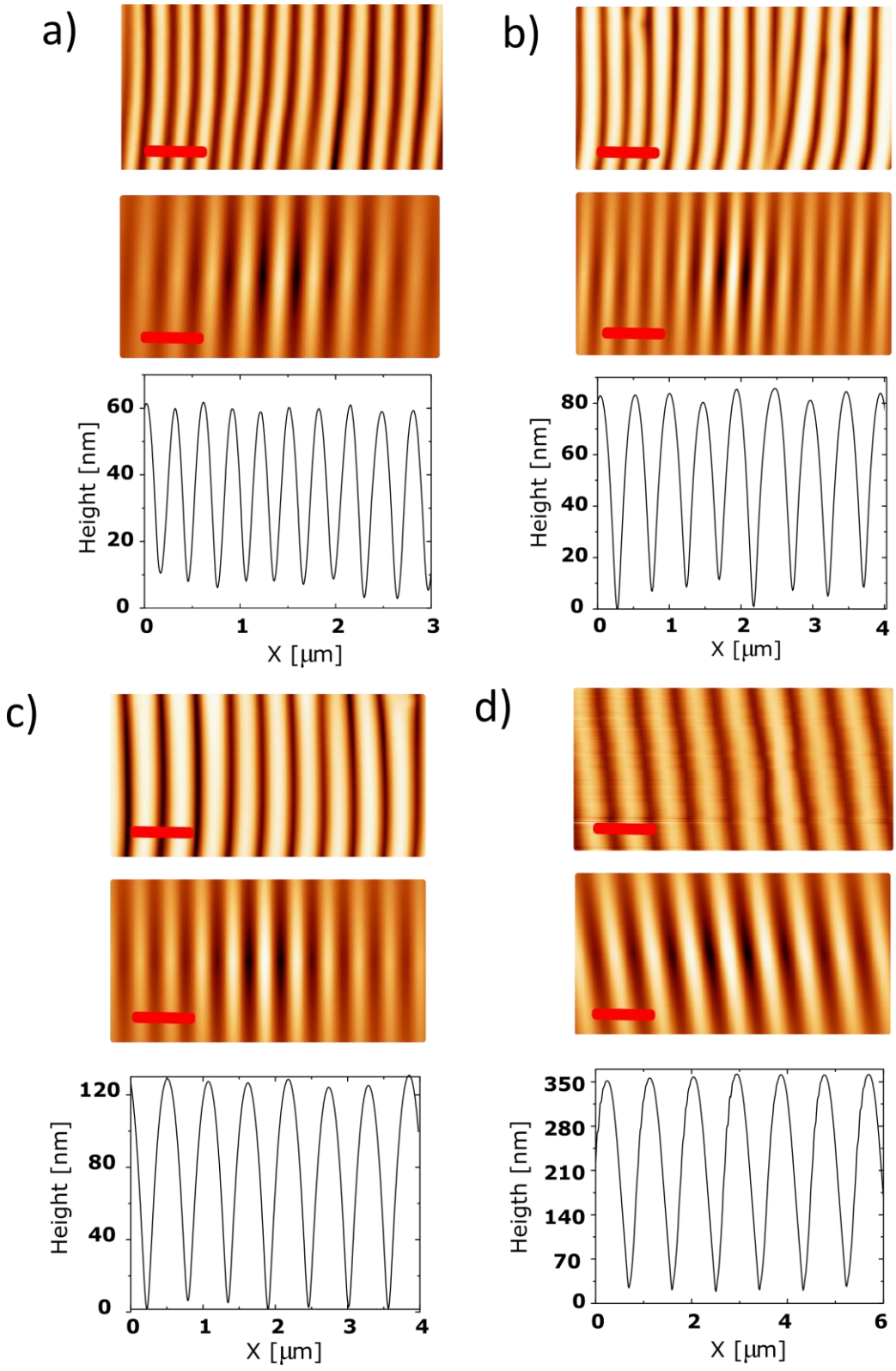

Figure 8: *AFM topography (top panel), self-correlation function (middle panel) and line profile (bottom panel) of: a) sample A. The red scale bar corresponds to 800 nm. b) sample B. The red*

scale bar corresponds to 1.2 μm. c) sample C. The red scale bar corresponds to 1.4 μm d) sample D. The red scale bar corresponds to 3.0 μm.

NW growth

Gold was thermally evaporated at grazing incidence in the same vacuum chamber used for the IBS. The amount of deposited material was monitored during the evaporation by a quartz microbalance.

Sample imaging and width statistics

A Scanning Electron Microscope (Hitachi VP-SEM SU3500) was employed to acquire images of the Au NW. In the upper panels of Fig. 9(a-d) I show the SEM topographs of Au NW supported on the different PDMS templates, corresponding to sample A, B, C and D respectively. In the lower panels of Fig. 9(a-d) I show histograms of the statistical analysis NW transversal width $w_{//}$ projected on the horizontal plane derived by ImageJ software. The average values of $w_{//}$ read resplectively: 136, 159, 172 and 236 nm. The uncertainty of the average value is assumed to be +/- 5 nm, correspondig the the instrumental resolution, since the computed standard error is below this limit.

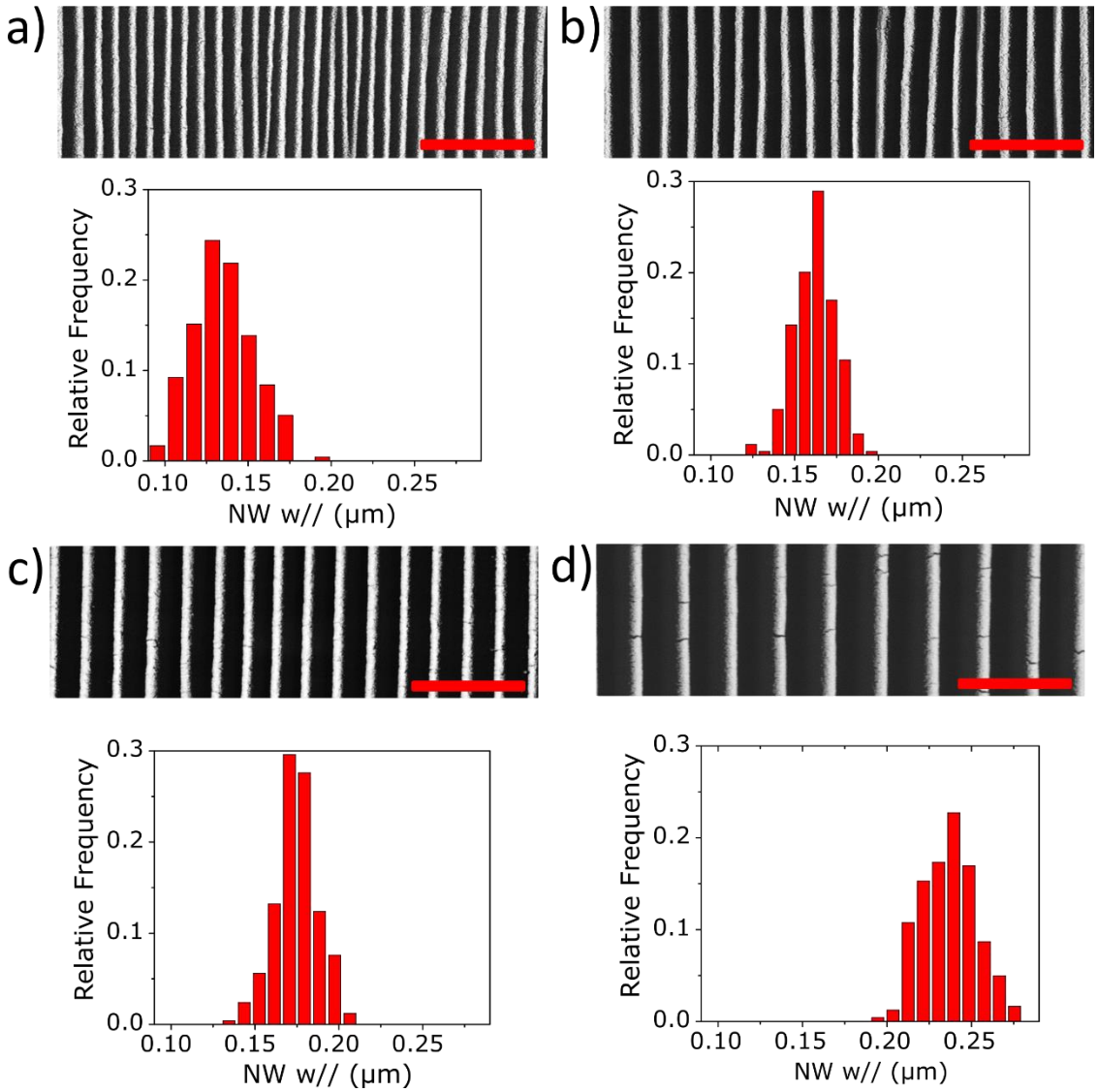

Figure 9: *SEM topographs acquired in the backscattering channel (top panels) and histograms of the statistical analysis NWs transversal width $w_{//}$ (bottom panels) for: a) sample A. b) sample B. c) sample C. d) sample D. The red scale bars correspond to 3.0 μm for all images.*

<u>*Optical measurements*</u>

The optical properties of the samples were studied by extinction spectroscopy both in-situ and ex-situ. We employed a spectrometer (HR4000, Ocean Optics) operating in the wavelength range 300÷1100 nm. Measurements in NIR/IR range of the spectrum were performed with Arcoptix FT-NIR fiber-coupled spectrometer. Halogen and deuterium sources provided light, which was fibre coupled to the UHV chamber for in-situ measurements. The anisotropic optical response of the

samples was investigated by changing the polarization of the incidence light from transverse magnetic (TM - electric field perpendicular to the NW axis) to transverse electric (TE - electric field parallel to the NW axis).

References

(1) Aksu, S.; Huang, M.; Artar, A.; Yanik, A. A.; Selvarasah, S.; Dokmeci, M. R.; Altug, H. Flexible Plasmonics on Unconventional and Nonplanar Substrates. *Advanced Materials* **2011**, *23* (38), 4422–4430. https://doi.org/10.1002/adma.201102430.

(2) Dunklin, J. R.; Forcherio, G. T.; Keith Roper, D. Gold Nanoparticle-Polydimethylsiloxane Films Reflect Light Internally by Optical Diffraction and Mie Scattering. *Materials Research Express* **2015**, *2* (8), 085005. https://doi.org/10.1088/2053-1591/2/8/085005.

(3) Johnston, I. D.; McCluskey, D. K.; Tan, C. K. L.; Tracey, M. C. Mechanical Characterization of Bulk Sylgard 184 for Microfluidics and Microengineering. *Journal of Micromechanics and Microengineering* **2014**, *24* (3), 035017. https://doi.org/10.1088/0960-1317/24/3/035017.

(4) Choi, K. M.; Rogers, J. A. A Photocurable Poly(Dimethylsiloxane) Chemistry Designed for Soft Lithographic Molding and Printing in the Nanometer Regime. *Journal of the American Chemical Society* **2003**, *125* (14), 4060–4061. https://doi.org/10.1021/ja029973k.

(5) Benight, S. J.; Wang, C.; Tok, J. B. H.; Bao, Z. Stretchable and Self-Healing Polymers and Devices for Electronic Skin. *Progress in Polymer Science* **2013**, *38* (12), 1961–1977. https://doi.org/10.1016/j.progpolymsci.2013.08.001.

(6) Song, W.; Vasdekis, A. E.; Psaltis, D. Elastomer Based Tunable Optofluidic Devices. *Lab on a Chip* **2012**, *12* (19), 3590. https://doi.org/10.1039/c2lc40481h.

(7) Halldorsson, S.; Lucumi, E.; Gómez-Sjöberg, R.; Fleming, R. M. T. Advantages and Challenges of Microfluidic Cell Culture in Polydimethylsiloxane Devices. *Biosensors and Bioelectronics* **2015**, *63*, 218–231. https://doi.org/10.1016/j.bios.2014.07.029.

(8) Alrifaiy, A.; Lindahl, O. A.; Ramser, K. Polymer-Based Microfluidic Devices for Pharmacy, Biology and Tissue Engineering. *Polymers* **2012**, *4* (3), 1349–1398.

https://doi.org/10.3390/polym4031349.

(9) Baudoin, R.; Alberto, G.; Paullier, P.; Legallais, C.; Leclerc, E. Parallelized Microfluidic Biochips in Multi Well Plate Applied to Liver Tissue Engineering. *Sensors and Actuators B: Chemical* **2012**, *173*, 919–926. https://doi.org/10.1016/j.snb.2012.06.050.

(10) Ren, K.; Zhou, J.; Wu, H. Materials for Microfluidic Chip Fabrication. *Accounts of Chemical Research* **2013**, *46* (11), 2396–2406. https://doi.org/10.1021/ar300314s.

(11) Jiang, Y.; Wang, H.; Li, S.; Wen, W. Applications of Micro/Nanoparticles in Microfluidic Sensors: A Review. *Sensors* **2014**, *14* (4), 6952–6964. https://doi.org/10.3390/s140406952.

(12) Buonomenna, M. G.; Bae, J. Organic Solvent Nanofiltration in Pharmaceutical Industry. *Separation & Purification Reviews* **2015**, *44* (2), 157–182. https://doi.org/10.1080/15422119.2014.918884.

(13) Seethapathy, S.; Górecki, T. Applications of Polydimethylsiloxane in Analytical Chemistry: A Review. *Analytica Chimica Acta* **2012**, *750*, 48–62. https://doi.org/10.1016/j.aca.2012.05.004.

(14) Kapridaki, C.; Maravelaki-Kalaitzaki, P. TiO2–SiO2–PDMS Nano-Composite Hydrophobic Coating with Self-Cleaning Properties for Marble Protection. *Progress in Organic Coatings* **2013**, *76* (2–3), 400–410. https://doi.org/10.1016/j.porgcoat.2012.10.006.

(15) Ryu, D.; Loh, K. J.; Ireland, R.; Karimzada, M.; Yaghmaie, F.; Gusman, A. M. In Situ Reduction of Gold Nanoparticles in PDMS Matrices and Applications for Large Strain Sensing. *Smart Structures and Systems* **2011**, *8* (5), 471–486. https://doi.org/10.12989/sss.2011.8.5.471.

(16) Zhou, J.; Khodakov, D. A.; Ellis, A. V.; Voelcker, N. H. Surface Modification for PDMS-Based Microfluidic Devices. *ELECTROPHORESIS* **2012**, *33* (1), 89–104. https://doi.org/10.1002/elps.201100482.

(17) Jin, M.; Feng, X.; Xi, J.; Zhai, J.; Cho, K.; Feng, L.; Jiang, L. Super-Hydrophobic PDMS Surface with Ultra-Low Adhesive Force. *Macromolecular Rapid Communications* **2005**, *26* (22), 1805–1809. https://doi.org/10.1002/marc.200500458.

(18) Giordano, M. C.; de Mongeot, F. B. Anisotropic Nanoscale Wrinkling in Solid-State Substrates. *Advanced Materials* **2018**, *30* (30), 1801840. https://doi.org/10.1002/adma.201801840.

(19) Park, H.-G.; Jeong, H.-C.; Jung, Y. H.; Seo, D.-S. Control of the Wrinkle Structure on Surface-Reformed Poly(Dimethylsiloxane) via Ion-Beam Bombardment. *Scientific Reports* **2015**, *5* (1). https://doi.org/10.1038/srep12356.

(20) Repetto, D.; Giordano, M. C.; Foti, A.; Gucciardi, P. G.; Mennucci, C.; Buatier de Mongeot, F. SERS Amplification by Ultra-Dense Plasmonic Arrays on Self-Organized PDMS Templates. *Applied Surface Science* **2018**, *446*, 83–91. https://doi.org/10.1016/j.apsusc.2018.02.163.

(21) Giordano, M. C.; Longhi, S.; Barelli, M.; Mazzanti, A.; Buatier de Mongeot, F.; Della Valle, G. Plasmon Hybridization Engineering in Self-Organized Anisotropic Metasurfaces. *Nano Research* **2018**, *11* (7), 3943–3956. https://doi.org/10.1007/s12274-018-1974-3.

(22) Oh, S. H.; Kim, J. G.; Kim, C. S.; Choi, D. S.; Chang, S.; Jeong, M. Y. The Fabrication of 3-D Nanostructures by a Low- Voltage EBL. *Applied Surface Science* **2011**, *257* (9), 3817–3823. https://doi.org/10.1016/j.apsusc.2010.11.155.

(23) Kim, P.; Hu, Y.; Alvarenga, J.; Kolle, M.; Suo, Z.; Aizenberg, J. Rational Design of Mechano-Responsive Optical Materials by Fine Tuning the Evolution of Strain-Dependent Wrinkling Patterns. *Advanced Optical Materials* **2013**, *1* (5), 381–388. https://doi.org/10.1002/adom.201300034.

(24) Owen, M. J.; Smith, P. J. Plasma Treatment of Polydimethylsiloxane. *Journal of Adhesion Science and Technology* **1994**, *8* (10), 1063–1075. https://doi.org/10.1163/156856194X00942.

(25) Genzer, J.; Groenewold, J. Soft Matter with Hard Skin: From Skin Wrinkles to Templating and Material Characterization. *Soft Matter* **2006**, *2* (4), 310. https://doi.org/10.1039/b516741h.

(26) Béfahy, S.; Lipnik, P.; Pardoen, T.; Nascimento, C.; Patris, B.; Bertrand, P.; Yunus, S. Thickness and Elastic Modulus of Plasma Treated PDMS Silica-like Surface Layer. *Langmuir* **2010**, *26* (5), 3372–3375. https://doi.org/10.1021/la903154y.

(27) Horcas, I.; Fernández, R.; Gómez-Rodríguez, J. M.; Colchero, J.; Gómez-Herrero, J.; Baro,

A. M. WSXM : A Software for Scanning Probe Microscopy and a Tool for Nanotechnology. *Review of Scientific Instruments* **2007**, *78* (1), 013705. https://doi.org/10.1063/1.2432410.

(28) Nania, M.; Matar, O. K.; Cabral, J. T. Frontal Vitrification of PDMS Using Air Plasma and Consequences for Surface Wrinkling. *Soft Matter* **2015**, *11* (15), 3067–3075. https://doi.org/10.1039/C4SM02840F.

(29) Laurent, G.; Félidj, N.; Aubard, J.; Lévi, G.; Krenn, J. R.; Hohenau, A.; Schider, G.; Leitner, A.; Aussenegg, F. R. Evidence of Multipolar Excitations in Surface Enhanced Raman Scattering. *Physical Review B* **2005**, *71* (4). https://doi.org/10.1103/PhysRevB.71.045430.

(30) Encina, E. R.; Coronado, E. A. Resonance Conditions for Multipole Plasmon Excitations in Noble Metal Nanorods. *The Journal of Physical Chemistry C* **2007**, *111* (45), 16796–16801. https://doi.org/10.1021/jp075880j.

(31) Payne, E. K.; Shuford, K. L.; Park, S.; Schatz, G. C.; Mirkin, C. A. Multipole Plasmon Resonances in Gold Nanorods. *The Journal of Physical Chemistry B* **2006**, *110* (5), 2150–2154. https://doi.org/10.1021/jp056606x.

(32) Maier, S. A. *Plasmonics: Fundamentals and Applications*; Springer: New York, 2007.

(33) Nie, S. Probing Single Molecules and Single Nanoparticles by Surface-Enhanced Raman Scattering. *Science* **1997**, *275* (5303), 1102–1106. https://doi.org/10.1126/science.275.5303.1102.

(34) Kang, H.; Jung, S.; Jeong, S.; Kim, G.; Lee, K. Polymer-Metal Hybrid Transparent Electrodes for Flexible Electronics. *Nature Communications* **2015**, *6* (1). https://doi.org/10.1038/ncomms7503.

(35) Lee, M.-S.; Lee, K.; Kim, S.-Y.; Lee, H.; Park, J.; Choi, K.-H.; Kim, H.-K.; Kim, D.-G.; Lee, D.-Y.; Nam, S.; et al. High-Performance, Transparent, and Stretchable Electrodes Using Graphene–Metal Nanowire Hybrid Structures. *Nano Letters* **2013**, *13* (6), 2814–2821. https://doi.org/10.1021/nl401070p.

(36) Lee, P.; Lee, J.; Lee, H.; Yeo, J.; Hong, S.; Nam, K. H.; Lee, D.; Lee, S. S.; Ko, S. H. Highly Stretchable and Highly Conductive Metal Electrode by Very Long Metal Nanowire Percolation Network. *Advanced Materials* **2012**, *24* (25), 3326–3332.

https://doi.org/10.1002/adma.201200359.

(37) Chiappe, D.; Toma, A.; de Mongeot, F. B. Transparent Plasmonic Nanowire Electrodes via Self-Organised Ion Beam Nanopatterning. *Small* **2013**, *9* (6), 913–919. https://doi.org/10.1002/smll.201201146.

(38) Giordano, M. C.; Repetto, D.; Mennucci, C.; Carrara, A.; Mongeot, F. B. de. Template-Assisted Growth of Transparent Plasmonic Nanowire Electrodes. *Nanotechnology* **2016**, *27* (49), 495201. https://doi.org/10.1088/0957-4484/27/49/495201.

(39) Joo, Y.; Byun, J.; Seong, N.; Ha, J.; Kim, H.; Kim, S.; Kim, T.; Im, H.; Kim, D.; Hong, Y. Silver Nanowire-Embedded PDMS with a Multiscale Structure for a Highly Sensitive and Robust Flexible Pressure Sensor. *Nanoscale* **2015**, *7* (14), 6208–6215. https://doi.org/10.1039/C5NR00313J.

(40) Shuai, X.; Zhu, P.; Zeng, W.; Hu, Y.; Liang, X.; Zhang, Y.; Sun, R.; Wong, C. Highly Sensitive Flexible Pressure Sensor Based on Silver Nanowires-Embedded Polydimethylsiloxane Electrode with Microarray Structure. *ACS Applied Materials & Interfaces* **2017**, *9* (31), 26314–26324. https://doi.org/10.1021/acsami.7b05753.

CHAPTER 3

Plasmon hybridization engineering in self-organized anisotropic dimers

Introduction

Recently, the possibility to fabricate hybrid metal/dielectric plasmonic nanostructures gained increasing attention. Such subwavelength heterostructures can be considered metamaterials, as their properties are radically different from their isolated constituent materials. Let's e.g. consider the case of "nanosandwiches", vertically stacked structures grown on a dielectric substrate, made-up by two layers of metal separated by a layer of dielectric material. In the example presented in Fig. 1a we can consider the geometry adopted in ref. [1] where two gold nanodisks are separated by a silica layer of the same size. Illuminating the sample with photons of appropriate wavelength it's possible to excite Localized Surface Plasmons (LSP) on both gold nanodisks. The oscillating electrical dipoles exctited on the two disks will interact when the dielectric layer separating them is sufficiently thin leading to the hybridization of the two single disk plasmonic modes. We have then two hybrid modes: a mode of higher energy (dipolar electric or anti-bonding mode) and a mode of lower energy (dipolar magnetic or bonding mode), as can be appreciated in Fig. 1b by comparing the blue trace corresponding to a single Au disk capped by the dielectric layer, and the black trace corresponding to the "sandwich" structure.

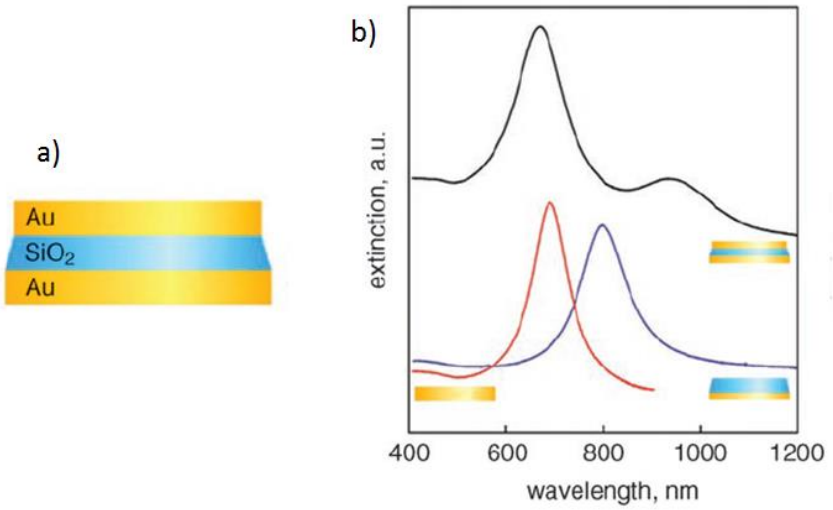

***Figure 1**: a) Sketch of a "nanosandwich" made by 3 layers (metal/dielectric/metal) of equal thickness. b) Exctincion spectra of a sinlge Au nanodisk (red curve), Au nanodisk + oxide layer (blue curve) and complete "nanosandwich" (black curve).*

In the high energy mode the two dipoles oscillate in phase, we can thus consider a single effective oscillating dipole and hence the "electric" mode name. In the low energy mode the dipoles oscillate in anti-phase and the transient currents inside the two nanodisk flow similarly to eddy currents in a spire forming a loop, with the magnetic field centered in the dielectric spacer and hence the name "magnetic" mode. Moreover, simulations suggest that a high field enhancement is produced by the dielectric magnetic mode over the edges of the nanosandwiches [[1]] and, even more importantly, provide hints on the way to tune the magnetic mode resonant wavelenght changing the different layer thickness and chemical composition (Fig. 2).

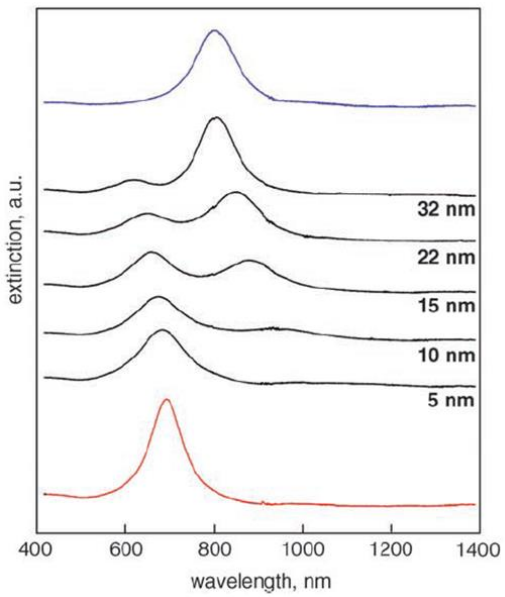

***Figure 2**: Tunability of the "nanosadwich" plasmonic properties. The red curve refers to a single Au disk with 20 nm of thickness, while the blue curve to a single Au nanodisk with 10 nm of thickness. The black curves refer to a nanosandwich with fixed Au layers (20 nm) and varying dielectric spacer thickness (from 5 to 32 nm). It can be seen how increasing the dielectric thickness the magnetic mode strongly blueshifts, while the electric mode decreases in intensity but stays relatively fixed in frequency.*

Plasmonic metasurfaces have been recently explored and engineered to achieve advanced optical functionalities in flat ultra-compact devices [2–4]. The general trend in this field is to increase the complexity of the individual elements of the patterns, so-called meta-atoms, in order to provide novel functionalities. For example, surface-enhanced coherent anti-Stokes Raman scattering (SECARS) through plasmonic Fano resonances [5] and flat-optics analog computing with gap-plasmon metasurfaces [6], have been recently demonstrated. These outstanding achievements were enabled by state-of-the-art nanofabrication technologies, in particular, electron-beam lithography (EBL) [7–10] and focused ion beam (FIB) milling [11–13]. However, these cleanroom techniques are not suitable in many applications where scalability and/or cost effectiveness are of key importance, in particular, for large-area applications such as photovoltaics [14,15], as well as in plasmon-enhanced bio-sensing, which requires inexpensive production methods with quantitative control and engineering capability at the nanoscale (see Refs. [16,17] for relevant examples of plasmon-

enhanced quantitative SERS). Various methods for large-area nanofabrication have been recently developed, including micro-contact printing (soft lithography) [18,19], nanoimprinting [20,21], lithographically patterned electrodeposition [22], and a large number of self-assembling (SA) and self-organization (SO) techniques (see Refs. [1,17,23–27] and references therein). The latter techniques are particularly suitable in terms of low production costs; however, they lack the many degrees of freedom offered by EBL and FIB. In particular, the self-assembled (SA) and self-organized (SO) techniques typically provide 2D meta-atoms with a monomeric configuration, usually in the form of isotropic nanoparticle or nanohole arrays with an electric dipole character of the plasmonic resonance [28–32]. Furthermore, more sophisticated dimeric and trimeric SA/SO configurations could be very beneficial for sub-radiant (and thus sharper) magnetic dipole resonances. To the best of our knowledge, until now, this is limited only to clusters [1,33,34] or disordered patterns [25], with no evidence of feasibility in highly ordered large-area structures obtained by SA/SO. If the number of available configurations of 2D SA/SO meta-atoms (such as the multi-layer nanodisk system previoulsy described) is limited, the situation is even worse for highly anisotropic (and eventually one-dimensional (1D)) configurations. The fabrication of such types of structures by SA/SO (and even by lithography assisted methods [35]) is significantly more challenging owing to the demand for both positional and orientational ordering over large area of the metasurfaces. However, they have potential to advance the SA/SO technology for plasmonic patterns, owing to the higher filling factor and homogeneity of the hot-spots, and can eventually provide novel functionalities related to the higher polarization sensitivity.

In my PhD work I employed a multistep approach based on wrinkling enhaced IBS soda-lime glass templates (described in section 1.2.3 of this thesis) and kinetically controlled deposition for the confinement and engineering of self-organized plasmonic patterns with quasi-1D hybrid MIM (metal/insulator/metal) meta-atoms [36]. Highly ordered plasmonic arrays of NWs with rectangular cross-sections (nanostrips) in monomeric and dimeric MIM configurations were fabricated, thus approaching the engineering capabilities of EBL and FIB but on a significantly larger area, using a parallel process. The optical quality of the patterns was evaluated by comparison with full-wave numerical simulations of the transmittance spectrum in the entire visible (VIS) and near-infrared (NIR) ranges, performed by Prof. Della Valle (Politecnico di Milano). In particular, the presence of magnetic dipole plasmonic resonance for the nanostrip dimer configuration is revealed, also referred to as a gap-plasmon (GP) resonator [37–40]. As previously commented, this type of

resonance is attributed to the hybridization of elementary plasmons in engineered dimeric meta-atoms, and leads to a superior sensitivity and higher field enhancement, compared with those of the dipolar plasmonic resonances for monomeric meta-atom configurations (see Refs. [39,41,42] and references therein). The magnetic dipole resonance is very sensitive to small variations of the morphological features of the meta-atoms; the activation and tailoring of these modes in the anisotropic SO plasmonic metasurfaces that will be presented in this chapter is thus a remarkable achievement, being the first example of fully self-assembled, large area GP in the state of the art, as far as our knowledge goes.

3.1 – Results and discussion

Fabrication of self-organized Au nanowire arrays on nanorippled glass templates

The wrinkling mechanism typical of soft organic matter, described in section 1.1 and in chapter 2 of this thesis, can enhance the nanopatterning of solid state, inorganic glass under ion irradiation, providing excellent rigid templates for the confinement of plasmonic structures, as described in section 1.2.3. These self-organized platforms will be exploited in the following chapters of the thesis for different large area plasmonic functionalizations.

Highly ordered ripple nanopatterns are prepared over a large area (order of cm^2) at the surface of a low-cost soda lime glass substrate using defocused IBS. During the IBS process, the substrate temperature is fixed at approximately 680 K in order to induce high-aspect-ratio nanostructures through ion-beam driven SO nanopatterning (see section 1.2.3 section for details and Ref. [43]). Under ion irradiation at an incidence angle of $\theta = 30°$, a quasi-1D large area ripple pattern is obtained (see Experimental section) as shown by the scanning electron microscopy (SEM) image of Fig. 3(a). In the atomic force microscopy (AFM) image of Fig. 3(b) highly anisotropic nanoripples, as long as several micrometers, are observed, which are characterized by a pronounced vertical dynamic range, exceeding 110 nm, and lateral periodicity of approximately 200 nm, as revealed from the 2D self-correlation pattern. The AFM line profile in Figs. 3(c) (not scaled) and 3(e) (scaled) evidence the ripple cross-section characterized by a typical height of approximately 80 nm and steep asymmetric faceted ridges. Indeed, the ridges exposed directly to the ion beam (negative values in the histogram of slope distribution in Fig. 3(d)) develop very steep facets whose measured slope reaches a value of –50°, which correspond to the deep grooves

of the pattern. It is worth noting that the broad slope distribution can be underestimated owing to tip convolution effects. The ripple ridges that are partially shadowed from the ion beam are less steep and characterized by a well-defined slope distribution with a peak at +30° (positive values in Fig. 2(d)).

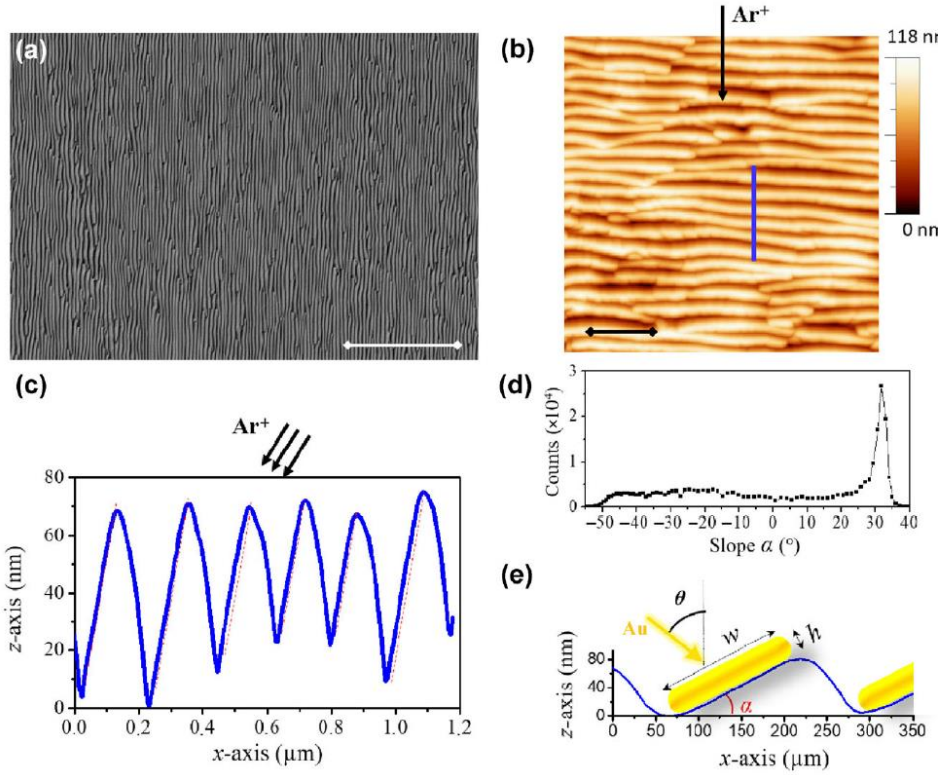

Figure 3: *(a) Large-area SEM image of the rippled glass template metalized with a thin Au film; the white scale-bar corresponds to 5 μm. (b) AFM topography of the SO glass ripple pattern; the black scale-bar corresponds to 800 nm, while the blue line corresponds to the AFM ripple profile in (c). AFM line profile (not scaled) of the ripple corresponding to the blue line. (d) Histogram of the slope distribution of the ripple pattern in (b). (e) Scaled AFM line profile of the rippled glass template, highlighting the asymmetric shape of the SO glass nanostructures, and illustration of the glancing-angle Au deposition procedure.*

These asymmetric faceted templates are desirable for effectively confined highly ordered quasi-1D arrays of plasmonic NWs with selected tilt and width, imposed by the ripple facets. As illustrated in Fig. 3(e), glancing angle gold deposition was performed perpendicularly to the ripple ridges with the Au-beam tilted at an angle of θ with respect to the surface normal. Under these

conditions, the local thickness of Au deposited on the selected facets is $h = t_0 \times \cos(\theta - \alpha)$, where t_0 represents the metal thickness that would be deposited on a flat surface normally oriented with respect to the Au beam, and α is the slope of the glass facet exposed to the Au beam. When a deposition angle of $\theta = 50°$ is selected, the Au-beam directly faces the ripple ridges tilted at $\alpha = +30°$ (as shown in the illustration), and laterally disconnected Au stripes are confined on the illuminated ridges, while the opposite facets remain completely shadowed. Under these conditions, the width of the Au-NWs' cross section is imposed by the ripple template, while the local thickness h can be easily tailored, as it is proportional to the selected dose t_0.

The scanning electron microscopy (SEM) image in Fig. 4(a), acquired with a backscattered electron detector, shows Au NW arrays confined at $\theta = 50°$ on the "wide" facets of the rippled glass template with a local Au thickness of $h = 22$ nm. The brighter regions in the image reveal the presence of aligned and laterally disconnected Au nanostrips reaching a length of several micrometers. The statistical distribution of the Au-NWs' projected width shown in Fig. 4(b), extracted from a series of SEM images, is unimodal with a peak at approximately $w_p = 87$ nm, reflecting the conformal growth of the NW arrays with a pronounced lateral order. Taking into account the tilt $\alpha = 30°$ of the facet, we derive the mean NW width $w = w_p / \cos(\alpha) = (100 \pm 10)$ nm, which corresponds to the size of the Au-illuminated ripple facets (Fig. 3(e)). The latter parameters are significantly improved compared with those of SO NW arrays prepared by direct IBS with polycrystalline Au films, which exhibit a very broad width (height) distribution in the range of 20–400 nm (5–40 nm) [44].

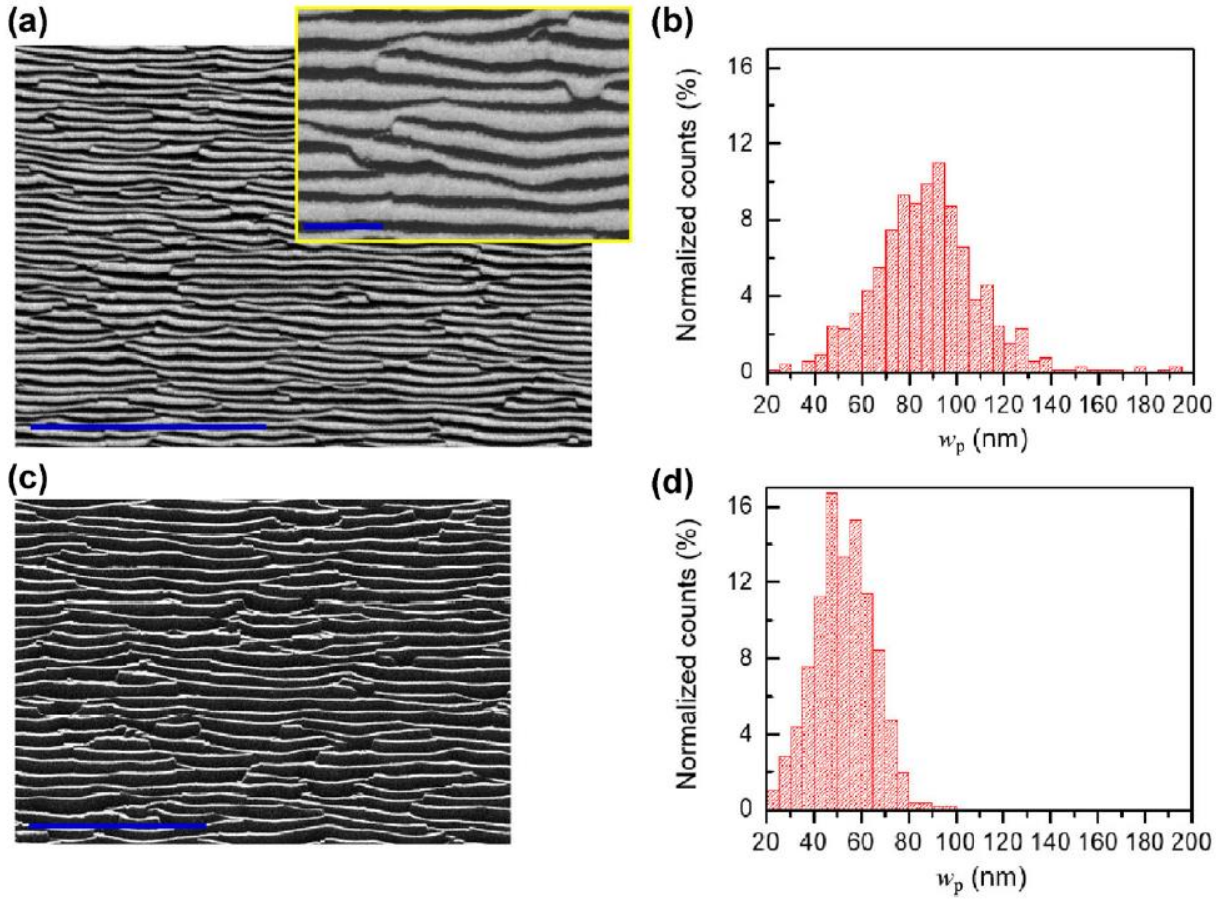

Figure 4: *(a) SEM images (back-scattered signal) of Au NW arrays confined on "wide" facets of rippled glass templates; the blue scale-bar corresponds to 4 μm. The inset shows a magnified SEM image of the same Au nanostripes; the scale-bar corresponds to 500 nm. (b) Statistical distribution of the width (wp) of the Au-NWs (shown in (a)) confined on the "wide" glass facets, projected on the sample plane. (c) SEM image and (d) statistics of the projected width wp of the Au-NWs confined on the "narrow" glass facets.*

In order to illustrate the possibility to tailor the geometrical parameters of the NWs, in Fig. 4(c) we show a SEM image of Au NW arrays confined on the "narrow" facets of the pattern, i.e., the steep ridges are tilted up to $\alpha = -50°$. In this case, metal evaporation was performed at $\theta = -70°$; the beam directly faced the steep ridges. The local thickness h was fixed to 22 nm. The statistical distribution of the projected width shown in Fig. 4(d) is unimodal, with a peak at a smaller value of approximately wp = 53 nm, which, considering the facet tilt, corresponds to an average NW width of $w = (82 \pm 10)$ nm. The NW arrays in Fig. 4 are expected to exhibit a well-defined and

anisotropic optical response in the VIS–NIR spectral range, owing to the excitation of localized plasmon resonances, whose wavelength can be tailored by modifying the NW shape. The breaking of the NWs along their major axis, at an average interval of approximately 2–3 μm (Fig. 4(a)), has two implications: (i) The translational invariance along this direction is broken beyond the spatial scale of the average length of the NWs; (ii) an inhomogeneous broadening of the plasmonic resonances can emerge, when the array is probed with large-area optical beams, as discussed below.

The optical behavior of the Au NW arrays was investigated by measuring the extinction spectra in the VIS–NIR spectral range. The samples were illuminated with a polarized VIS–NIR light beam (light-spot diameter: 5 mm), and the transmitted intensity was then acquired at normal incidence. Figure 5(a) shows the optical transmission spectra with longitudinal (TE-pol, solid curve) and transversal (TM-pol, dashed curve) light polarizations (with respect to the NWs' long axis (see inset of Fig. 5(a))). The blue curves represent the optical spectra that correspond to the Au confinement on the "wide" ripple facets, as illustrated in Fig. 3(e) and shown in the SEM image in Fig. 4(a). We observe a strong optical dichroism; for the longitudinal polarization (TE-pol), a decrease of the transmittance is detected for wavelengths smaller than 530 nm, owing to the excitation of Au interband transitions [45], similar to the optical response of a continuous Au thin film. For the transversal polarization (TM-pol), the transmission spectrum exhibits a pronounced transmission minimum (peak at 620 nm), attributed to the excitation of localized surface plasmon (LSP) resonance along the cross-section of the Au NWs. The gold wires are indeed laterally disconnected and characterized by a shape aspect ratio w/h of approximately 4.5, which corresponds to an LSP excitation in the VIS spectrum. The narrow distribution of the NWs' width w, shown in Fig. 4(b), leads to a reduced spectral dispersion of the plasmonic resonance (the full width at half maximum amounts approximately to 130 nm). A strong enhancement of the TM-pol transmittance with respect to the TE-pol signal is observed in the spectral regions far away from the LSP resonance, i.e., in the near ultraviolet (NUV)-blue and red-NIR ranges. In this spectral range, metallic arrays behave as wire grid polarizers owing to the strong plasmonic excitation (see Ref. [46] and references therein).

The plasmonic resonance of such arrays can be tailored in the VIS spectral range by performing Au deposition where the Au beam illuminates the steep and narrow facets of the rippled glass

template, i.e., those corresponding to negative slopes in the histogram in Fig. 3(d). When Au evaporation is performed at θ =70° with respect to the surface normal on the steep narrow facets, up to the same local thickness of h =22 nm, an array of narrow NWs separated by the large facets is formed, as shown in the SEM image in Fig. 4(c). The average periodicity is unchanged; however, the average width w decreases, hence the w/h aspect ratio decreases to approximately 3.7. Figure 5(a) shows the spectra (red) of this alternative 1D grating that is characterized by the same local thickness h, but different NWs' width w. Similar to the previous case, we observe a strong optical dichroism induced by the LSP excitation. However, the reduced NW aspect ratio w/h causes a significant blue-shift of the plasmonic peak down to 570 nm, while the FWHM of the resonance is reduced to approximately 70 nm. These results are in a quantitative agreement with those of the full-wave finite-element method (FEM) numerical simulations performed by Prof. Della Valle (Politecnico di Milano) (Fig. 5(b)).

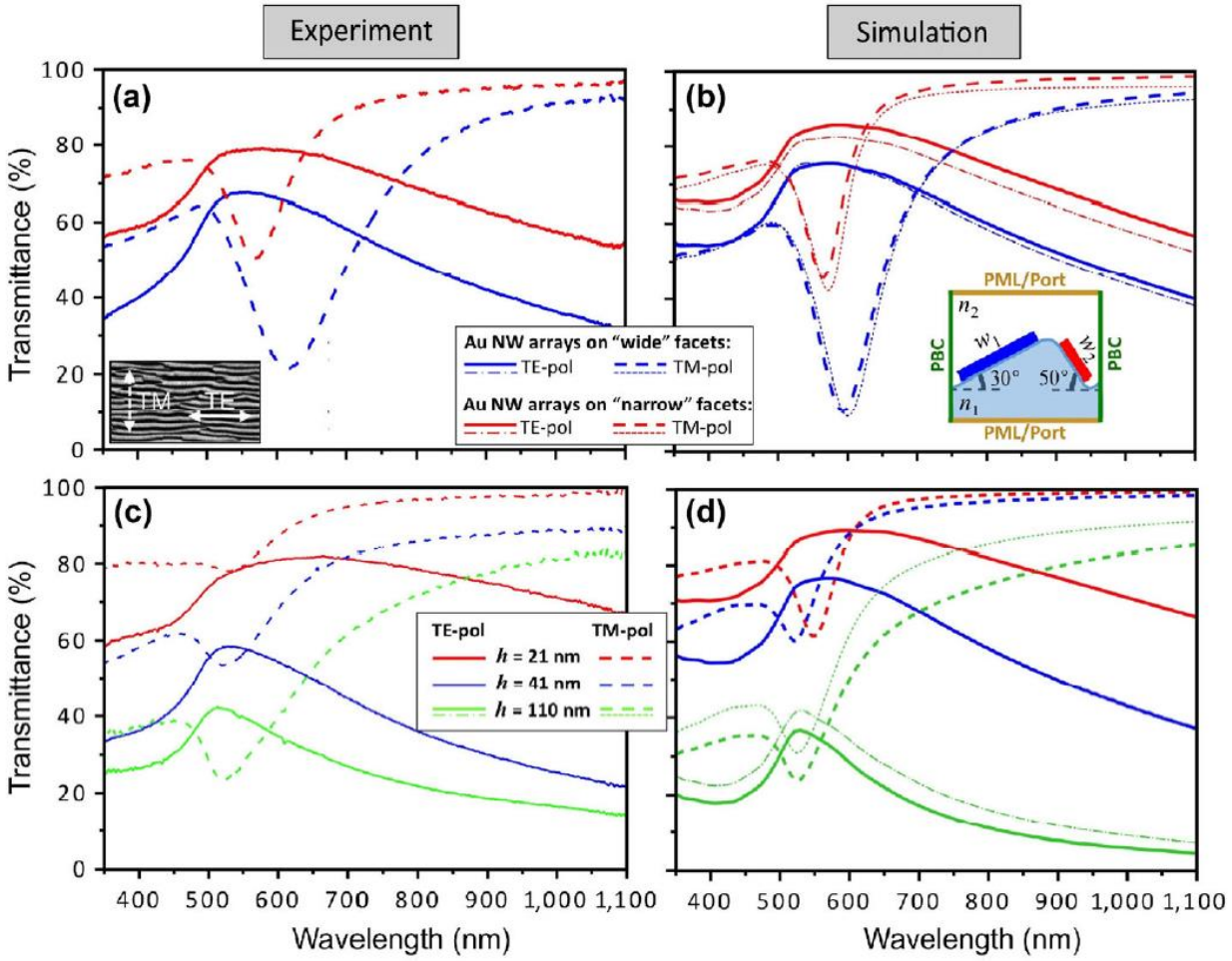

Figure 5: *(a) Measured and (b) calculated optical extinction spectra of the Au NW arrays confined*

on the rippled glass templates on the "wide" (blue trace curve) and "narrow" (red trace curve) facets of the pattern. The optical transmittance is shown for the longitudinal (TE-pol, solid trace curve) and transversal (TM-pol, dashed trace curve) polarizations of the light at normal incidence. The inset in (a) shows a top view of the sample; the arrows represent the electric fields under the TE (solid arrow) and TM (dashed arrow) polarizations. The inset in (b) illustrates the unit cell of the nanostrip array (period:~ 200 nm), employed for the numerical analysis (see Methods section for details). (c) Measured and (d) calculated optical extinction spectra of Au NW arrays confined on the "narrow" facets of the pattern. Red, blue, and green trace curves correspond to an increased Au local coverage with a thickness of h = 21, 41, and 110 nm, respectively. In the numerical simulations in (b) and (d), the heavy trace curves represent the simplified model with a symmetric environment (n1 = n2 = nef = 1.25) and scattered field formulation with perfectly matched layers (PML), whereas the light trace curves represent the more accurate model with a glass (n1 = 1.45) rippled substrate and air (n2 = 1) cover, obtained using the total field formulation with port boundary conditions.

An alternative approach to achieve fine tuning of the optical/plasmonic response of the NWs array is to change the aspect ratio *w*/*h* of the meta-atoms, similarly to the PDMS case descibed in the previous chapter, by varying this time the local thickness *h* of the NWs (i.e., by varying the deposited dose), while keeping constant their width *w*, which is solely determined by the size of the illuminated facets (a constant parameter if the glancing-angle deposition conditions are not modified). Figure 5(c) shows the optical extinction spectra of Au NWs deposited on narrow facets at 70°, for thicknesses *h* of 110, 41, and 21 nm. The mean optical transmittance gradually increases, while the LSP resonance red-shifts in a highly nonlinear manner. The red shift is negligible when *h* decreases from 110 to 41 nm; however, a further decrease to *h* = 21 nm leads to a red-shift of approximately 25 nm; this trend is also confirmed by the numerical simulations shown in Fig. 4(d). This highly nonlinear tunability of the plasmonic resonance with the aspect ratio, while keeping a constant *w*, is a signature of the retardation-based character of the LSP, typical for noble-metal nanostrip plasmonic resonators [47]. Therefore, we demonstrated the possibility to precisely confine highly ordered NWs arrays on SO faceted templates, achieving tunable plasmonic excitation in the visible range. Because of the limited width tunability of the glass template ripple periodicity, the NIR/IR range was not accessible as in the PDMS/Au NWs array described in chapter 2. In that case very wide Au NWs could be confined on the polymeric template and

retardation effects exploited to very efficiently redshits their LSPR.

Plasmon hybridization in self-organized plasmonic dimers

Owing to the high degree of order and slope selection, the SO arrays of tilted nanostrips represent a platform that enables natural lithography of vertically stacked metallic nanostrip dimers separated by a dielectric layer. Under this condition, a near-field coupling of the plasmonic fields of the individual nanostrips occurs, and multiple resonances are expected to appear owing to the plasmon hybridization [1,48,49]. Particularly intriguing for nanospectroscopy applications is the possibility to tune the plasmonic resonances in order to meet the requirements of the spectroscopy setup, and further increase the near-field enhancement, which is very beneficial for nonlinear spectroscopies such as SERS [50–53] and SECARS [4]. Electron beam lithography and ion-beam milling are widely employed fabrication methods to achieve plasmon hybridization in highly ordered nanostructure arrays, allowing complex configurations of meta-atoms, though on limited areas in the range of hundreds square micrometers [6,7]. However, as previously underlined, there are very few examples of plasmon hybridization engineering in SO/SA nanostructures, mostly dealing with clusters [1,54], or disordered patterns with a low flexibility in the available geometry of the meta-atoms, and consequently are less flexible in their optical response [18]. By employing the above SO method, I was able to combine the ability to pattern a relatively homogeneous metasurface, with an area on the order of square centimeter, with the control of the plasmon hybridization mechanism of highly anisotropic meta-atoms consisting of nanostrip dimers.

The 1D NWs arrays confined on the “wide” ripple facets (see the SEM image in Fig. 4(a)) with w = 100 nm and h = 30 nm are employed as a platform for the further growth of a silica layer with a thickness of s = 42 nm. The silica thin film is conformally grown on the Au NWs by sputtering deposition at an incidence angle of θ = 50° using a SiO2 target. Then, after a glancing-angle Au evaporation at θ = 50° up to a local thickness of h = 30 nm, a 1D array of tilted dimers of NWs is obtained, as illustrated in Fig. 6(a). SEM images in Figs. 6(b) and 6(c) show a top-view and cross-section of the SO Au-silica-Au dimers, respectively. The top-view image shows that the metal nanostrips are self-aligned and laterally disconnected according to the underlying pattern, as the Au NW arrays in Fig. 4(a).

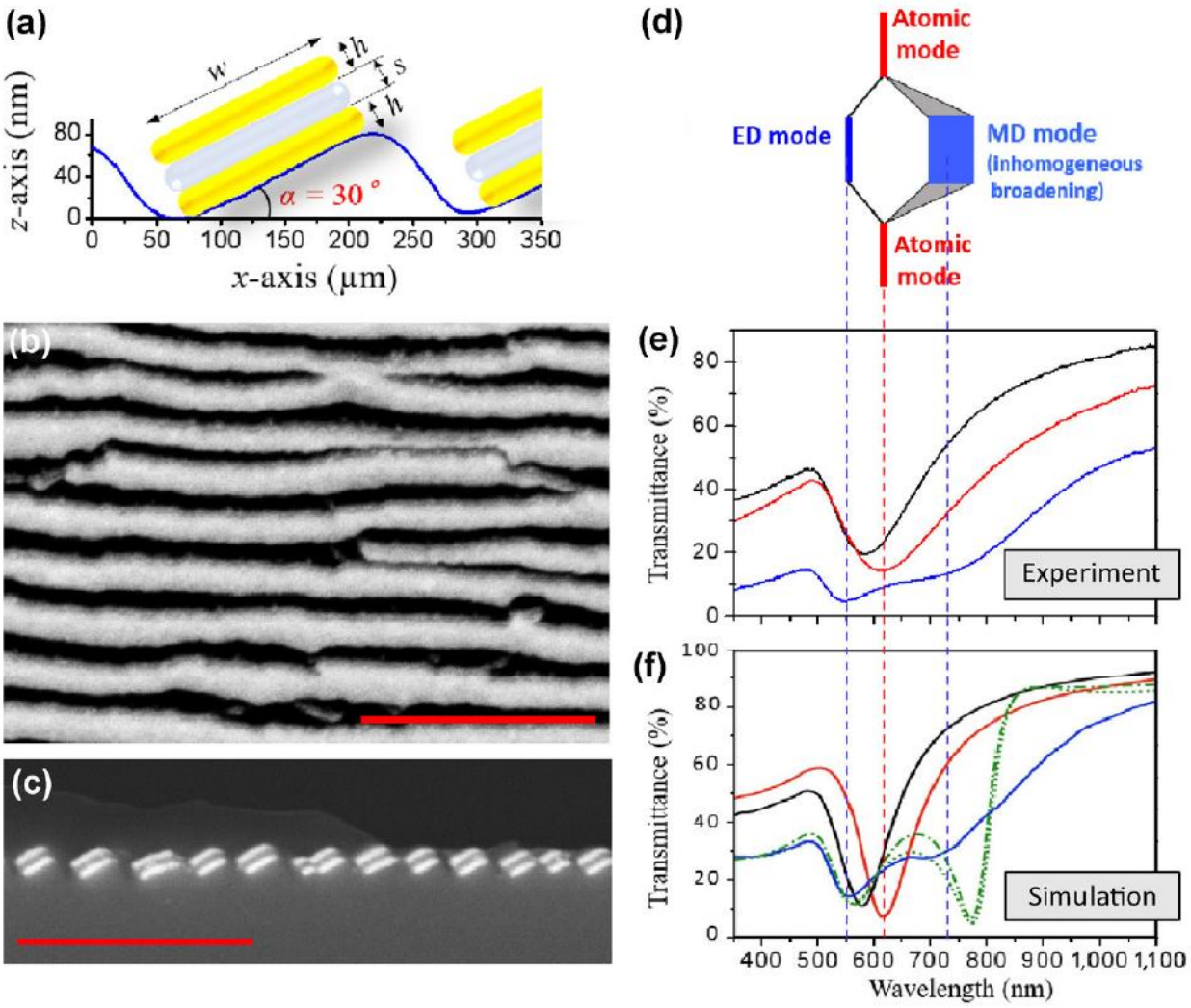

Figure 6: *(a) Illustration of the Au-silica-Au dimers confined on the faceted ripple pattern; w = 100 nm, h = 30 nm, and s = 42 nm. (b) Top-view and (c) cross-section SEM images of the Au-silica-Au dimers, respectively; the red scale bars correspond to 1 μm. (d) Illustration of the hybridization mechanism for the dimer configuration; the inhomogeneous broadening effects caused by a disorder of the array, which mainly affects the low energy supermode, are also considered. (e) Measured and (f) calculated (Comsol Multiphysics) optical spectra (transversal polarization) of Au NWs (black curves), Au-silica NWs (red curves), and Au-silica-Au dimers (blue curves), at normal incidence. Green trace curves in (f) represent the simulations of the Au-silica-Au dimers without considering the disorder of the array, with (green dotted curve) and without (dash-dot curve) the effective environment approximation.*

The cross-section image clearly shows the dielectric silica layer (darker film) sandwiched between

two metallic strips (brighter films) that are vertically disconnected. The coupled nanostrips lie on parallel facets following the asymmetric saw-tooth profile, typical for the ripple pattern. Therefore, we can conclude that the SO process effectively facilitates conformal stacking of the Au-SiO2-Au layers with respect to the underlying ripple pattern, leading to the confinement of 1D arrays of vertically stacked NW dimers.

The optical response of the arrays was monitored during the multi-step fabrication process by measuring the normal-incidence transmittance for both longitudinal and transversal polarizations. For the longitudinal TE-polarization the optical spectra of the Au-silica-Au dimers resemble that of the Au NWs, despite a reduced transmittance with a maximum at about 20%. For the transversal TM-polarization (Fig. 6(e)), a significant modification of the optical response is observed, which can be interpreted using the hybridization mechanism summarized in Fig. 6(d). The LSP resonance characteristic of the monomeric NWs (black curve in Fig. 6(e)) red-shifts from approximately 570 to 620 nm when the metasurface is capped with silica (red curve in Fig. 6(e)). This shift is caused by the increase of the average refractive index of the dielectric medium surrounding the Au NWs, which can be attributed with the deposited sub-stoichiometric oxide SiO2–x on the surface by sputtering, which exhibits a higher refractive index, than that of the SiO2 target (we estimated that $n$cap = 1.75). The TM optical spectrum of the dimeric metasurface (blue curve) shows a splitting of the LSP resonance of the monomeric nanostrip configuration, with the formation of a high energy mode at approximately 550 nm and low energy mode at approximately 730 nm (wavelength). The observed hybridization behavior is confirmed by optical simulations of Prof. Della Valle (Fig. 6(f)), which show split plasmonic modes, spectrally overlapped with the measured data, except for the width of the low energy mode, which is significantly larger than that of an ideal (monodispersed) array of Au-silica-Au nanodimers (green dotted curve). We can identify the high and low energy modes as an electric dipole (ED) and magnetic dipole (MD) modes, respectively, as recently reported in studies on plasmonic meta-atoms [40,55].

It is well known that the MD mode is superior with respect to the ED mode, in terms of sensitivity to small parameters variations [39,55]. Therefore, the MD resonance is more affected by the disorder of the SO pattern induced by the size distribution of the NWs (Fig. 4(b)), which is conformally replicated in the dimer configuration. In order to provide a quantitative estimation of the disorder effects on the broadening of the MD plasmonic resonance Prof. Della Valle performed stochastic

simulations of the TM optical response, based on the measured distribution of the NWs' width *w*. The transmittance of the disordered array is shown in Fig. 6(f) (blue curve), which is in a good agreement with the measured spectrum in Fig. 6(e) (blue curve). We can conclude that the MD resonance is broadened by an inhomogeneous mechanism owing to the size distribution, an intrinsic feature of the SO patterning.

Magnetic mode tunability and near field enhancement

Analogously to the monomeric metasurface, by changing the morphological parameters of the Au-silica-Au meta-atom, we can tailor the optical response of the dimeric configuration. In particular, we verified both experimentally and theoretically that by adjusting the thickness *h* (Au) and thickness *s* (silica) in the range of 20–40 nm, one can effectively control the hybridization mechanism to tune the plasmonic resonances in a broad range of wavelengths. Figure 7(a) and 7(b) show the measured and calculated TM spectra of dimeric metasurfaces, respectively, with different values of the (*h*, *s*) parameters: (30, 42) nm (blue curves), (20, 42) nm (green curves), and (20, 21) nm (red curves). A large red-shift of the MD mode from 740 to 850 nm is observed when the thickness *h* decreases from 30 to 20 nm, while maintaining a constant thickness of the silica spacer (*s* = 42 nm). The high-energy ED resonance is also red shifted, though only by 20 nm. We can conclude that the optical tailoring of hybrid plasmonic modes in nanostrip dimers is reminiscent of the retardation-based mechanism, which occurs at the single nanostrip level [39,47]. In addition, the high sensitivity of the MD resonance to the morphological parameters leads to an enhanced spectral shift. The MD resonance can be tuned even more efficiently by adjusting the thickness of the silica spacer layer, while maintaining a constant thickness *h*.

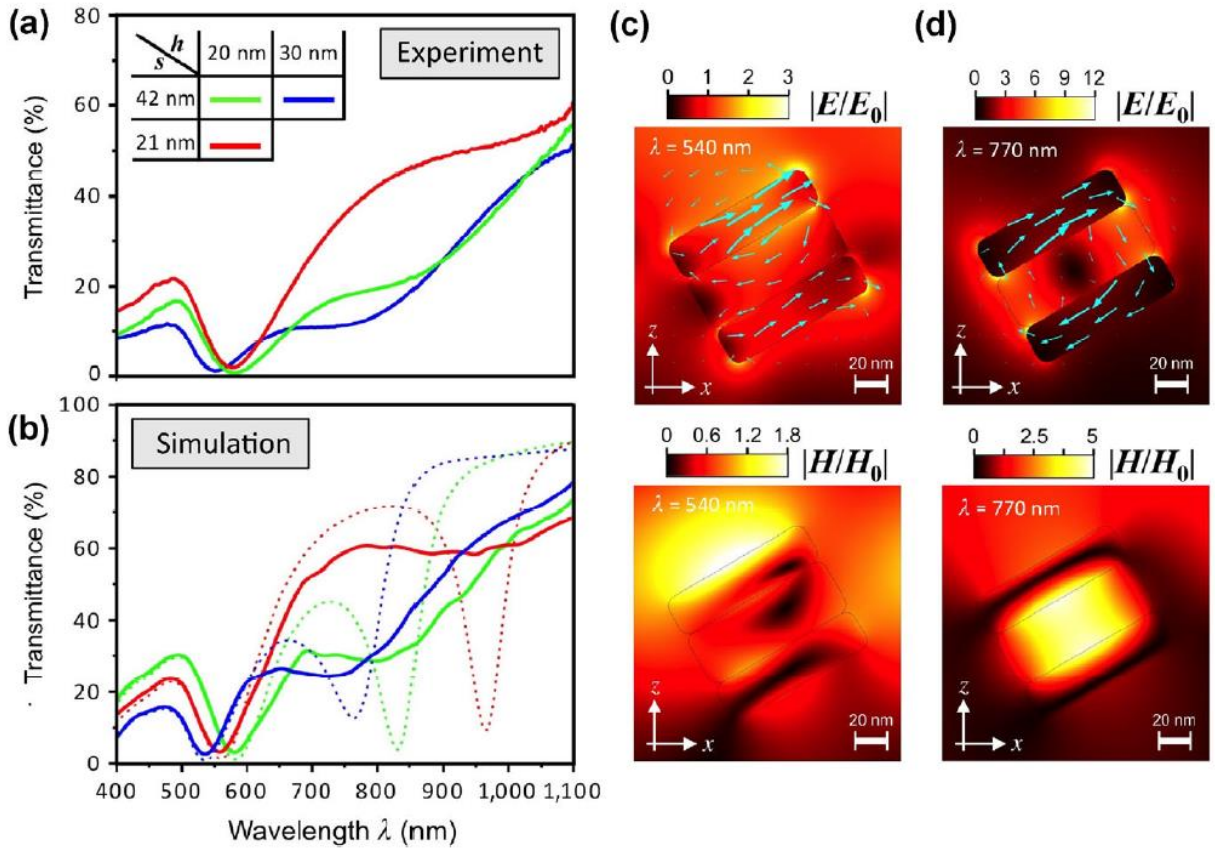

Figure 7: *(a) Measured and (b) calculated transmission spectra of the Au-silica-Au dimers, for transversal polarization with respect to the dimers' long axis at an angle of incidence of 35°. The blue, green, and red curves correspond to (h, s) of (30, 42), (20, 42), and (20, 21) nm, respectively. The dashed curves in (b) represent the simulations without considering the intrinsic disorder of the pattern (see Experimental section for details). Simulations of the plasmonic electric (top panels) and magnetic (bottom panels) near-field enhancements of the Au-silica-Au dimers with (h, s) = (30, 42) nm, excited at (c) 540 nm and (d) 770 nm. The arrows represent the displacement current density at a representative moment of time. A typical ED configuration is observed at 540 nm in (c), where the displacement currents have the same orientation in both nanostrips (from bottom left to top right), whereas a typical MD configuration appears at 770 nm in (d), with antiparallel currents in the two nanostrips, which leads to a current loop in the meta-atom and magnetic field concentration in-between the nanostrips.*

As an example, Fig. 7(a) shows a shift of the MD resonance by approximately 200 nm with the decrease of the silica spacer layer thickness from s = 42 nm (green curve) to s = 21 nm (red curve).

This large shift is in agreement with the one retrieved by the numerical simulations in Fig. 7(b), and can be explained using the hybridization theory. The thickness of the silica spacer layer (*s*) controls the proximity of the individual nanostrips, and thus the strength of the coupling *C* between their induced electric fields, which in turns determines the amount of splitting between the corresponding plasmonic resonances [56]. The coupling C, and consequently the splitting, increases with the decrease of *s*. In particular, the MD resonance is significantly more red-shifted, compared with the blue-shift of the ED mode, as typical for gold nanodimers in the VIS and NIR ranges [56].

Regarding applications in optical spectroscopies and biosensing, the tunable plasmonic near-field enhancement induced by the excitation of the MD in the NIR range is particularly intriguing, as less energetic pump lasers mean lower sample damage and reduced fluorescence background signal, which can interfere with Raman fingerprint recognition. Prof. Della Valle calculated near-field distribution for dimers with typical sizes of (*h*, *s*) = (30, 42) nm shown in Figs. 7(c) and 7(d) (thermal color map), for excitations of the ED resonance at 540 nm and MD resonance at 770 nm, respectively. It is worth noting that a strong near-field enhancement occurs at the edge of the dimers in the range of few nanometers, where $|E/E_0|$ is approximately 3 for the ED mode and approximately 12 for the MD mode; E and E_0 are the total and incident electric fields, respectively. These values are very promising, compared with those of single Au NWs arrays, which exhibit a field enhancement of approximately 4 at the LSP wavelength of 565 nm, especially considering that e.g. SERS gain is proportional to the fourth power of the local electric field. Moreover, the inhomogeneous broadening of the MD resonance leads to a multiplexed configuration of the MD hot spots of the metasurface, with different sites resonating at different wavelengths within a broad spectrum. This allows one to mitigate the design challenges in terms of matching of a given operation wavelength (e.g. pump laser wavelength in an SERS setup). Simultaneously, the resonance broadening leads to a dilution of the active hot spots, compared with the density of the meta-atoms, according to the ratio between the homogeneous broadening of the MD resonance (approximately 60–70 nm) and inhomogeneous broadening (order of 300 nm). However, the highly anisotropic configuration of the nanostrip dimers, with a characteristic length in the range of several micrometers (Fig. 4(a)), can still provide a relatively high hot-spots filling factor; compared with the localized hot spots provided by more conventional isotropic plasmonic patterns of 2D nanostructures (e.g., conventional film on nanospheres, or arrays of rod nanoantennas).

3.2 Conclusions

During my PhD I worked on a multi-step self-organization method based on defocused IBS and kinetically controlled deposition, allowing the fabrication of engineered plasmonic patterns on a large area. In particular, highly anisotropic plasmonic metasurfaces based on gold nanostrips in monomeric as well as dimeric configurations of the meta-atoms were fabricated. The SO fabrication method can control and tailor plasmonic resonances of NWs, in particular, the hybridization mechanism in molecular meta-atoms composed of two coupled gold nanostrips. With this approach it's possible to engineer a magnetic dipole resonance with broadband tuning and subradiant features, by employing plasmon hybridization methods. The high sensitivity of the plasmonic resonances to small variations of dimers morphology required a challenging precise control of the configuration parameters during the SO fabrication. To the best of our knowledge, this is the first demonstration of such capability obtained by a large-area SO/SA fabrication technique. Taking into account the potentials of the subradiant high-field-enhancement, plasmonic resonances for nonlinear nanospectroscopies, including SERS and SECARS, and plasmon-enhanced photon harvesting in solar and photovoltaic cells, these findings pave the way for a further development of the field.

3.3 Experimental

Samples fabrication

A self-organized ripple pattern is induced at the surface of a soda-lime glass substrate by IBS. A defocused Ar+-ion beam with an energy of E = 800 eV is directed to the glass surface using an extraction grid polarized at V = –200 V, while a tungsten filament achieves charge neutralization through thermionic emission. The ion fluence is approximately 1.4 × 1019 ions/cm^2. The obtained templates were employed to confine metal NW arrays by a thermal Au evaporation perpendicular to the ripples' long axis. The thickness of the Au NWs was controlled by means of a calibrated quartz microbalance. A thin silica film is then conformally grown by sputtering deposition using a SiO2 target on the Au NWs, previously confined on the "wide" ridges tilted at α = +30°. In analogy with the previous evaporation step, and in order to ensure conformality, the silica film was deposited at an incidence angle of θ = 50°. In the final step, the dimer is completed by another

identical thermal evaporation of Au. The thickness of the Au and silica layers is controlled by means of a calibrated quartz microbalance.

Optical characterization

The optical response of the Au NWs and Au-silica-Au dimer arrays was investigated in the NUV–VIS–NIR spectrum by measuring optical transmission at normal incidence. The radiation emitted by a compensated deuterium-halogen lamp (DH-2000-BAL, Mikropak) is fiber-coupled to a linear polarizer and pinhole (with a diameter of 5 mm) acting also as a sample holder, placed at the focus of the optical beam. The polarization of the incoming light, incident on the back side of the sample, can be selected as parallel (TE-pol) or perpendicular (TM-pol) with respect to the Au NWs' long axis. A lens positioned at the opposite side of the sample, aligned with the illumination beam, focuses the radiation transmitted through the sample into a second optical fiber. Then, the signal is detected by a high-resolution solid-state spectrometer (HR4000 Ocean Optics) connected to a computer for the acquisition of the spectra. All spectra presented in this manuscript were normalized to the optical transmittance of a bare glass substrate.

Morphological characterization

The surface topography of the samples was investigated using both AFM and SEM techniques. The AFM topographies were acquired using the intermittentcontact mode with two different instruments (Nanosurf Mobile S and NanoMagnetic Ez-AFM) equipped with a high-aspect-ratio Si tip (ACL and ACSTA by APPNano; curvature radius: 10–20 nm). A thermionic emission SEM microscope (SU3500, Hitachi) operating under a high-vacuum condition was employed to acquire images, with an energy of the electron beam in the range of 5–10 kV.

References

(1) Dmitriev, A.; Pakizeh, T.; Käll, M.; Sutherland, D. S. Gold–Silica–Gold Nanosandwiches: Tunable Bimodal Plasmonic Resonators. *Small* **2007**, *3* (2), 294–299. https://doi.org/10.1002/smll.200600409.

(2) Kildishev, A. V.; Boltasseva, A.; Shalaev, V. M. Planar Photonics with Metasurfaces. *Science* **2013**, *339* (6125), 1232009–1232009. https://doi.org/10.1126/science.1232009.

(3) Yu, N.; Capasso, F. Flat Optics with Designer Metasurfaces. *Nature Materials* **2014**, *13*

(2), 139–150. https://doi.org/10.1038/nmat3839.

(4) Khorasaninejad, M.; Chen, W. T.; Devlin, R. C.; Oh, J.; Zhu, A. Y.; Capasso, F. Metalenses at Visible Wavelengths: Diffraction-Limited Focusing and Subwavelength Resolution Imaging. *Science* **2016**, *352* (6290), 1190–1194. https://doi.org/10.1126/science.aaf6644.

(5) Zhang, Y.; Zhen, Y.-R.; Neumann, O.; Day, J. K.; Nordlander, P.; Halas, N. J. Coherent Anti-Stokes Raman Scattering with Single-Molecule Sensitivity Using a Plasmonic Fano Resonance. *Nature Communications* **2014**, *5* (1). https://doi.org/10.1038/ncomms5424.

(6) Pors, A.; Nielsen, M. G.; Bozhevolnyi, S. I. Analog Computing Using Reflective Plasmonic Metasurfaces. *Nano Letters* **2015**, *15* (1), 791–797. https://doi.org/10.1021/nl5047297.

(7) Vieu, C.; Carcenac, F.; Pépin, A.; Chen, Y.; Mejias, M.; Lebib, A.; Manin-Ferlazzo, L.; Couraud, L.; Launois, H. Electron Beam Lithography: Resolution Limits and Applications. *Applied Surface Science* **2000**, *164* (1–4), 111–117. https://doi.org/10.1016/S0169-4332(00)00352-4.

(8) Koh, A. L.; Fernández-Domínguez, A. I.; McComb, D. W.; Maier, S. A.; Yang, J. K. W. High-Resolution Mapping of Electron-Beam-Excited Plasmon Modes in Lithographically Defined Gold Nanostructures. *Nano Letters* **2011**, *11* (3), 1323–1330. https://doi.org/10.1021/nl104410t.

(9) Near, R.; Tabor, C.; Duan, J.; Pachter, R.; El-Sayed, M. Pronounced Effects of Anisotropy on Plasmonic Properties of Nanorings Fabricated by Electron Beam Lithography. *Nano Letters* **2012**, *12* (4), 2158–2164. https://doi.org/10.1021/nl300622p.

(10) Aćimović, S. S.; Kreuzer, M. P.; González, M. U.; Quidant, R. Plasmon Near-Field Coupling in Metal Dimers as a Step toward Single-Molecule Sensing. *ACS Nano* **2009**, *3* (5), 1231–1237. https://doi.org/10.1021/nn900102j.

(11) Verslegers, L.; Catrysse, P. B.; Yu, Z.; White, J. S.; Barnard, E. S.; Brongersma, M. L.; Fan, S. Planar Lenses Based on Nanoscale Slit Arrays in a Metallic Film. *Nano Letters* **2009**, *9* (1), 235–238. https://doi.org/10.1021/nl802830y.

(12) Novotny, L.; van Hulst, N. Antennas for Light. *Nature Photonics* **2011**, *5* (2), 83–90. https://doi.org/10.1038/nphoton.2010.237.

(13) Han, G.; Weber, D.; Neubrech, F.; Yamada, I.; Mitome, M.; Bando, Y.; Pucci, A.; Nagao, T. Infrared Spectroscopic and Electron Microscopic Characterization of Gold Nanogap Structure Fabricated by Focused Ion Beam. *Nanotechnology* **2011**, *22* (27), 275202. https://doi.org/10.1088/0957-4484/22/27/275202.

(14) Atwater, H. A.; Polman, A. Plasmonics for Improved Photovoltaic Devices. *Nature Materials* **2010**, *9* (3), 205–213. https://doi.org/10.1038/nmat2629.

(15) Ng, C.; Cadusch, J. J.; Dligatch, S.; Roberts, A.; Davis, T. J.; Mulvaney, P.; Gómez, D. E. Hot Carrier Extraction with Plasmonic Broadband Absorbers. *ACS Nano* **2016**, *10* (4), 4704–4711. https://doi.org/10.1021/acsnano.6b01108.

(16) Kasera, S.; Herrmann, L. O.; Barrio, J. del; Baumberg, J. J.; Scherman, O. A. Quantitative Multiplexing with Nano-Self-Assemblies in SERS. *Scientific Reports* **2015**, *4* (1). https://doi.org/10.1038/srep06785.

(17) Gwo, S.; Wang, C.-Y.; Chen, H.-Y.; Lin, M.-H.; Sun, L.; Li, X.; Chen, W.-L.; Chang, Y.-M.; Ahn, H. Plasmonic Metasurfaces for Nonlinear Optics and Quantitative SERS. *ACS Photonics* **2016**, *3* (8), 1371–1384. https://doi.org/10.1021/acsphotonics.6b00104.

(18) Zhao, X.-M.; Xia, Y.; Whitesides, G. M. Soft Lithographic Methods for Nano-Fabrication. *Journal of Materials Chemistry* **1997**, *7* (7), 1069–1074. https://doi.org/10.1039/a700145b.

(19) Xia, Y.; Whitesides, G. M. Soft Lithography. *Angewandte Chemie International Edition* **1998**, *37* (5), 550–575. https://doi.org/10.1002/(SICI)1521-3773(19980316)37:5<550::AID-ANIE550>3.0.CO;2-G.

(20) Guo, L. J. Nanoimprint Lithography: Methods and Material Requirements. *Advanced Materials* **2007**, *19* (4), 495–513. https://doi.org/10.1002/adma.200600882.

(21) Boltasseva, A. Plasmonic Components Fabrication via Nanoimprint. *Journal of Optics A: Pure and Applied Optics* **2009**, *11* (11), 114001. https://doi.org/10.1088/1464-4258/11/11/114001.

(22) Xiang, C.; Kung, S.-C.; Taggart, D. K.; Yang, F.; Thompson, M. A.; Güell, A. G.; Yang, Y.; Penner, R. M. Lithographically Patterned Nanowire Electrodeposition: A Method for Patterning Electrically Continuous Metal Nanowires on Dielectrics. *ACS Nano* **2008**, *2* (9), 1939–1949. https://doi.org/10.1021/nn800394k.

(23) Verre, R.; Fleischer, K.; Ualibek, O.; Shvets, I. V. Self-Assembled Broadband Plasmonic Nanoparticle Arrays for Sensing Applications. *Applied Physics Letters* **2012**, *100* (3), 031102. https://doi.org/10.1063/1.3674982.

(24) Thomas, K. G.; Barazzouk, S.; Ipe, B. I.; Joseph, S. T. S.; Kamat, P. V. Uniaxial Plasmon Coupling through Longitudinal Self-Assembly of Gold Nanorods. *The Journal of Physical Chemistry B* **2004**, *108* (35), 13066–13068. https://doi.org/10.1021/jp049167v.

(25) González-Díaz, J. B.; García-Martín, A.; García-Martín, J. M.; Cebollada, A.; Armelles, G.; Sepúlveda, B.; Alaverdyan, Y.; Käll, M. Plasmonic Au/Co/Au Nanosandwiches with Enhanced Magneto-Optical Activity. *Small* **2008**, *4* (2), 202–205. https://doi.org/10.1002/smll.200700594.

(26) Hung, A. M.; Micheel, C. M.; Bozano, L. D.; Osterbur, L. W.; Wallraff, G. M.; Cha, J. N. Large-Area Spatially Ordered Arrays of Gold Nanoparticles Directed by Lithographically Confined DNA Origami. *Nature Nanotechnology* **2010**, *5* (2), 121–126.

https://doi.org/10.1038/nnano.2009.450.

(27) Im, H.; Bantz, K. C.; Lee, S. H.; Johnson, T. W.; Haynes, C. L.; Oh, S.-H. Self-Assembled Plasmonic Nanoring Cavity Arrays for SERS and LSPR Biosensing. *Advanced Materials* **2013**, *25* (19), 2678–2685. https://doi.org/10.1002/adma.201204283.

(28) Wang, P.-Y.; Shields, C. W.; Zhao, T.; Jami, H.; López, G. P.; Kingshott, P. Rapid Self-Assembly of Shaped Microtiles into Large, Close-Packed Crystalline Monolayers on Solid Surfaces. *Small* **2016**, *12* (10), 1309–1314. https://doi.org/10.1002/smll.201503130.

(29) Robbiano, V.; Giordano, M.; Martella, C.; Stasio, F. D.; Chiappe, D.; de Mongeot, F. B.; Comoretto, D. Hybrid Plasmonic-Photonic Nanostructures: Gold Nanocrescents Over Opals. *Advanced Optical Materials* **2013**, *1* (5), 389–396. https://doi.org/10.1002/adom.201200060.

(30) Toma, A.; Chiappe, D.; Massabò, D.; Boragno, C.; Buatier de Mongeot, F. Self-Organized Metal Nanowire Arrays with Tunable Optical Anisotropy. *Applied Physics Letters* **2008**, *93* (16), 163104. https://doi.org/10.1063/1.3002319.

(31) Choi, D.; Choi, Y.; Hong, S.; Kang, T.; Lee, L. P. Self-Organized Hexagonal-Nanopore SERS Array. *Small* **2010**, *6* (16), 1741–1744. https://doi.org/10.1002/smll.200901937.

(32) Mishra, Y. K.; Adelung, R.; Kumar, G.; Elbahri, M.; Mohapatra, S.; Singhal, R.; Tripathi, A.; Avasthi, D. K. Formation of Self-Organized Silver Nanocup-Type Structures and Their Plasmonic Absorption. *Plasmonics* **2013**, *8* (2), 811–815. https://doi.org/10.1007/s11468-013-9477-2.

(33) Fan, J. A.; Wu, C.; Bao, K.; Bao, J.; Bardhan, R.; Halas, N. J.; Manoharan, V. N.; Nordlander, P.; Shvets, G.; Capasso, F. Self-Assembled Plasmonic Nanoparticle Clusters. *Science* **2010**, *328* (5982), 1135–1138. https://doi.org/10.1126/science.1187949.

(34) Fan, J. A.; Bao, K.; Sun, L.; Bao, J.; Manoharan, V. N.; Nordlander, P.; Capasso, F. Plasmonic Mode Engineering with Templated Self-Assembled Nanoclusters. *Nano Letters* **2012**, *12* (10), 5318–5324. https://doi.org/10.1021/nl302650t.

(35) Natelson, D. Best of Both Worlds. *Nature Materials* **2006**, *5* (11), 853–854. https://doi.org/10.1038/nmat1769.

(36) Giordano, M. C.; Longhi, S.; Barelli, M.; Mazzanti, A.; Buatier de Mongeot, F.; Della Valle, G. Plasmon Hybridization Engineering in Self-Organized Anisotropic Metasurfaces. *Nano Research* **2018**, *11* (7), 3943–3956. https://doi.org/10.1007/s12274-018-1974-3.

(37) Miyazaki, H. T.; Kurokawa, Y. Squeezing Visible Light Waves into a 3-Nm-Thick and 55-Nm-Long Plasmon Cavity. *Physical Review Letters* **2006**, *96* (9). https://doi.org/10.1103/PhysRevLett.96.097401.

(38) Yuan, H.-K.; Chettiar, U. K.; Cai, W.; Kildishev, A. V.; Boltasseva, A.; Drachev, V. P.; Shalaev, V. M. A Negative Permeability Material at Red Light. *Optics Express* **2007**, *15* (3), 1076. https://doi.org/10.1364/OE.15.001076.

(39) Søndergaard, T.; Jung, J.; Bozhevolnyi, S. I.; Della Valle, G. Theoretical Analysis of Gold Nano-Strip Gap Plasmon Resonators. *New Journal of Physics* **2008**, *10* (10), 105008. https://doi.org/10.1088/1367-2630/10/10/105008.

(40) Pors, A.; Bozhevolnyi, S. I. Plasmonic Metasurfaces for Efficient Phase Control in Reflection. *Optics Express* **2013**, *21* (22), 27438. https://doi.org/10.1364/OE.21.027438.

(41) Miyata, M.; Holsteen, A.; Nagasaki, Y.; Brongersma, M. L.; Takahara, J. Gap Plasmon Resonance in a Suspended Plasmonic Nanowire Coupled to a Metallic Substrate. *Nano Letters* **2015**, *15* (8), 5609–5616. https://doi.org/10.1021/acs.nanolett.5b02307.

(42) Raza, S.; Stenger, N.; Pors, A.; Holmgaard, T.; Kadkhodazadeh, S.; Wagner, J. B.; Pedersen, K.; Wubs, M.; Bozhevolnyi, S. I.; Mortensen, N. A. Extremely Confined Gap Surface-Plasmon Modes Excited by Electrons. *Nature Communications* **2014**, *5* (1). https://doi.org/10.1038/ncomms5125.

(43) Giordano, M. C.; de Mongeot, F. B. Anisotropic Nanoscale Wrinkling in Solid-State Substrates. *Advanced Materials* **2018**, *30* (30), 1801840. https://doi.org/10.1002/adma.201801840.

(44) D'Andrea, C.; Fazio, B.; Gucciardi, P. G.; Giordano, M. C.; Martella, C.; Chiappe, D.; Toma, A.; Buatier de Mongeot, F.; Tantussi, F.; Vasanthakumar, P.; et al. SERS Enhancement and Field Confinement in Nanosensors Based on Self-Organized Gold Nanowires Produced by Ion-Beam Sputtering. *The Journal of Physical Chemistry C* **2014**, *118* (16), 8571–8580. https://doi.org/10.1021/jp5007236.

(45) Guerrisi, M.; Rosei, R.; Winsemius, P. Splitting of the Interband Absorption Edge in Au. *Physical Review B* **1975**, *12* (2), 557–563. https://doi.org/10.1103/PhysRevB.12.557.

(46) Liao, Y.-L.; Zhao, Y. Design of Wire-Grid Polarizer with Effective Medium Theory. *Optical and Quantum Electronics* **2014**, *46* (5), 641–647. https://doi.org/10.1007/s11082-013-9768-z.

(47) Della Valle, G.; Sondergaard, T.; Bozhevolnyi, S. I. Plasmon-Polariton Nano-Strip Resonators: From Visible to Infra-Red. *Optics Express* **2008**, *16* (10), 6867. https://doi.org/10.1364/OE.16.006867.

(48) Prodan, E. A Hybridization Model for the Plasmon Response of Complex Nanostructures. *Science* **2003**, *302* (5644), 419–422. https://doi.org/10.1126/science.1089171.

(49) Wang, H.; Brandl, D. W.; Nordlander, P.; Halas, N. J. Plasmonic Nanostructures: Artificial Molecules. *Accounts of Chemical Research* **2007**, *40* (1), 53–62.

https://doi.org/10.1021/ar0401045.

(50) Cao, Y. C. Nanoparticles with Raman Spectroscopic Fingerprints for DNA and RNA Detection. *Science* **2002**, *297* (5586), 1536–1540. https://doi.org/10.1126/science.297.5586.1536.

(51) Kneipp, K.; Moskovits, M.; Kneipp, H. *Surface-Enhanced Raman Scattering Physics and Applications*; 2006.

(52) Fazio, B.; D'Andrea, C.; Bonaccorso, F.; Irrera, A.; Calogero, G.; Vasi, C.; Gucciardi, P. G.; Allegrini, M.; Toma, A.; Chiappe, D.; et al. Re-Radiation Enhancement in Polarized Surface-Enhanced Resonant Raman Scattering of Randomly Oriented Molecules on Self-Organized Gold Nanowires. *ACS Nano* **2011**, *5* (7), 5945–5956. https://doi.org/10.1021/nn201730k.

(53) Xie, J.; Zhang, Q.; Lee, J. Y.; Wang, D. I. C. The Synthesis of SERS-Active Gold Nanoflower Tags for *In Vivo* Applications. *ACS Nano* **2008**, *2* (12), 2473–2480. https://doi.org/10.1021/nn800442q.

(54) Menke, E. J.; Thompson, M. A.; Xiang, C.; Yang, L. C.; Penner, R. M. Lithographically Patterned Nanowire Electrodeposition. *Nature Materials* **2006**, *5* (11), 914–919. https://doi.org/10.1038/nmat1759.

(55) Davis, T. J.; Vernon, K. C.; Gómez, D. E. Designing Plasmonic Systems Using Optical Coupling between Nanoparticles. *Physical Review B* **2009**, *79* (15). https://doi.org/10.1103/PhysRevB.79.155423.

(56) Davis, T. J.; Gómez, D. E.; Vernon, K. C. Simple Model for the Hybridization of Surface Plasmon Resonances in Metallic Nanoparticles. *Nano Letters* **2010**, *10* (7), 2618–2625. https://doi.org/10.1021/nl101335z.

CHAPTER 4

Large Area Color Routing via Cross-Polarized Detuned Plasmonic Nanoantennas

Introduction

The investigation of optical phenomena at the nanoscale has witnessed an amazing development in the last decades, with particular interest to metallic nanostructures, supporting so-called plasmonic resonances and subsequent spatial localization of intense optical fields far below the diffraction limit [1–3]. A key feature of subwavelength metallic structures is their capability to provide amplified light scattering and strong near field confinement at the resonant frequency, thus behaving as optical nanoantennas [4–9]. Plasmonic nanoantennas have been thoroughly developed (also employing high refractive index dielectrics [10]) to demonstrate challenging functionalities in flat-optics nanodevices [11,12], including waveplates [13,14], polarization splitters [15,16], directional nanoemitters [17–19], unidirectional antennas [20–22], and multi-directional color routers [23–26]. The availability of broadband highly directive optical antennas is crucial for the development of a wide range of applications from optical sensors [2,27,28], to photonic harvesting [11,29,30] and biosensing [31–34]. When dealing with color routing, i.e. wavelength selective multi-directional scattering, different strategies, comprising single or multi-element antenna systems, and different materials, have been so far explored, as summarized below:

(i) The first approach relies on multi-element nanoantennas. The simplest configuration exploits the scattering interference between two asymmetric nanoantenna elements whose resonant oscillating dipoles are transversely aligned with respect to the incident beam, and separated by a fixed distance [23,24,35]. Unidirectional scattering (i.e. fully constructive interference on one side of the multi-element antenna and fully destructive on the other) is enabled by a large phase shift of the two oscillators with respect to the (driving) illuminating field, in the spectral range in-between their resonances. The wavelength selectivity, enabling color routing operation, is obtained via a symmetry breaking induced, e.g., by using two different materials for the two nano-antenna elements [23]. The unidirectionality can be also enhanced with several elements in order to realize

a downscaling of the classic RF Yagi-Uda antenna [20,36,37] or other array configurations [36,38,39]. The intrinsic limit to the multi-element antennas design is the strong sensitivity to the inter-distance between the individual elements, which demands for expensive top-down nanofabrication techniques.

ii) Another approach exploits the near field interference of multiple (e.g., electric and magnetic) resonances simultaneously excited in the same antenna element. The color routing is achieved provided that one of the resonances undergoes an abrupt π phase shift with respect to the others, when scanning the spectral range of operation. This is typically accomplished with a magnetic dipolar resonance in all-dielectric nanostructures, allowing an abrupt change of the rotation direction of the in-plane eddy currents generating the magnetic field at optical frequencies [25,40–42]. Relatively intense magnetic modes can indeed be excited in metallic nanostructures and interfere with the electric modes to form a unidirectional light scattering pattern. This can be achieved by resorting to specific antenna geometries, e.g. gold split-ring resonators [43] or even nanodisk antennas [44], but does not induce any abrupt phase shift of the optical magnetic mode. Therefore, while plasmonic nanoantennas can be engineered to achieve unidirectionality [45,46], only dielectric and hybrid metal/dielectric antennas are suited for color routing [25,47]. This single-element multiple-resonance approach deserves a quite complex engineering of the antenna shape and material composition, which, again, requires demanding top-down fabrication methods.

iii) The third approach is based upon subwavelength wavefront manipulation by metasurfaces, with meta-atoms made of either single or multi-element nanoantennas. As for ordinary diffraction gratings, optical metasurfaces can be tailored to enforce reflection/transmission of selected diffraction orders. Also, by introducing spatial inhomogeneities along the plane, phase gradients can be implemented in order to provide either wavelength independent unidirectional scattering [48], or wavelength selective narrow-band bi-directional color routing operation [26,49]. Very recently, active metasurfaces for bias controlled directional scattering started to gain attention [50].

All the proposed strategies to achieve color routing (especially the last one) rely on complex design of the nanoantenna geometry, inter-antenna gap and chemical composition. This usually requires a heavy computational effort and time-consuming lithographic nanofabrication processes, which are inherently limited to small areas.

During my PhD I worked on a novel approach to bi-directional passive color routing at optical frequencies, based on cross-polarized detuned plasmonic nano-antennas in a uniaxial (quasi-1D) bimetallic configuration [51]. The directional routing mechanism is based purely on the relative tilt and material composition of the nanoantenna elements, rather than on the interference of their resonant optical modes, which is actually inhibited by the cross-polarization configuration. In this way it's possible to achieve broadband and highly effective color routing functionalities over large area (cm^2) with much more relaxed fabrication constraints and requirements compared to the state of the art antenna design. This strategy can be effectively implemented by using the self-organized nanofabrication approach based on the hot Ion Beam Sputtering of soda-lime glasses described in section 1.3.2 of this thesis, and on the maskless confinement of plasmonic bi-directional antennas on these anisotropic wrinkled transparent templates.

4.1 – Results and discussion

Cross-Polarized Detuned Plasmonic Nanoantennas theoretical model and numerical simulations

The concept behind the previously described approach is summarized in Fig. 1, where simulations by Prof. Della Valle (Politecnico di Milano) are presented. Let's consider the two-dimensional scattering problem of two cross-polarized electric dipolar scatterers, excited by a uniform plane wave with in-plane electric field (i.e. linear TM polarization) (Fig. 1a). If the two scatterers exhibit a resonant behavior with well separated scattering peaks (Fig. 1b), e.g., one in the blue (λ_1) and one in the red (λ_2), the blue light is mainly scattered at 90° with respect to the red light, with negligible superposition of the two spectral components in the far field along the two orthogonal directions.

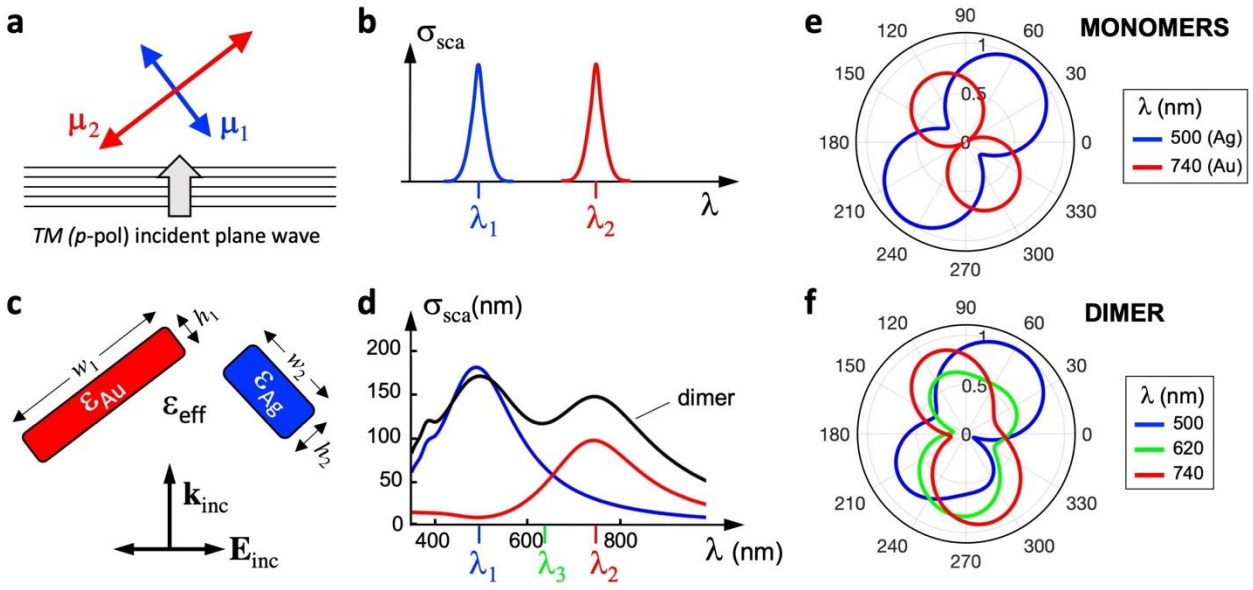

Figure 1: *(a) Sketch of the cross-polarized electrical dipoles for color routing with (b) detuned scattering spectra; (c) implementation with bimetallic nanostrips and (d) the actual scattering spectra of the gold monomer (red), of the silver monomer (blu) and of the dimer (black), retrieved by full-wave numerical simulations; (e) scattering diagram of the nanostrip monomers at their peak resonance wavelengths; (f) same as (e) for the nanostrip dimer, also showing the scattering diagram at an intermediate wavelength (in-between the two resonances).*

Such an ideal system can be implemented with a couple of tilted metallic nanostrips, which are well known to behave as dipolar scatterers, having a pronounced resonance under TM light, enabled by a plasmonic response [52]. The latter can be controlled and tuned by acting on the width (w) and height (h) of the nanostrips, as well as on the metal permittivity. Basically, the fundamental dipolar resonance wavelength of the nanostrip linearly scales with w, and is inversely proportional to h, whereas, for a given geometrical configuration, silver nanostrips resonate at shorter wavelengths compared to gold nanostrips [52]. Having this in mind, two dimensional plasmonic dimer made of a gold nanostrip with (w_1, h_1) = (100,12) nm tilted at 35° with respect to the x-axis and a silver nanostrip with (w_2, h_2) = (*80,35*) nm tilted at -55° (Fig. 1c) were designed. Finite element method (FEM) numerical analysis of the nanostrips scattering spectrum (Fig. 1d) retrieves a peak resonance wavelength at λ_1 = 500 nm for silver and at λ_2 =740 nm for gold isolated nanostrips (or monomers). The scattering diagram as a function of the polar angle Θ for the isolated monomers (Fig. 1e) exhibits the typical pattern of a dipolar scatterer, with two main lobes

orthogonal to the major axis of the nanostrip. In the dimer configuration, the scattering diagram, even though being more complex because of the near-field coupling between the two monomers, preserves the key features of the individual scattering patterns at the two resonance wavelengths (Fig. 1f). In particular, it is worth noting the wavelength dependent bidirectional behavior, characterized by a strong rejection of the blue wing of the spectrum at $\Theta \sim 140°$ and of the red wing at $\Theta \sim 40°$, implementing the desired color routing operation.

Bimetallic nanoantennas fabrication

Even though conceptually simple, the design above detailed poses a fundamental challenge in terms of fabrication, because of the tilted configuration of the nanostrips and the requirement of a large area nanopatterning to allow flat-optics operation. Here, the self-organized nanofabrication based on the anisotropic nanoscale wrinkling in glasses [53], already described in section 1.2.3 of this thesis, enables the effective engineering of tilted plasmonic nanostrip antennas in the form of cross-polarized metallic dimers lying on opposite ridges of a faceted dielectric template.

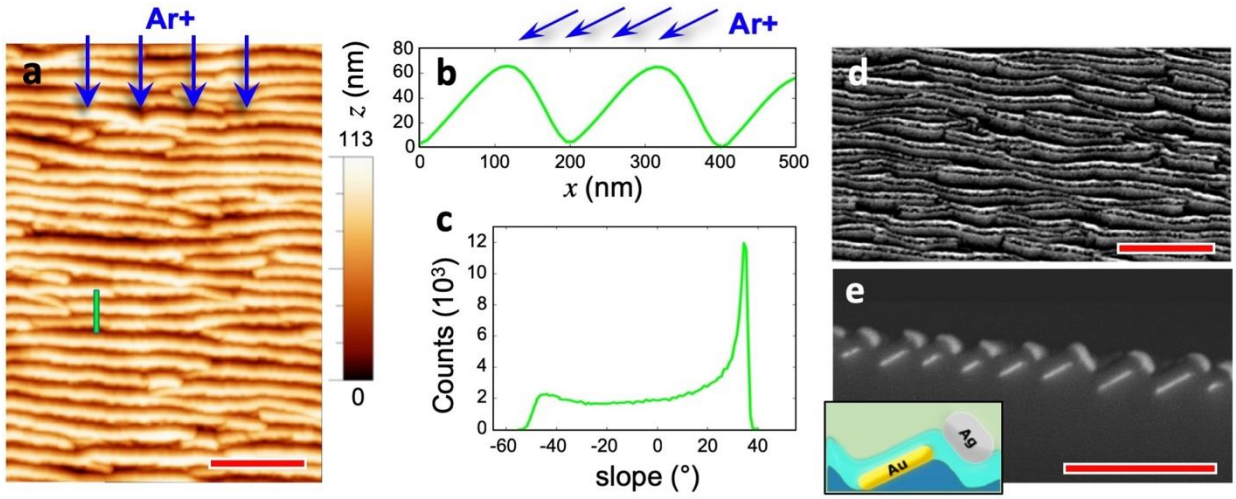

Figure 2: *(a) Atomic Force Microscopy (AFM) topography of the fabricated rippled glass template. Scale bar 1 μm (b) AFM cross section of nanoripples corresponding to green line in panel (a). (c) Histogram of the slope distribution extracted by the AFM image of panel (a). (d) Scanning Electron Microscope (SEM) images of the bimetallic metasurface detected in top view and (e) cross section configuration. Scale bars 1 μm and 600 nm, respectively. The inset represents a sketch of the unit cell cross section of the bimetallic surface.*

A cheap soda-lime glass substrate (20 × 20 × 1 mm) is irradiated with a defocused Ar^+ ion beam set at an incident angle of $\theta = 30°$ and at a low energy of 800 eV. The glass temperature is fixed at about 680 K during the Ion Beam Sputtering (IBS) process. A quasi 1-D rippled pattern is obtained all over the macroscopic sample surface, with a wavevector parallel to the ion beam direction (Fig. 2a). The glass ripples are elongated for a length of several micrometers and show a remarkable degree of long-range order. The nanostructures are characterized by a steep asymmetric saw-tooth profile with a pronounced vertical dynamic of approximately 90 nm (Fig. 2b) and a wavevector periodicity of about 200 nm and assessed by the self-correlation function of the AFM topography. The ridges directly exposed to the ion beam develop a broad facet slope distribution (negative values in the slope frequency plot of Fig. 2c) peaked at about -50°. On the contrary, the ridges opposed to the ion beam (positive values in Fig. 2c) develop wider and very defined facets with slopes peaked at +35°.

Such high aspect-ratio ordered rippled templates, with well-defined tilted facets are the ideal platform for the maskless confinement of plasmonic uniaxial nano-strip antennas (NSA) with controlled tilt and morphology. The controlled growth is achieved by grazing angle physical vapor deposition of metal atoms exploiting shadowing effects on the tilted ripple facets [54]. In order to fabricate the bimetallic dipolar antennas depicted in the theoretical model of Fig. 1c, I first confined Au NSA by glancing evaporation on the wider rippled facets which are tilted at +35° (see inset sketch in Fig. 2e). By the statistical analysis of SEM cross section images (Fig. 2e) the average Au NSA width $w \approx 105$ nm, controlled by the periodicity of the underlying template and by the local slope of the illuminated ripple facets, was assessed. The thickness of the Au NSA reads $h \approx 12$ nm and is determined by the sublimated metal dose and deposition angle (see Experimental section for details). As a second step, an insulating layer of sub-stoichiometric silica was grown on the sample at normal incidence by Radio Frequency Magnetron Sputtering. Finally, Ag NSA were confined on the narrower and steeper rippled facets with an average slope of -50°, on top of the conformally grown silica layer. Ag NSA average w and h are about 83 nm and 36 nm, respectively. The average dielectric gap separating the Au and Ag NSA corresponds to 40 nm, again evaluated from the SEM cross section analysis. The methods enables the controlled growth of subwavelength bimetallic antennas whose length exceeds several micrometers and form a large area quasi 1-D metasurface, as demonstrated by the top- view and cross-section SEM images (Fig.

2d, 2e). The image of the sample cross section (Fig. 2e) evidences the selective lateral confinement of nanoantennas on top of the tilted ripples ridges, thus well mimicking the cross section of the ideal structure sketched in the inset of Fig 2e.

Transmission and scattering measurements

Optical transmittance measurements at normal incidence were performed on the sample using a halogen/deuterium lamp source. Scattering measurements were instead acquired with a custom-made scatterometer set-up, following the scheme sketched in Fig. 3l-3m (see Experimental section for details). The sample was illuminated from the glass side at normal incidence and the scattered light was collected at a fixed polar angle of $\Theta = 50°$, as a function of the azimuthal angle Φ. For both transmittance and scattering measurements, the source light was linearly polarized orthogonally to the NSA long axis (i.e. TM polarization). The same optical measurements were performed also on two other samples: Au NSA, and Ag NSA, fabricated with the same morphological and geometrical configuration as in the complete bimetallic Au-Ag NSA. This allowed to investigate the properties of the final system as well as the optical behavior of its two building blocks. The optical transmittance and the scattering intensities measured for the Au, Ag and Au-Ag NSA samples are shown in Fig. 3d-f and Fig. 3g-i, respectively. Remarkably, for all the three configuration a directional scattering maximum is detected, which is resonant to the localized surface plasmon mode (i.e. minimum in transmittance in Fig. 3d-f).

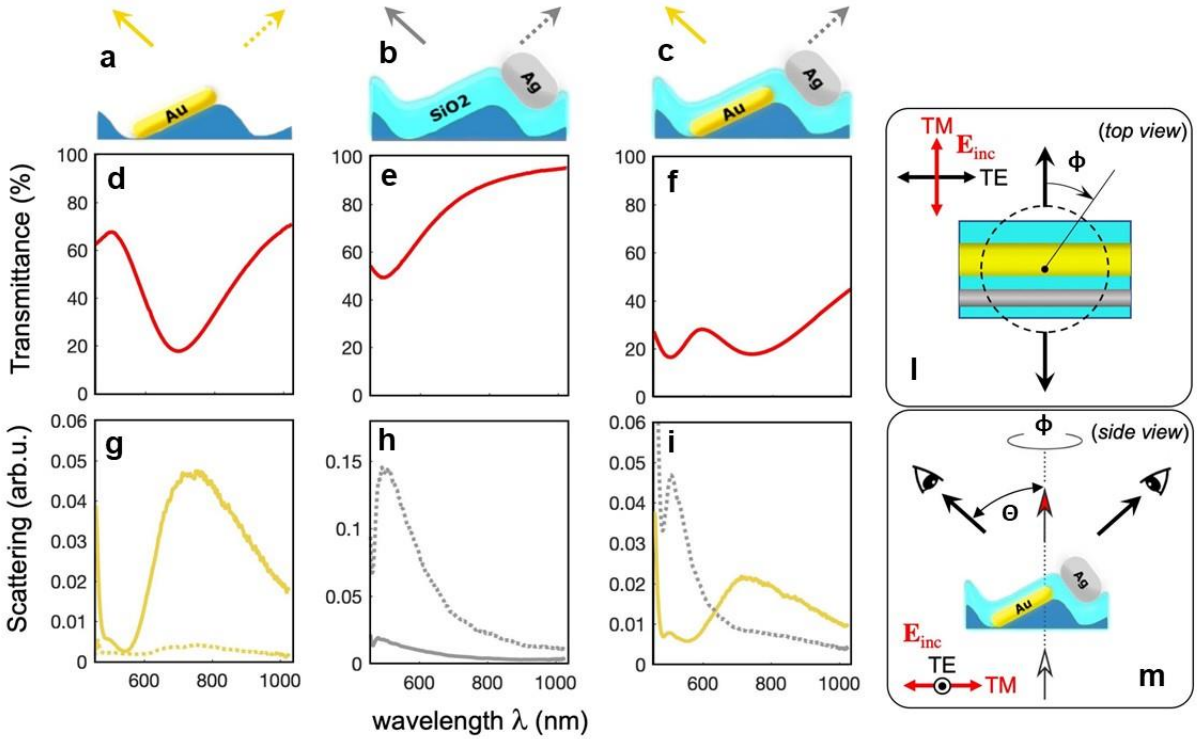

Figure 3: *(a,b,c) Sketch of the Au, Au and Au/Ag NSA meta-atom cross section, respectively. (d,e,f) Measured optical transmittance at normal incidence for Au, Au and Au/Ag NSA arrays, respectively. All the spectra are normalized to the transmittance of the bare glass substrate. (g,h,i) Scattered light intensity detected at Θ = 50°, Φ = 0° (solid curve) and at Θ = 50°, Φ =180° (dashed curve) for Au, Ag and Au/Ag NSA arrays, respectively. The relative scattering scale intensity is the same for all the panels. (l,m) Sketch of the optical set-up exploited for scattering measurements respectively shown in top- and side- view.*

As anticipated above, the scattering pattern of a plasmonic nanostrip antenna is expected to resemble the one of a dipolar antenna. The transmitted scattering maximum is then expected to be centered along the direction normal to the NSA major axis. When Φ = 0°, and Θ = 50°, scattered light collection is essentially facing the +35° tilted Au NSA (as it can be clearly appreciated in the inset of Fig. 3-l-m), i.e. the direction where the scattering intensity is expected to be stronger. Indeed, for this collection configuration (solid yellow curve in bottom panel of Fig. 3-g) the measured scattering intensity shows an intense and broad maximum centered around 750 nm. Note that the scattering maximum and the plasmonic transmittance dip are resonant (the slight frequency shift being ascribable to the well-known mismatch between absorption and scattering resonances

in plasmonic nanostructures), thus clearly demonstrating the plasmonic nature of the enhanced scattered light. When the collection of the scatterometer is set to the azimuthal angle $\Phi = 180°$, the scattered light is measured along the direction of the Au NSA major axis. As a consequence, the scattering intensity drops by about an order of magnitude, in agreement with the radiation pattern simulations of Fig. 1e. Fig. 3e shows the transmittance measurement for the Ag NSA, with the Ag nanostrips confined on a silica layer grown upon the rippled glass template, to preserve the effective refractive index of the medium surrounding the NSA in the complete bimetallic NSA. The plasmonic transmittance dip is blue-shifted to 500 nm compared to the Au NSA, due to the different Ag NSA aspect ratio (*w/h*), and higher permittivity (in modulus) of silver compared to gold [55]. This time, when $\Phi = 180°$ (keeping $\Theta = 50°$) the scattered light collection is perfectly aligned to the normal of the Ag nanostrips, which are tilted at -50°, and an intense scattering peak is recorded at resonance, i.e. around 500 nm, near the edge of our laser source spectrum (dashed grey curve in Fig. 3h). Note that the resonant scattering intensity of the Ag NSA is about 3 times higher than in the Au NSA, mainly because of the better optimized collection angle with respect to the NSA axis and also thanks to the higher optical density of Ag, which implies a larger Ag scattering cross section [52]. When the azimuthal angle is set to $\Phi = 0°$ the scattered light is collected in a direction parallel to the Ag NSA axis, which corresponds to the direction of minimum scattered intensity emission pattern (cf. Fig. 1). As a consequence, the collected scattering intensity considerably drops down (solid gray curve in Fig. 3h). Finally, the transmittance spectrum for the complete bimetallic Ag-Au NSA is shown in Fig. 3c. Two separate transmittance dips are distinguishable at 500 nm and 740 nm, which are associated to the plasmonic resonances of the Ag NSA and Au NSA monomers, respectively. When the azimuthal angle is fixed to $\Phi = 0°$ the collection of the scattering intensity faces the Au NSA and a scattering maximum is recorder at the Au NSA resonance of 740 nm (solid yellow curve in Fig. 3g), with negligible contributions from the Ag NSA (cf. Fig 3h, solid grey curve). When the azimuthal angle is set to $\Phi = 180°$, the collection direction faces the Ag NSA, and a scattering intensity peak is recorded at the Ag NSA resonance of 500 nm, with negligible contribution from the Au NSA (cf. Fig 3g bottom panel, dashed yellow curve). Note also that the scattering from the Au-Ag dimeric NSA is partially attenuated with respect to the case of individual Au or Ag NSA building blocks, mostly because of non-resonant shadowing effects. Actually, even though hybridization is negligible in our detuned cross-polarized configuration (in agreement with the numerical simulations of Fig. 1), each

monomer is placed within the cross-section region of the other, thus causing an effective partial attenuation of the beam. Remarkably, the detected directivity figures highlight the high efficiency of self-organized bimetallic antennas in wavelength selective bidirectional scattering.

This response is well explained in terms of the cross-polarized detuned plasmonic nanoantenna model. Provided the tilted nanoantennas configuration the Ag and Au NSA monomer resonantly scatters light to the "right side" at about 500 nm wavelength, and to the "left side" at about 740 nm wavelegth, respectively.

Scattering directivy of the large area, passive color router

To quantify the color routing performance in our samples, we plot in Fig. 4 the *Directivity spectrum (D)*, defined as follows:

$$D(\lambda;\Theta) = 10 \times \log_{10}\left[\frac{S(\Phi = 0°, \Theta;\lambda)}{S(\Phi = 180°, \Theta;\lambda)}\right]$$

The Directivity spectra at polar angles $\Theta = 30°$ and $\Theta = 50°$ are shown in Fig. 4 (top panels), together with the corresponding numerical simulations by Prof. Della Valle (bottom panels).

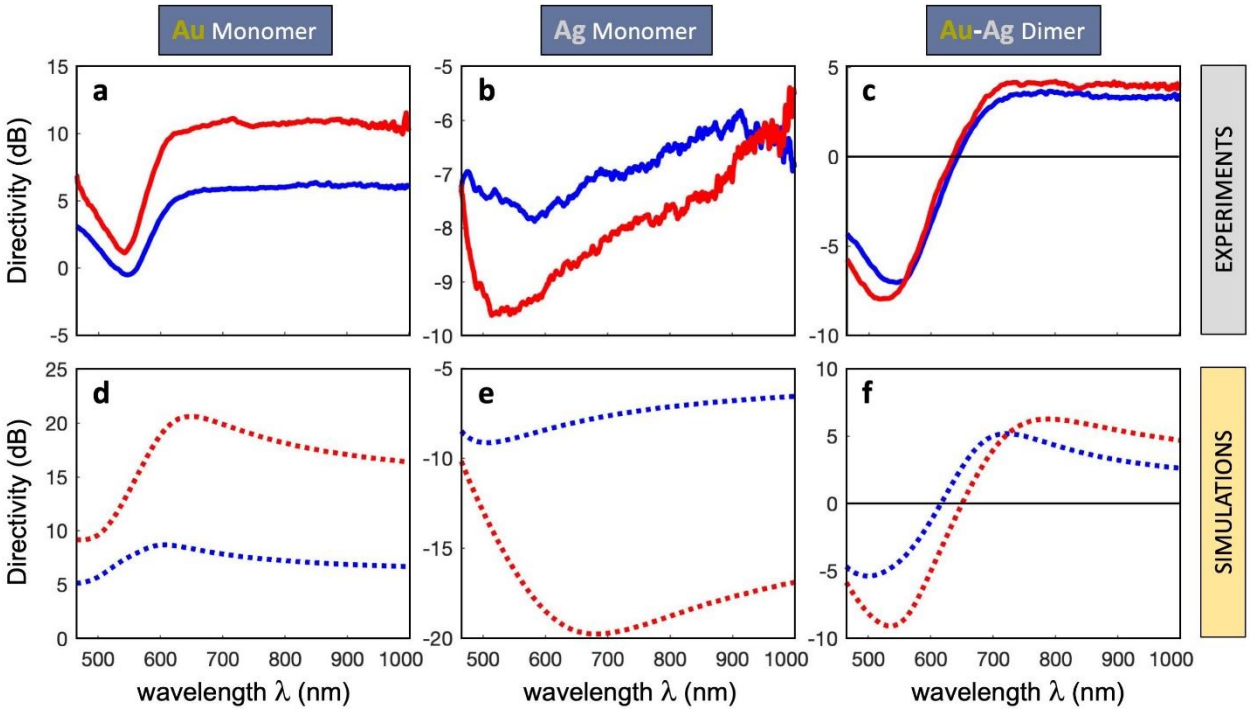

Figure 4: *Measured (a, b, c) and simulated (d, e, f) directivities at two different polar angles (Θ = 30° in black, Θ = 50° in red) for: (a, d) Au NSA monomer, (b, e) Ag NSA monomer and (c, f) Au-Ag NSA dimer configurations, respectively.*

Note that the monomeric configurations based on Au (Fig. 4a) or Ag (Fig. 4b) NSAs, even though giving rise to a wavelength dependent directional scattering, are not capable of bidirectional functionality, having no sign changes in their Directivity. Conversely, the bimetallic Au-Ag NSA uniquely provides an inversion of *D* as a function of the wavelength. The sign flips from negative to positive by increasing λ from the blue wing of the spectrum (dominated by the Ag NSA scattering) to the red one (dominated by Au NSA scattering), the zero being at around 620 nm (i.e. in correspondence to a local maximum of the transmittance spectrum of Fig.3f, placed in-between the two orthogonal plasmonic resonances of the dimer configuration). Remarkably, the maximum directivity values for both the monomer and dimer configurations are well within the same order of magnitude reported for lithographic antennas and, at the same time, show a uniform broadband response which is particularly evident in the NIR range [23,25,45].

The quasi-1D nature of the arrays and the polydispersion of the NSA morphological feature lead to the absence of collective grating effects or surface lattice resonances in their optical features and also ensure the spectrally broad response of the LSP resonance (cf. Ref. [56] for details and Fig. SI1). Therefore, the optical properties of the NSAs are dominated by the resonant features of the unit cell, which is the typical regime of metasurface operation. Thus, the color routing properties of the system are not related to complex and/or restrictive collective geometries and morphological parameters, greatly relaxing the fabrication demands and issues.

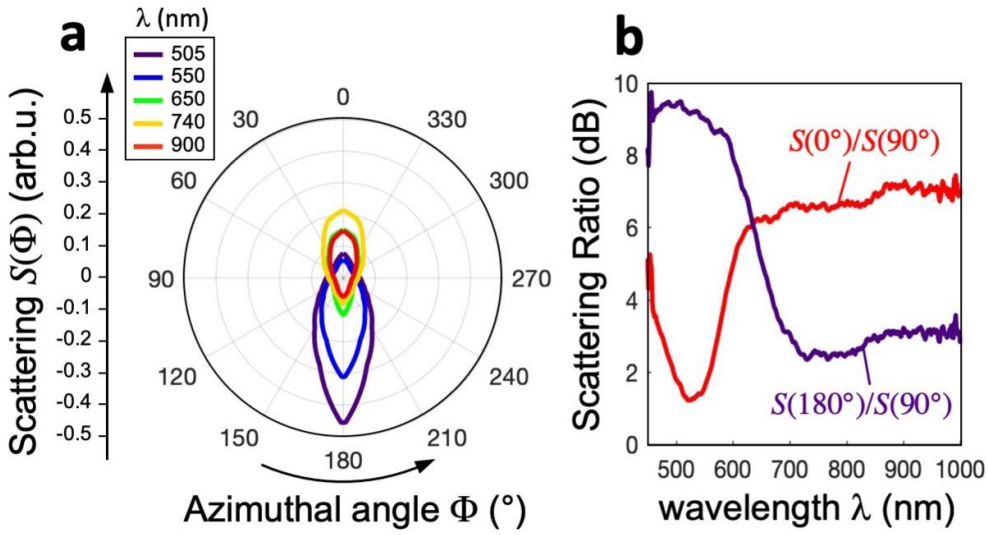

Figure 5: *(a) Azimuthal plot of the scattered light at polar angle Θ = 50° for 5 different wavelengths. (b) 90° scattering rejection ratio as a function of wavelength for left (red) and right (purple) routing operation.*

Finally, it is worth noticing that even though o implementation of the NSAs employs finite length (i.e. few μm long) structures, thus breaking the continuous translational invariance of the ideal 2D configuration, the measured azimuthal scattering pattern turns out to be well concentrated along the Φ = 0° and Φ = 180° directions of the color routing. This is especially true at around the plasmonic resonance wavelengths, as elucidated by the 90° scattering rejection ratio of Fig. 5b, defined as the ratio (in dB scale) between the light scattered at Φ = 0° (or Φ = 180°) and that scattered at Φ = 90° for a given polar angle (Θ = 50° in the present case). A related issue pertains to the polarization sensitivity of our structures, which belongs to the quasi-1D configuration [54,57]. To address this point, we have repeated all the optical experiments with TE polarization (electric field of the source parallel to the nanostrips i.e. orthogonal to their cross-sectional plane – see top-view sketch in Figure 3l). The results indicate a very shallow directional scattering in terms of the azimuthal angle, and the absence of bidirectional wavelength sensitivity which is consistent with the basic theoretical argument according to which no plasmonic resonances can be excited under TE illumination.

4.2 - Conclusions

In this chapter I demonstrated broadband color routing from cross-polarized detuned plasmonic

nanoantennas, fabricated over a large area (cm^2) via self-organized metal confinement on faceted glass templates. The latter represents a natural platform for guiding the growth of vertically tilted nanoantenna arrays in a single maskless step. The resulting plasmonic metasurfaces exhibit highly directional and wavelength selective properties which are widely tunable and not related to complex and/or restrictive collective geometries and morphological parameters, greatly relaxing the fabrication demands and related critical issues. All the main optical and scattering features of the structures can be effectively predicted by numerical simulations in which the key parameters (such as antennas tilt and materials dielectric function) can be readily implemented by our self-organization methods. Since the scattering directivities of the proposed beam splitters are competitive with the figures of merit of lithographically patterned nanoantennas, these results can enable large-area real world metasurfaces to be operated as flat optics broadband color routers, with potential impact on a wide range of applications from telecom photonics, to optical nanosensing.

4.3 - Experimental

Tilted optical nanoantennas fabrication

A soda-lime glass substrate (20*20*2 mm) is repeatedly rinsed in ethanol and acetone. The sample is then placed in a custom-made vacuum chamber and irradiated with an 800 eV low energy defocused Ar^+ ion beam (gas purity N5.0). A biased tungsten filament avoids charge build-up through thermionic electron emission. The ion beam illuminates the glass surface at an incident angle of $\theta = 30°$ with respect to its normal. The ion fluence corresponds to 1.4×10^{19} ions/cm^2 and the glass temperature is fixed at about 680 K during the Ion Beam Sputtering (IBS) process. After the rippled pattern is formed on the glass surface, thermal Au deposition is performed on the rippled facets at a glancing angle $\theta = 55°$ with respect to the flat sample normal. The Au beam directly illuminates the glass facets tilted at +35° while the opposite facets are completely shadowed. By means of a calibrated quartz microbalance, the thickness h of the Au stripes can be evaluated by basic geometrical arguments given the Au thickness (h_0) deposited on a flat surface facing the crucible at normal incidence and the average slope of the illuminated facet measured with AFM as $h=h_0 \times cos(55° - 35°)$. The sample is then put in a custom-made RF sputtering chamber where a layer of SiO_2 is conformally grown all over the surface using a 3" quartz target. The silica

layer thickness was monitored by means of a calibrated quartz microbalance. The RF sputtering experiment is run in Argon atmosphere at a power *P=60 W*, sample-target distance *d=8.5 cm* and total pressure of about $P=7\times10^{-2}$ *mbar*. Finally, Ag stripes are confined on the rippled facets tilted at -50°, now coated with a conformal SiO_x layer, by using the same strategy and arguments already described for the Au ones.

Morphological characterization

The rippled glass template morphology was characterized by means of an atomic force microscope (Nanosurf S Mobile), running in tapping mode. The average periodicity and slope of the glass ripples were computed from the statistical analysis of AFM topographies by means of WSxM software. Top view and cross section back scattered electrons images of the bimetallic nanoantennas array were acquired by means of a scanning electron microscope (Hitachi VP-SEM SU3500), operating in the 10-15 kV accelarating voltage range. Statistical analysis was performed on the SEM images by means of ImageJ software in order to evaluate the average antennas width and average antennas and silica gap thicknesses.

Extinction and scattering measurements

VIS-NIR extinction measurements were performed at normal incidence using a halogen-deuterium compensated lamp (DH-2000-BAL, Mikropak) as source and a solid-state spectrometer (HR4000, Ocean Optics), operating in the wavelength range 300−1100 nm, as detector. Scattering spectra were acquired by employing a custom made scatterometer which can collect light as a continous function of the azimuthal angle, for a fixed selection of polar angles. The sample was illuminated from the bare flat glass side with a Visible and Near-Infra-Red broadband laser source (SuperK COMPACT by NKT Photonics) pulsed at high frequency (~10 kHz) to have a stronger signal intensity. A fiber coupled spectrometer Ocean Optics HR4000 was again used as detector. For both extinction and scattering measurements, the light source was linearly polarized to investigate the anisotropic optical properties of the nanoantennas array.

References

(1) Gramotnev, D. K.; Bozhevolnyi, S. I. Plasmonics beyond the Diffraction Limit. *Nature Photonics* **2010**, *4* (2), 83–91. https://doi.org/10.1038/nphoton.2009.282.

(2) Lal, S.; Link, S.; Halas, N. J. Nano-Optics from Sensing to Waveguiding. *Nature Photonics* **2007**, *1* (11), 641–648. https://doi.org/10.1038/nphoton.2007.223.

(3) Maier, S. A.; Atwater, H. A. Plasmonics: Localization and Guiding of Electromagnetic Energy in Metal/Dielectric Structures. *Journal of Applied Physics* **2005**, *98* (1), 011101. https://doi.org/10.1063/1.1951057.

(4) Muhlschlegel, P. Resonant Optical Antennas. *Science* **2005**, *308* (5728), 1607–1609. https://doi.org/10.1126/science.1111886.

(5) Ciraci, C.; Hill, R. T.; Mock, J. J.; Urzhumov, Y.; Fernandez-Dominguez, A. I.; Maier, S. A.; Pendry, J. B.; Chilkoti, A.; Smith, D. R. Probing the Ultimate Limits of Plasmonic Enhancement. *Science* **2012**, *337* (6098), 1072–1074. https://doi.org/10.1126/science.1224823.

(6) Akselrod, G. M.; Argyropoulos, C.; Hoang, T. B.; Ciracì, C.; Fang, C.; Huang, J.; Smith, D. R.; Mikkelsen, M. H. Probing the Mechanisms of Large Purcell Enhancement in Plasmonic Nanoantennas. *Nature Photonics* **2014**, *8* (11), 835–840. https://doi.org/10.1038/nphoton.2014.228.

(7) Jones, S.; Andrén, D.; Karpinski, P.; Käll, M. Photothermal Heating of Plasmonic Nanoantennas: Influence on Trapped Particle Dynamics and Colloid Distribution. *ACS Photonics* **2018**, *5* (7), 2878–2887. https://doi.org/10.1021/acsphotonics.8b00231.

(8) Giordano, M. C.; Foti, A.; Messina, E.; Gucciardi, P. G.; Comoretto, D.; Buatier de Mongeot, F. SERS Amplification from Self-Organized Arrays of Plasmonic Nanocrescents. *ACS Applied Materials & Interfaces* **2016**, *8* (10), 6629–6638. https://doi.org/10.1021/acsami.5b11843.

(9) Brown, L. V.; Yang, X.; Zhao, K.; Zheng, B. Y.; Nordlander, P.; Halas, N. J. Fan-Shaped Gold Nanoantennas above Reflective Substrates for Surface-Enhanced Infrared Absorption (SEIRA). *Nano Letters* **2015**, *15* (2), 1272–1280. https://doi.org/10.1021/nl504455s.

(10) Kuznetsov, A. I.; Miroshnichenko, A. E.; Brongersma, M. L.; Kivshar, Y. S.; Luk'yanchuk, B. Optically Resonant Dielectric Nanostructures. *Science* **2016**, *354* (6314), aag2472. https://doi.org/10.1126/science.aag2472.

(11) Tagliabue, G.; Jermyn, A. S.; Sundararaman, R.; Welch, A. J.; DuChene, J. S.; Pala, R.; Davoyan, A. R.; Narang, P.; Atwater, H. A. Quantifying the Role of Surface Plasmon Excitation and Hot Carrier Transport in Plasmonic Devices. *Nature Communications* **2018**, *9* (1). https://doi.org/10.1038/s41467-018-05968-x.

(12) Kim, Y.; Wu, P. C.; Sokhoyan, R.; Mauser, K.; Glaudell, R.; Kafaie Shirmanesh, G.; Atwater, H. A. Phase Modulation with Electrically Tunable Vanadium Dioxide Phase-Change Metasurfaces. *Nano Letters* **2019**, *19* (6), 3961–3968. https://doi.org/10.1021/acs.nanolett.9b01246.

(13) Pors, A.; Nielsen, M. G.; Valle, G. D.; Willatzen, M.; Albrektsen, O.; Bozhevolnyi, S. I. Plasmonic Metamaterial Wave Retarders in Reflection by Orthogonally Oriented Detuned Electrical Dipoles. *Optics Letters* **2011**, *36* (9), 1626. https://doi.org/10.1364/OL.36.001626.

(14) Yu, N.; Aieta, F.; Genevet, P.; Kats, M. A.; Gaburro, Z.; Capasso, F. A Broadband, Background-Free Quarter-Wave Plate Based on Plasmonic Metasurfaces. *Nano Letters* **2012**, *12* (12), 6328–6333. https://doi.org/10.1021/nl303445u.

(15) Boroviks, S.; Deshpande, R. A.; Mortensen, N. A.; Bozhevolnyi, S. I. Multifunctional Metamirror: Polarization Splitting and Focusing. *ACS Photonics* **2018**, *5* (5), 1648–1653. https://doi.org/10.1021/acsphotonics.7b01091.

(16) Aas, L. M. S.; Kildemo, M.; Martella, C.; Giordano, M. C.; Chiappe, D.; Buatier de Mongeot, F. Optical Properties of Biaxial Nanopatterned Gold Plasmonic Nanowired Grid Polarizer. *Optics Express* **2013**, *21* (25), 30918. https://doi.org/10.1364/OE.21.030918.

(17) Curto, A. G.; Taminiau, T. H.; Volpe, G.; Kreuzer, M. P.; Quidant, R.; van Hulst, N. F. Multipolar Radiation of Quantum Emitters with Nanowire Optical Antennas. *Nature Communications* **2013**, *4* (1). https://doi.org/10.1038/ncomms2769.

(18) Curto, A. G.; Volpe, G.; Taminiau, T. H.; Kreuzer, M. P.; Quidant, R.; van Hulst, N. F. Unidirectional Emission of a Quantum Dot Coupled to a Nanoantenna. *Science* **2010**, *329* (5994), 930–933. https://doi.org/10.1126/science.1191922.

(19) Cihan, A. F.; Curto, A. G.; Raza, S.; Kik, P. G.; Brongersma, M. L. Silicon Mie Resonators for Highly Directional Light Emission from Monolayer MoS2. *Nature Photonics* **2018**, *12* (5), 284–290. https://doi.org/10.1038/s41566-018-0155-y.

(20) Kosako, T.; Kadoya, Y.; Hofmann, H. F. Directional Control of Light by a Nano-Optical Yagi–Uda Antenna. *Nature Photonics* **2010**, *4* (5), 312–315. https://doi.org/10.1038/nphoton.2010.34.

(21) Shen, H.; Chou, R. Y.; Hui, Y. Y.; He, Y.; Cheng, Y.; Chang, H.-C.; Tong, L.; Gong, Q.; Lu, G. Directional Fluorescence Emission from a Compact Plasmonic-Diamond Hybrid Nanostructure: Directional Fluorescence Emission…. *Laser & Photonics Reviews* **2016**, *10* (4), 647–655. https://doi.org/10.1002/lpor.201600021.

(22) Vercruysse, D.; Neutens, P.; Lagae, L.; Verellen, N.; Van Dorpe, P. Single Asymmetric Plasmonic Antenna as a Directional Coupler to a Dielectric Waveguide. *ACS Photonics* **2017**, *4* (6), 1398–1402. https://doi.org/10.1021/acsphotonics.7b00038.

(23) Shegai, T.; Chen, S.; Miljković, V. D.; Zengin, G.; Johansson, P.; Käll, M. A Bimetallic Nanoantenna for Directional Colour Routing. *Nature Communications* **2011**, *2* (1). https://doi.org/10.1038/ncomms1490.

(24) Shibanuma, T.; Matsui, T.; Roschuk, T.; Wojcik, J.; Mascher, P.; Albella, P.; Maier, S. A. Experimental Demonstration of Tunable Directional Scattering of Visible Light from All-Dielectric Asymmetric Dimers. *ACS Photonics* **2017**, *4* (3), 489–494. https://doi.org/10.1021/acsphotonics.6b00979.

(25) Li, J.; Verellen, N.; Vercruysse, D.; Bearda, T.; Lagae, L.; Van Dorpe, P. All-Dielectric Antenna Wavelength Router with Bidirectional Scattering of Visible Light. *Nano Letters* **2016**, *16* (7), 4396–4403. https://doi.org/10.1021/acs.nanolett.6b01519.

(26) Yan, C.; Yang, K.-Y.; Martin, O. J. F. Fano-Resonance-Assisted Metasurface for Color Routing. *Light: Science & Applications* **2017**, *6* (7), e17017–e17017. https://doi.org/10.1038/lsa.2017.17.

(27) Liu, B.; Chen, S.; Zhang, J.; Yao, X.; Zhong, J.; Lin, H.; Huang, T.; Yang, Z.; Zhu, J.; Liu, S.; et al. A Plasmonic Sensor Array with Ultrahigh Figures of Merit and Resonance Linewidths down to 3 Nm. *Advanced Materials* **2018**, *30* (12), 1706031. https://doi.org/10.1002/adma.201706031.

(28) Cetin, A. E.; Iyidogan, P.; Hayashi, Y.; Wallen, M.; Vijayan, K.; Tu, E.; Nguyen, M.; Oliphant, A. Plasmonic Sensor Could Enable Label-Free DNA Sequencing. *ACS Sensors* **2018**, *3* (3), 561–568. https://doi.org/10.1021/acssensors.7b00957.

(29) Atwater, H. A.; Polman, A. Plasmonics for Improved Photovoltaic Devices. *Nature Materials* **2010**, *9* (3), 205–213. https://doi.org/10.1038/nmat2629.

(30) Knight, M. W.; Sobhani, H.; Nordlander, P.; Halas, N. J. Photodetection with Active Optical Antennas. *Science* **2011**, *332* (6030), 702–704. https://doi.org/10.1126/science.1203056.

(31) Anker, J. N.; Hall, W. P.; Lyandres, O.; Shah, N. C.; Zhao, J.; Van Duyne, R. P. Biosensing with Plasmonic Nanosensors. *Nature Materials* **2008**, *7* (6), 442–453. https://doi.org/10.1038/nmat2162.

(32) Kneipp, K.; Moskovits, M.; Kneipp, H. *Surface-Enhanced Raman Scattering Physics and Applications*; 2006.

(33) Neubrech, F.; Huck, C.; Weber, K.; Pucci, A.; Giessen, H. Surface-Enhanced Infrared Spectroscopy Using Resonant Nanoantennas. *Chemical Reviews* **2017**, *117* (7), 5110–5145. https://doi.org/10.1021/acs.chemrev.6b00743.

(34) Dipalo, M.; Messina, G. C.; Amin, H.; La Rocca, R.; Shalabaeva, V.; Simi, A.; Maccione, A.; Zilio, P.; Berdondini, L.; De Angelis, F. 3D Plasmonic Nanoantennas Integrated with MEA Biosensors. *Nanoscale* **2015**, *7* (8), 3703–3711. https://doi.org/10.1039/C4NR05578K.

(35) Shegai, T.; Johansson, P.; Langhammer, C.; Käll, M. Directional Scattering and Hydrogen Sensing by Bimetallic Pd–Au Nanoantennas. *Nano Letters* **2012**, *12* (5), 2464–2469.

https://doi.org/10.1021/nl300558h.

(36) Ho, J.; Fu, Y. H.; Dong, Z.; Paniagua-Dominguez, R.; Koay, E. H. H.; Yu, Y. F.; Valuckas, V.; Kuznetsov, A. I.; Yang, J. K. W. Highly Directive Hybrid Metal–Dielectric Yagi-Uda Nanoantennas. *ACS Nano* **2018**, *12* (8), 8616–8624. https://doi.org/10.1021/acsnano.8b04361.

(37) Dregely, D.; Taubert, R.; Dorfmüller, J.; Vogelgesang, R.; Kern, K.; Giessen, H. 3D Optical Yagi–Uda Nanoantenna Array. *Nature Communications* **2011**, *2* (1). https://doi.org/10.1038/ncomms1268.

(38) Dregely, D.; Lindfors, K.; Lippitz, M.; Engheta, N.; Totzeck, M.; Giessen, H. Imaging and Steering an Optical Wireless Nanoantenna Link. *Nature Communications* **2014**, *5* (1). https://doi.org/10.1038/ncomms5354.

(39) Vaskin, A.; Bohn, J.; Chong, K. E.; Bucher, T.; Zilk, M.; Choi, D.-Y.; Neshev, D. N.; Kivshar, Y. S.; Pertsch, T.; Staude, I. Directional and Spectral Shaping of Light Emission with Mie-Resonant Silicon Nanoantenna Arrays. *ACS Photonics* **2018**, *5* (4), 1359–1364. https://doi.org/10.1021/acsphotonics.7b01375.

(40) Fu, Y. H.; Kuznetsov, A. I.; Miroshnichenko, A. E.; Yu, Y. F.; Luk'yanchuk, B. Directional Visible Light Scattering by Silicon Nanoparticles. *Nature Communications* **2013**, *4* (1). https://doi.org/10.1038/ncomms2538.

(41) Neugebauer, M.; Woźniak, P.; Bag, A.; Leuchs, G.; Banzer, P. Polarization-Controlled Directional Scattering for Nanoscopic Position Sensing. *Nature Communications* **2016**, *7* (1). https://doi.org/10.1038/ncomms11286.

(42) Ma, C.; Yan, J.; Huang, Y.; Yang, G. Directional Fano Resonance in an Individual GaAs Nanospheroid. *Small* **2019**, *15* (18), 1900546. https://doi.org/10.1002/smll.201900546.

(43) Hancu, I. M.; Curto, A. G.; Castro-López, M.; Kuttge, M.; van Hulst, N. F. Multipolar Interference for Directed Light Emission. *Nano Letters* **2014**, *14* (1), 166–171. https://doi.org/10.1021/nl403681g.

(44) Coenen, T.; Bernal Arango, F.; Femius Koenderink, A.; Polman, A. Directional Emission from a Single Plasmonic Scatterer. *Nature Communications* **2014**, *5* (1). https://doi.org/10.1038/ncomms4250.

(45) Vercruysse, D.; Sonnefraud, Y.; Verellen, N.; Fuchs, F. B.; Di Martino, G.; Lagae, L.; Moshchalkov, V. V.; Maier, S. A.; Van Dorpe, P. Unidirectional Side Scattering of Light by a Single-Element Nanoantenna. *Nano Letters* **2013**, *13* (8), 3843–3849. https://doi.org/10.1021/nl401877w.

(46) Shegai, T.; Miljković, V. D.; Bao, K.; Xu, H.; Nordlander, P.; Johansson, P.; Käll, M. Unidirectional Broadband Light Emission from Supported Plasmonic Nanowires. *Nano Letters*

2011, *11* (2), 706–711. https://doi.org/10.1021/nl103834y.

(47) Pellegrini, G.; Mazzoldi, P.; Mattei, G. Asymmetric Plasmonic Nanoshells as Subwavelength Directional Nanoantennas and Color Nanorouters: A Multipole Interference Approach. *The Journal of Physical Chemistry C* **2012**, *116* (40), 21536–21546. https://doi.org/10.1021/jp306025b.

(48) Huang, L.; Chen, X.; Mühlenbernd, H.; Li, G.; Bai, B.; Tan, Q.; Jin, G.; Zentgraf, T.; Zhang, S. Dispersionless Phase Discontinuities for Controlling Light Propagation. *Nano Letters* **2012**, *12* (11), 5750–5755. https://doi.org/10.1021/nl303031j.

(49) Davis, M. S.; Zhu, W.; Xu, T.; Lee, J. K.; Lezec, H. J.; Agrawal, A. Aperiodic Nanoplasmonic Devices for Directional Colour Filtering and Sensing. *Nature Communications* **2017**, *8* (1). https://doi.org/10.1038/s41467-017-01268-y.

(50) Wu, P. C.; Pala, R. A.; Kafaie Shirmanesh, G.; Cheng, W.-H.; Sokhoyan, R.; Grajower, M.; Alam, M. Z.; Lee, D.; Atwater, H. A. Dynamic Beam Steering with All-Dielectric Electro-Optic III–V Multiple-Quantum-Well Metasurfaces. *Nature Communications* **2019**, *10* (1). https://doi.org/10.1038/s41467-019-11598-8.

(51) M. Barelli, A. Mazzanti, M.C. Giordano, G. Della Valle, F. Buatier de Mongeot. Flat-Optics Large Area Color Routing via Cross-Polarized Detuned Plasmonic Nanoantennas. *submitted to Nature Communications*

(52) Della Valle, G.; Sondergaard, T.; Bozhevolnyi, S. I. Plasmon-Polariton Nano-Strip Resonators: From Visible to Infra-Red. *Optics Express* **2008**, *16* (10), 6867. https://doi.org/10.1364/OE.16.006867.

(53) Giordano, M. C.; de Mongeot, F. B. Anisotropic Nanoscale Wrinkling in Solid-State Substrates. *Advanced Materials* **2018**, *30* (30), 1801840. https://doi.org/10.1002/adma.201801840.

(54) Giordano, M. C.; Longhi, S.; Barelli, M.; Mazzanti, A.; Buatier de Mongeot, F.; Della Valle, G. Plasmon Hybridization Engineering in Self-Organized Anisotropic Metasurfaces. *Nano Research* **2018**, *11* (7), 3943–3956. https://doi.org/10.1007/s12274-018-1974-3.

(55) Johnson, P. B.; Christy, R. W. Optical Constants of the Noble Metals. *Physical Review B* **1972**, *6* (12), 4370–4379. https://doi.org/10.1103/PhysRevB.6.4370.

(56) Della Valle, G.; Polli, D.; Biagioni, P.; Martella, C.; Giordano, M. C.; Finazzi, M.; Longhi, S.; Duò, L.; Cerullo, G.; Buatier de Mongeot, F. Self-Organized Plasmonic Metasurfaces for All-Optical Modulation. *Physical Review B* **2015**, *91* (23). https://doi.org/10.1103/PhysRevB.91.235440.

(57) Repetto, D.; Giordano, M. C.; Martella, C.; Buatier de Mongeot, F. Transparent Aluminium

Nanowire Electrodes with Optical and Electrical Anisotropic Response Fabricated by Defocused Ion Beam Sputtering. *Applied Surface Science* **2015**, *327*, 444–452. https://doi.org/10.1016/j.apsusc.2014.11.134.

CHAPTER 5

Self-Organized Nanorod Arrays for Large-Area Surface Enhanced Infra-Red Absorption

Introduction

Infra-Red (IR) spectroscopy and nanoimaging [1–7] have recently attracted increasing attention due the possibility to probe vibrational modes of a broad range of molecular species in a non-destructive way and to detect strongly subwavelength photonic and plasmonic modes in novel nanomaterials [8–12]. In particular Fourier Transform IR Spectroscopy (FTIR) [13,14] has enabled the direct detection of a variety of molecular vibrational modes in the Mid-IR spectrum (3 μm - 25 μm), showing the great potential of IR spectroscopy in different fields ranging from nanophotonics [15,16] to biology and life sciences [4,17]. However, a very high number of absorption bands limit the possibility to clearly identify specific molecular features in the so-called *fingerprint spectral region* extending from 700 cm^{-1} to 1500 cm^{-1}. Conversely, the vibrational modes of carbon- or nitrogen- based functional groups can be easily identified in the spectral window from about 2000 cm^{-1} to 3500 cm^{-1} (*functional group window).*

Despite the great advantage given by the low-energy excitation in the Near- and Mid-IR, the tiny vibrational absorption cross section practically limits the detection sensitivity in standard FTIR spectroscopy or in alternative configurations based on grazing incidence IR reflection-absorption spectroscopy (IRRAS) [18,19] on continuous metallic films, where vibrational signals of the order of 0.1% can be detected for molecular concentration at the monolayer level. Strong light-matter interaction of plasmonic nanoantennas [20–26] offers a unique opportunity for the effective improvement of the IR absorption sensitivity below the nM concentration level in Surface Enhanced Infrared Absorption Spectroscopy (SEIRA) [7,27–33]. Molecular infrared absorption is indeed proportional to the orientation of the molecule with respect to the incident radiation, to the change of the dipole moment and to the square of the local electric field at the molecule coordinates, at its absorption frequencies [34]. Plasmonic hot spots resonances can couple with sharp molecular vibronic fingerprints leading to a Fano-like electro-vibrational interaction and to

the enhancement of molecular infrared absportion signal by several orders of magnitude. The repoducibilty of SEIRA signal from plasmonic functionalized surfaces is an open issue shared with the SERS community. Recently, highly reproducible SEIRA activity has been demonstrated in well-defined noble metal nanoresonators engineered by top-down nanoscale lithography [27,28,31]. Here the nanoscale control on the nanoantennas size, shape and/or inter-spacing has given a deep insight into the more efficient nanoresonator configurations highlighting the key role of the active hot-spots for IR biosensing [7,31,35]. In parallel, IR detection has been recently demonstrated by exploiting lithographically designed nanodevices based on nanostructures or atomic two-dimensional materials [30,7,36–38]. In this way high sensitivity and tunable IR optical response can be achieved but the lithographic nanofabrication practically limits the active sensing area in the range of 100 μm x 100 μm, demanding for highly focused optical beams and/or complex detection configurations [13-20].

Conversely, the capability to detect and identify a set of molecules or biomarkers within unknown biological samples is highly desirable for all day life biomedical applications and has recently motivated the devising of advanced microfluidic biosensor chips [39,40] based on nanopatterned plasmonic templates. The development of reliable, large area plasmonic platforms [41–44] thus represents a crucial issue in view of cost-effective biosensors potentially relevant for medical diagnostic and monitoring [45,46]. Real world applications require cost-effective methods able to control material functionalization over macroscopic areas thus enabling the excitation of statistically relevant ensembles of molecules. In the context of SEIRA spectroscopy pioneering experiments were performed by exploiting large area nanoparticle films [47,48] showing a relatively weak visibility of the IR molecular absorption in the range of 0.7%, and limited homogeneity over macroscopic scale.

During my PhD I worked on self-organized (SO) nanorod arrays supported on large area (cm^2) nanopatterned templates characterized by highly sensitive and reproducible biosensing capabilities [49]. The hot IBS soda-lime glass nanopatterning process previously described (in section 1.2.3 of this thesis and exploited for the plasmonic funcionalizations presented in chapter 2, 3 and 4 of this thesis) was modified to enable a maskless, single step method for the engineering of short aligned Au nanorod arrays. Such functionalized surfaces show polarization-sensitive broadband plasmonic modes tuned across the Near- and Mid-IR spectral region (2500 cm^{-1} - 5000 cm^{-1}), resonant with

the so-called *functional group window*. Under this condition superior Surface Enhanced Infra-Red Absorption sensitivity at the monolayer level over macroscopic sensor areas was demonstrated. The peculiar capability of this SO approach to engineer aligned plasmonic nanorods with high density (~40 μm^{-2}) of nanoscale gaps allows to strongly enhance the SEIRA sensitivity with respect to alternative large area plasmonic templates characterized by active antennas spread on the surface (density ~ few μm^{-2} [48]). The self-organized engineering of the active hot-spots enables the detection of Fano-like lineshapes in SEIRA from self-assembled monolayers of Octadecanthiol (ODT) molecules with visibility improved up to 5.7 % and high stability over large area. This figure arises from an enhancement factor of the single SO plasmonic antennas of about 75000 which is competitive to lithographic antennas [27,35] confined on microscopic active areas, thus enabling large-area IR spectroscopy and applications in cost-effective broadband on-chip biosensors.

5.1 Results and discussion

IR optical characterization of self-organized "long "Au nanoantennas

The optical characterization of Au NW arrays grown on hot IBS nanorippled soda-lime glasses, analogous to the ones described in Chapter 3 (section 3.2), was extended in the Near- and Mid-IR spectral range by means of FTIR spectroscopy (Fig. 1e). The average NWs width is 100 nm while their thickness is 23 nm. As clearly shown by the spectra of Figure 1e, in extinction configuration a strong optical dichroism has been detected across the whole Near- and Mid-IR spectral region, as well as in the alredy investigated Near-Ultra-Violet (NUV) and Visible spectral windows. In this chapter, comapred to all the other thesis chapters, I will use for convenience wavenumbers instead of nanometers to express photonic wavelenghts, and a different nomenclature of polarization configurations in the presentiation of the spectroscopic data. Here the normal incidence optical transmittance detected for two different polarizations of the incident light, either transversal ($T_{\perp}$ - (TM in other chapters) - dashed line, see sketch in Fig. 1c) or longitudinal ($T_{\parallel}$ - (TE in other chapters) - continuous line) to the nanostripe long-axis, is shown. In the NUV spectrum above 19000 cm^{-1} (wavelength λ below 526 nm) the optical response is dominated by the excitation of s-d interband transition in gold. In the VIS spectrum a narrow-band transmittance minimum is selectively detected for transversal polarization (dashed line in Fig. 1e) at about 16670

cm^{-1} (i.e. λ =600 nm) due to the excitation of a Localized Surface Plasmon (LSP) resonance along the nanostripes confined axis [20,50,51]; a high transparency up to 96% is instead detected in the Near- and Mid-IR spectral range due to the strongly subwavelength confinement in laterally disconnected nanostripes.

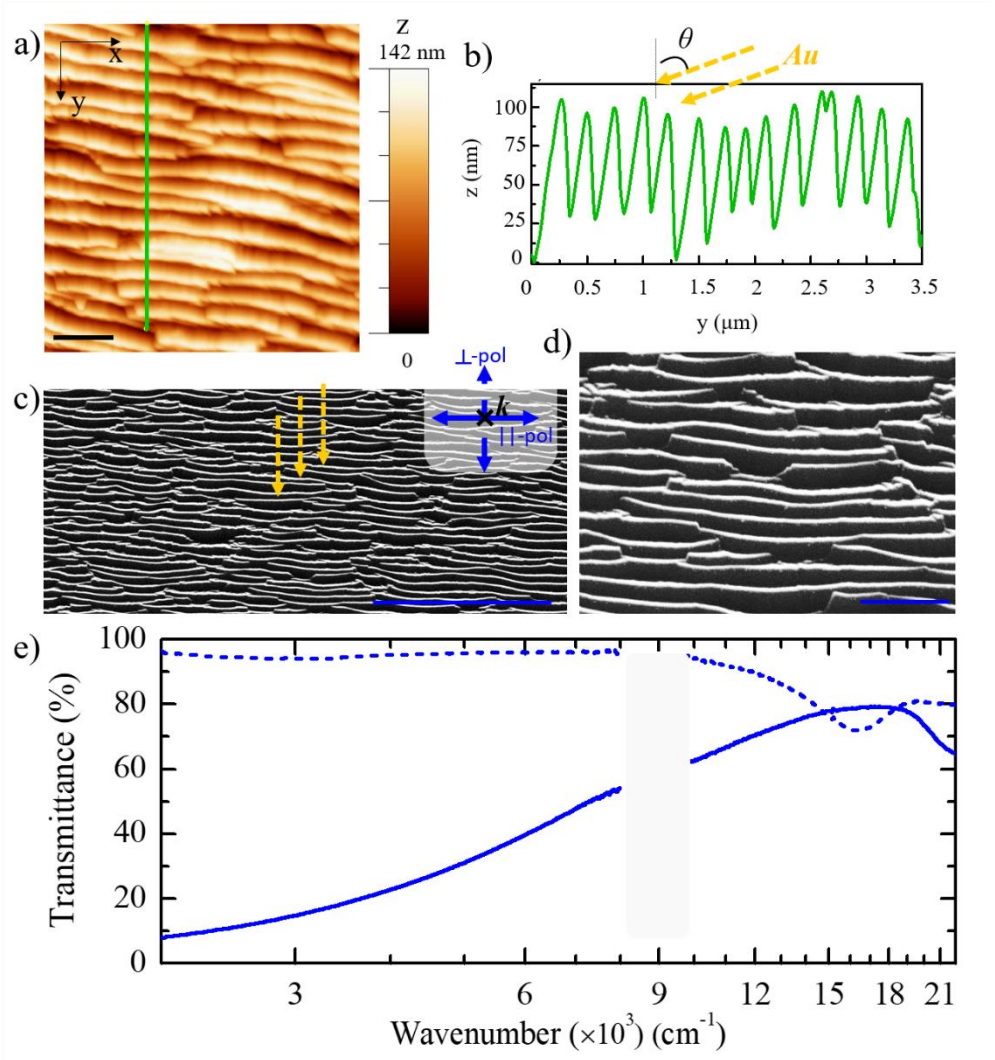

Figure 1: a,b) *AFM topography and cross section profile, respectively, of a high aspect ratio rippled glass template. The scale bar in panel a) corresponds to 800 nm.* ***c,d)*** *Large area and zoomed SEM image of quasi-1D Au nanostripe arrays confined on the self-organized glass template. The scale bars in c) and d) correspond to 5 μm and 1 μm, respectively.* ***e)*** *Optical transmission spectra of the Au nanostripe arrays detected for longitudinal (continuous line) and transversal (dashed line) polarization of the incident light with respect to the nanostripes axis. The spectra characterize the response of the arrays from the Mid-IR to the Near-UV spectral region.*

Conversely, for longitudinal polarization, the transmittance spectrum is dominated by a monotonic decrease within the whole detected IR window below 8000 cm^{-1}, due to the stronger Au reflectivity at lower frequencies. Remarkably, the large area metasurface shows a large linear IR extinction ratio $ER = T_{\perp}/T_{||}$ in the range of 4 – 12 μm, highlighting a potential of these templates as cost-effective polarimetry components in flat-optics [52–54]. The detected optical behavior suggests that the plasmonic resonance of stripes as long as several micrometers (Fig. 1c, 1d), when measured parallel to their long axis, is eventually red-shifted below 2000 cm^{-1} beyond the transparency range of the substrate.

Fabrication and morphological analyis of self-organized "short" Au nanoantennas

Interestingly, following top-down lithographic approaches [22,27,28,32], the near-field confinement in plasmonic nanoantennas can be exploited for selectively amplifying vibrational modes from IR-active molecular layers which are tuned in the frequency range of the *functional group window* (i.e. 2000 - 3500 cm^{-1}). In order to red-shift the plasmonic excitation in the relevant spectral range, the SO method has been modified for engineering the shape of the metallic nanoantennas, with the aim to decrease the characteristic length of the nanostripes down to the sub-micrometer range. By tailoring the ion beam irradiation of the glass substrate at the early stages of the process (i.e. reducing exposure time down to 300 s, fluence ~ 2.3 x 10^{18} ions/cm^2) the possibility to reduce the length of the wrinkle structures, preserving their anisotropic alignment was demonstrated. In particular, as shown in the AFM topography of Figure 2a, at the glass surface highly dense nanoripples are formed whose typical length is in the sub-micrometric range. Despite the self-organized patterning is here interrupted at an early stage, an anisotropic ripple morphology with a pronounced vertical dynamic up to 30 - 40 nm and lateral periodicity of about 90 nm is promptly formed (AFM image and cross section profile in Fig. 2a, 2b), thanks to the occurrence of the ion induced wrinkling instability [section 1.2.3 of the thesis and Ref. 55]. The peculiar presence of faceted ridges becomes obvious in the cross-section profile along the *y* axis (see Fig. 2a and b) which corresponds to the histogram of local slopes, $\alpha = \tan^{-1}(\frac{\partial z}{\partial y})$ in Fig. 2c, characterized by a bimodal distribution peaked at $\pm 30°$, respectively. The AFM topography of Figure 2a reveals that the ripple ridges, elongated in the horizontal direction, have a length that is broadly distributed

from about 200 nm up to about 1 μm. As a comparison, for the much higher ion doses of 1.4 x 10^{19} ions/cm^2 employed in Figure 1a, the coalescence of the short ripples into elongated faceted ridges extending up to several micrometers has taken place.

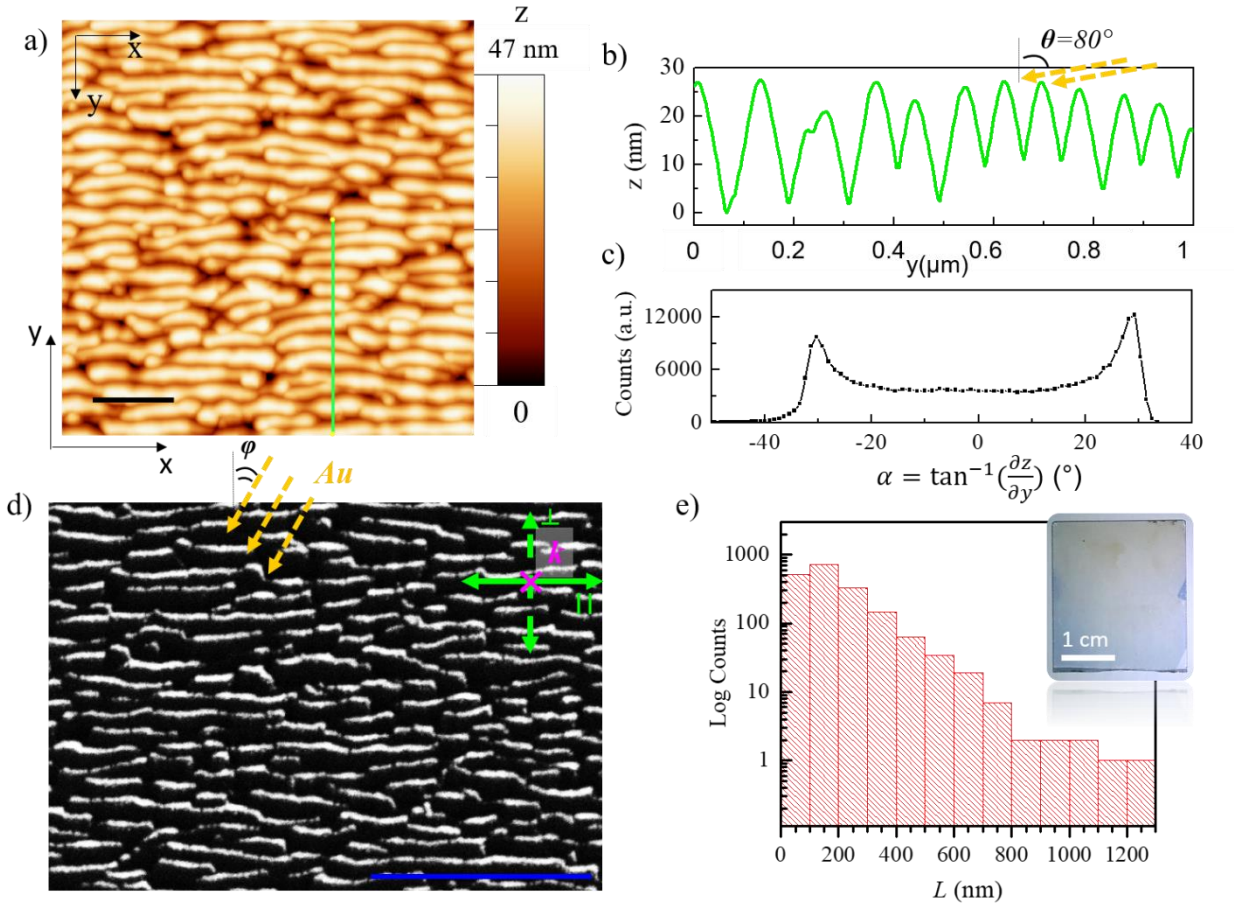

Figure 2: a,b) *AFM image and cross section profile, respectively, of aligned glass nanorods engineered by defocused ion beam irradiation. The black scale bar in panel a) corresponds to 400 nm.* ***c)*** *Histogram of the characteristic lateral slope,* $\alpha = \tan^{-1}\left(\partial z/\partial y\right)$*, of the glass nanorods pattern extracted from the AFM image.* ***d)*** *SEM image the Au nanorod arrays confined on the glass template. The blue scale bar in d) corresponds to 1 μm.* ***e)*** *Histogram of the Au nanorod length extracted from a statistic of SEM images acquired over an area of the order of few mm^2.*

In analogy to the first sample (Fig. 1), the peculiar faceted morphology of the SO wrinkled glass template enables the confinement of highly oriented tilted plasmonic antennas in register with the dielectric facets. However, here the glancing angle Au evaporation has been optimized in order to

fully exploit the presence of inter-ripples defects favoring the longitudinal disconnection of the Au nanostripes. In particular, we selected an out of plane polar angle $\theta = 80°$ and an in-plane azimuthal angle $\varphi = 30°$ (see side and top view sketches in sketches of Fig. 2b, 2d respectively). Under this condition it's possible to control longitudinal disconnections of the Au nanostripes tailored by the SO template at the micrometer and sub-micrometer level. The SEM image of Figure 2d clearly shows both laterally and longitudinally disconnected Au nanorod antennas supported by the faceted glass pattern. The local thickness *h* of the nanorods has been kept fixed at 23 nm, as in the case of Fig. 1, while the change of the nanopatterned template and of the metal deposition angle has induced a decrease of the mean nanorods width *w* to about 60 nm. The distribution of the Au nanorods length, *L*, is shown by the histogram of Figure 2e, obtained by analyzing a statistic of SEM images and highlighting a broad sub-micrometric distribution of rods length, ranging from about 100 nm up to 1.3 μm. This figure shows the capability to strongly tailor the nanostripe length by using the SO method here proposed; indeed, a strong reduction of the characteristic nanorods length from several micrometers (Fig. 1c, 1d) down to the sub-micrometer range (Fig. 2d) has been achieved. Remarkably, a key feature of this SO templates in view of cost-effective biosensing applications is the homogeneity of the nanorods morphology and periodic order over large area samples typically extending up to 2×3 cm^2 (see inset picture in Fig. 2e).

IR optical properties of "short" Au nanoantennas and SEIRA measurement on ODT monolayer

The broadband plasmonic near-field enhancement at the surface of the nanorod arrays, originated by the length distribution in Fig. 2e, can be exploited for selectively amplifying the molecular signal from a self-assembled monolayer of ODT on the surface, grown by the group of Prof. Annemarie Pucci in Heidelberg University (see Experimental section for the sample preparation details). The anisotropy of the Au nanorod arrays induces a strong dichroism in the optical behavior (Fig. 3a). Due to the reduction of the characteristic length of the nanorods in the sub-micrometer range, a broadband plasmonic resonance is now detected for longitudinal polarization of the incident light ($T_{||}$ -continuous line in Fig. 3a). Under this condition a blue-shift of the plasmonic mode in the relevant functional group spectral window is clearly revealed by comparison with the spectrum of long nanostripes (Fig.1e). The wide distribution of nanorod lengths (Fig. 2e) induces a broadband plasmonic resonance across the Near- and Mid-IR spectrum, extending from the

frequency of 2500 cm^{-1} to about 5000 cm^{-1}. This effect can be attributed to inhomogeneous and to homogeneous broadening, i.e. the incoherent superposition of the extinction signal from the array of nanorods characterized by a broad length distribution and the near-field coupling between antennas [56].

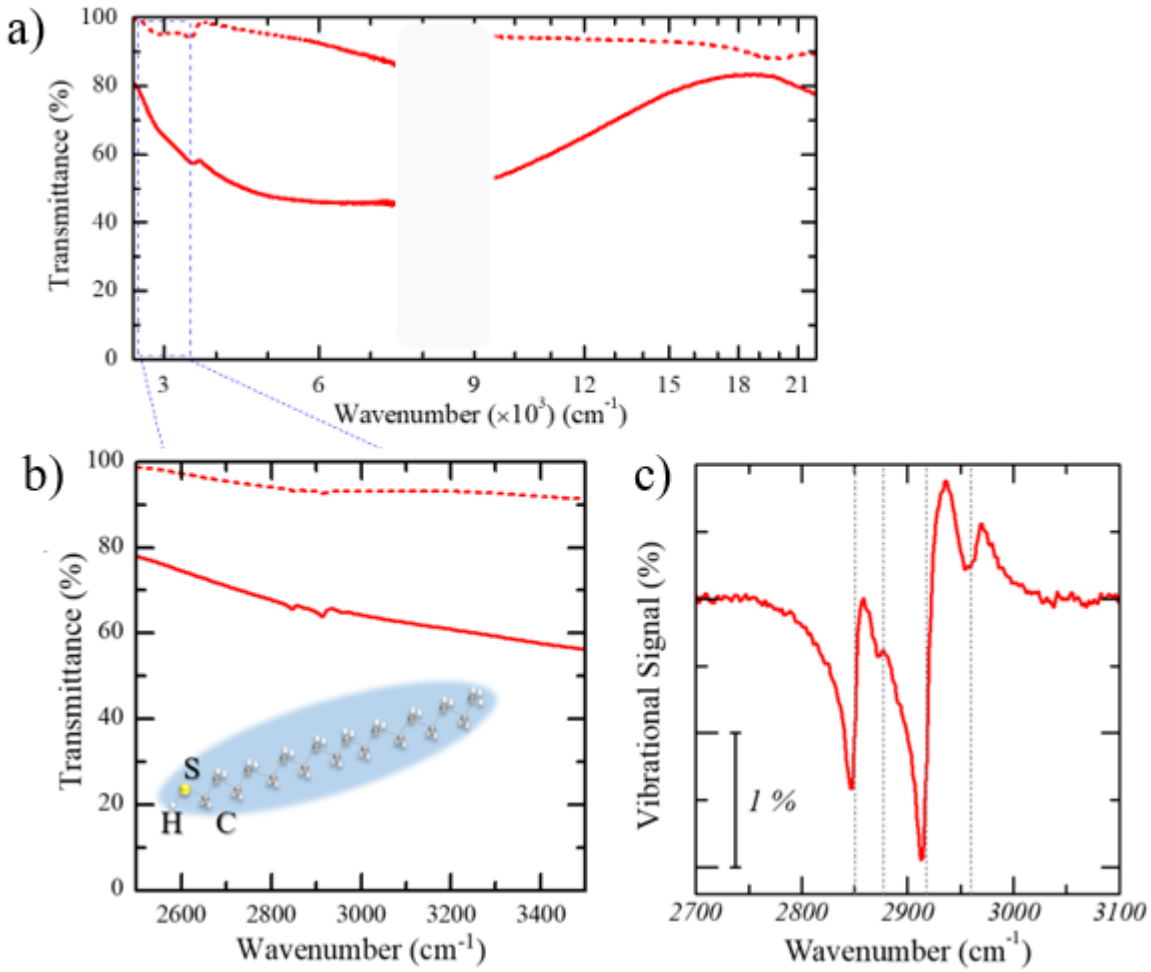

Figure 3: *(a) Near-Ultra Violet, Visible and Near-/Mid-Infra-Red (IR) optical transmission spectra of Au nanorod arrays supported on glass templates. The spectra refer to the bare Au nanorods sample shown in Fig. 2 d for longitudinal ($T_{||}$ - continuous line) and transversal ($T_{\perp}$ - dashed line) polarization of the excitation with respect to the nanorod long axis. b) Detail of panel a); zoom into the funcional group spectral window where optical modulations due to the presence of active molecules can be clearly appreciated.* ***c)*** *Vibrational signal from the ODT monolayer extracted from the spectrum of Fig. 3a as* $\left[T_{||}/T_{\perp}\right]_{\text{detected}} - \left[T_{||}/T_{\perp}\right]_{\text{optical backgroud}}$. *The SEIRA spectra show the characteristic vibrational modes of the ODT molecule which are peaked at 2850*

cm^{-1}, 2918 cm^{-1} (i.e. symmetric and antisymmetric stretching mode of the functional group CH_2) and at 2877 cm^{-1}, 2960 cm^{-1} (i.e. symmetric and antisymmetric stretching mode of the functional group CH_3).

Indeed, in Fig. 3b it can be seen how the longitudinal optical transmittance $T_{\parallel}$ is strongly modulated by the presence of the active molecules in the spectral range between 2800 cm^{-1} and 3000 cm^{-1}, where the vibrational modes of ODT are expected [27]. Conversely the molecular absorption is negligible for transversal polarization transmittance, $T_{\perp}$; this can be attributed to a small fraction of Au nanorods which detached during the molecular coating process (Fig. 4).

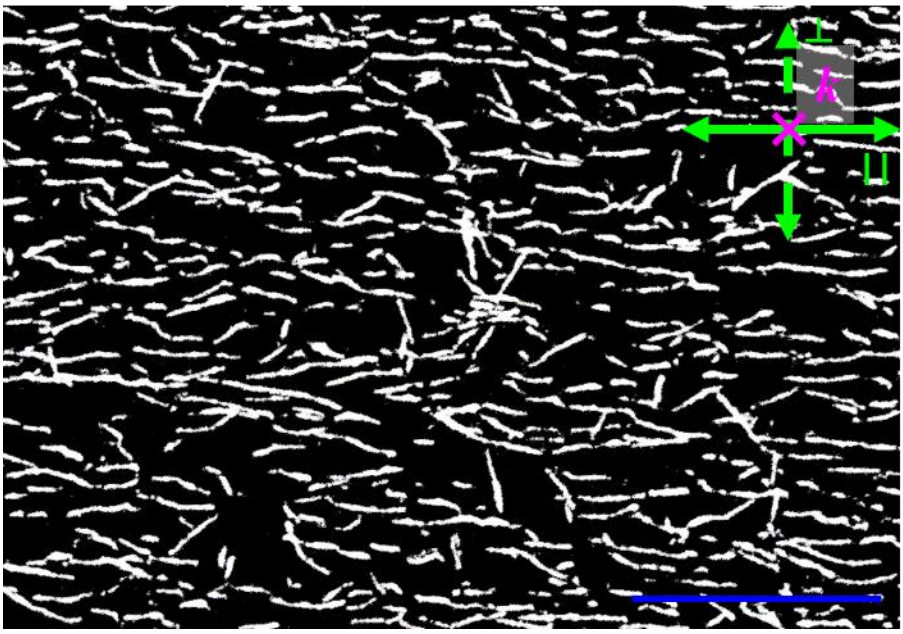

Figure 4: *SEM image of Au nanorod arrays acquired after the dip-coating with the ODT solution.*

Prospectively, this minor effect could be easily avoided by fixing the plasmonic nanostructures on the substrates with a nanometric adhesion layer (e.g. Cr, Ti) thus further improving the efficiency and stability of the nanorod templates. The dichroic optical response allows to easily normalize the detected signal by using the non-resonant polarization as a reference without need of comparison between different samples. We evaluate the vibrational signal as the difference between the detected relative transmittance $\left[T_{||}/T_{\perp}\right]_{\text{detected}}$ and the optical background from the bare plasmonic arrays prior to ODT deposition, $\left[T_{||}/T_{\perp}\right]_{\text{optical backgroud}}$, extracted as a fit from the spectra. The vibrational spectrum of Figure 3c shows multiple resonances characterized by

asymmetric line shape recalling Fano-like line shapes. In particular, two modes are detected at about 2850 cm^{-1} and 2918 cm^{-1} corresponding to the spectral position of the symmetric and antisymmetric stretching mode of the CH_2 functional group. Remarkably, the vibrational modes show a peak to peak amplitude enhanced up to 1.3 % and 2.8 %, respectively, which is a result comparable to the typical signals detected by using lithographic nanorod antennas [27,35]. Additionally, the SO plasmonic nanoantennas enable the highly sensitive detection of weaker vibrational modes of the CH_3 group at 2877 cm^{-1} and at 2960 cm^{-1}, which are due to symmetric and antisymmetric stretching, respectively.

Electromagnetic finite difference simulations (performed by our collegues in Heidelberg) allow to determine the characteristic size of antennas which are resonant in the functional group window, within a simplifying model which considers antennas as half-cylinder structures [35]. Under this assumption we obtain that antennas with lengths of about 760 nm have a longitudinal plasmonic resonance tuned to the ODT stretching vibration modes (i.e. 2800 cm^{-1}- 3000 cm^{-1}) [27]. However, a red-shift of the whole broadband plasmonic resonance is here expected with respect to the ideal simulation due to the non-cylindrical cross section of the antennas (aspect ratio $h/w \sim 0.4$), to the inter-antenna coupling in the array, to the effect of the dielectric substrate and to the phase delay upon reflection at the non-ideal antenna terminations [20,57]. The resonant antennas coupled to the ODT vibrational modes are thus expected to be shorter compared to the value suggested by simulation and to the case of decoupled lithographic antennas [32].

Fano-type coupling and SEIRA enhancement factor

The Fano-type coupling between the vibrational dipoles of the molecules and the plasmonic near-field at the hot-spots of the nanorod antennas leads here to the selective amplification of the molecular absorption lines [27,58]. In parallel, the detuning of the resonantly coupled excitations, i.e. of the narrow-band vibrational mode and the broadband plasmonic resonance, induces the characteristic asymmetry of the modes which is well explained by the Fano theory [59]. The latter describes the coupling of the modes using the extinction line shape function:

$$f(\varepsilon) = (q + \varepsilon)^2/(1 + \varepsilon^2), \qquad \text{(Eq. 1)}$$

with $\varepsilon = 2(\omega - \omega_{vib})/\Gamma$, ω_{vib} corresponding to the resonance frequency of the vibrational excitation, q to the asymmetry parameter, and Γ to the vibrational linewidth. By using this lineshape, the fit of the experimental data has been performed by the group of Prof. Pucci, obtaining a characteristic asymmetry parameter q =-1.5, which accounts for the coupling and for the phase shift between the vibrational and the plasmonic mode.

In parallel, the SEIRA activity can be evaluated in terms of the enhancement factors (*EF*) with respect to the signal detected in IRRAS (V_{IRRAS}) from an ODT monolayer coating a gold surface under grazing angle illumination conditions (i.e. incidence angle $\alpha = 83°$) [19], as:

$$EF = \frac{V_{SEIRA}}{V_{IRRAS}} \cdot \frac{1}{C} \cdot \frac{2\sin^2(\alpha)}{\cos(\alpha)} \cdot (n_s + 1) , \qquad \text{(Eq. 2)}$$

where C is the area coverage of the Au nanoantennas on the surface and $n_s = 1.5$ is the refractive index of the substrate. Based on the SEM statistics we estimate $C \cong 15$ % by conservatively considering all the Au nanorods with length $L \geq 200$ nm as potentially active sites. However, it has been cleared out [27,29,35], that the measured SEIRA signal arises only from the molecules that are located at the hot spots of the nanoantennas, in correspondence to their ends. In order to improve our strong overestimate of the SEIRA active areas we evaluate the tips area by considering the 10 nm long apexes of each nanorods via SEM statistics (Figure 2d), corresponding to an effective surface coverage $C_{eff} \cong 0.6$ %. Under this assumption we obtain that the characteristic enhancement factor of the resonant nanorod antennas (sample A) reads $EF_{eff} \cong 55000$. We stress that this figure is competitive with the efficiency of lithographic nanoantenna arrays [60,61] even though EF_{eff} is underestimated since in the evaluation of C_{eff} we included all rods lengths, including those strongly detuned from the molecular resonance which can be considered as nearly inactive.

Hot spot density engineering

In order to further improve the nanorod arrays sensitivity for biosensing, the vibrational response of the ODT monolayer has been inspected on a second sample (sample B) where the density of active hot spot sites was increased by slightly reducing the ion fluence in the nanopatterning

process (SEM image in Fig. 5a). The detected vibrational signal is shown in Figure 5b. The SEM morphology and vibrational signal of Sample A are reported for comparison in Fig 5c,d respectively. In analogy to sample A, a strong vibrational response is detected (blue line in Fig. 4b) which is characterized by a Fano line-shape of the modes with asymmetry factor q = -1.3, which is very similar to the value obtained for sample A (i.e. q = -1.5). Indeed, the broadband nature of the plasmonic resonance allows to preserve the phase delay between the plasmonic excitation and the vibrational stretching modes, despite the slight change of the distribution of antennas length and/or shape. This is a remarkable feature that allows to exploit these large area templates to perform large area vibrational spectroscopy at constant phase delay. In parallel, sample B shows a further enhancement of all the vibrational modes, with the peak-to-peak amplitude of the CH_2 antisymmetric stretching as high as 5.7 %.

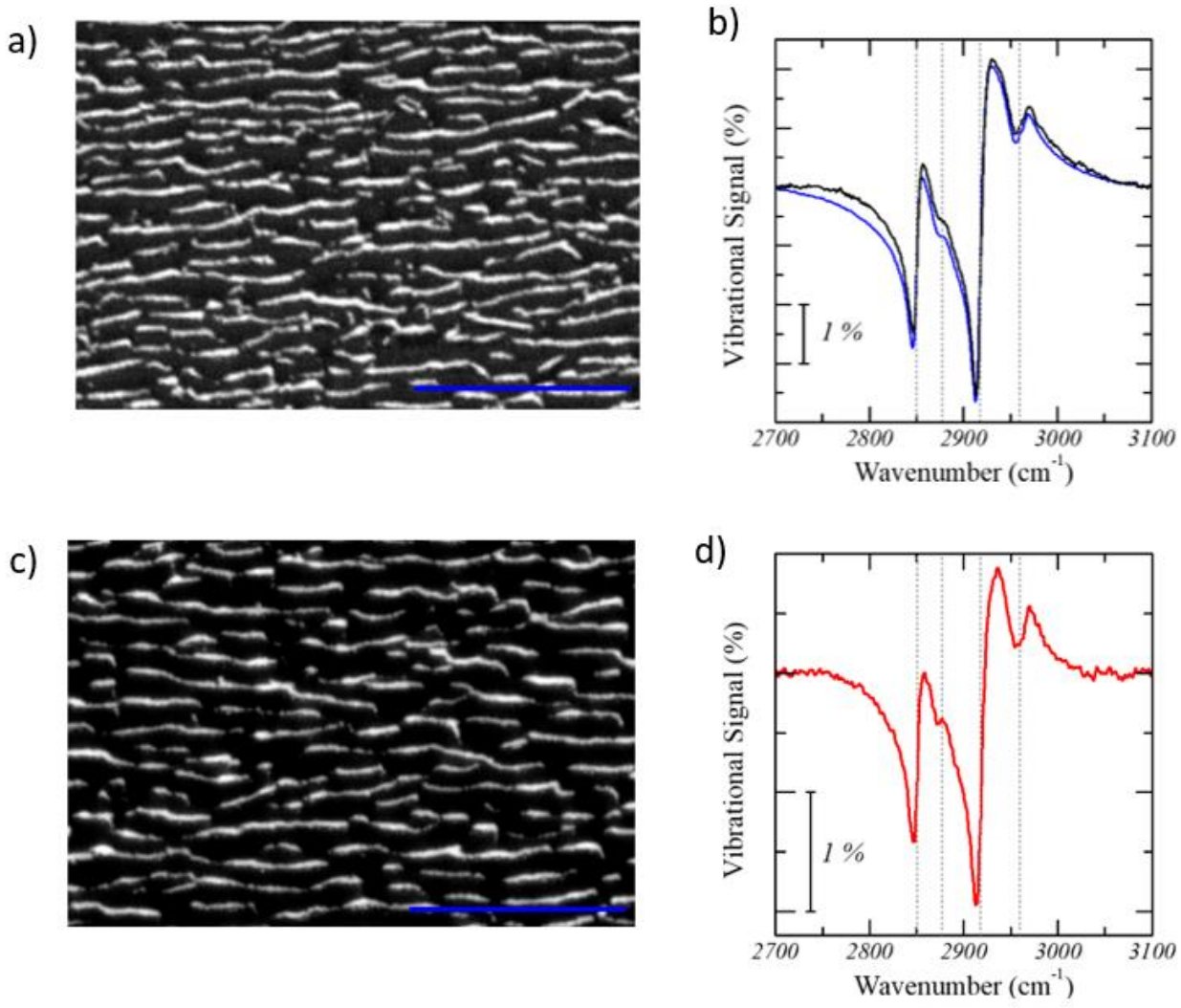

Figure 5 – *(a,c) SEM images acquired in the backscattered channel with a primary beam energy of 15 kV for sample B (a) and sample A (c) which are characterized by increasing density of active hot spots. The blue scale bars correspond to 1 μm. (b,d) Vibrational signal from the ODT monolayer for sample B (b) and sample A (d) . In panel b) the vibrational signal detected with the IR optical microscope (blue line – optical spot of 100 μm size) is compared with the signal detected with a standard IR spectrometer (black line - optical spot of 3 mm size).*

Since the density of antennas longer than 200 nm is here increased by 50 % with respect to sample A, we estimate for sample B an effective coverage corresponding to the active tip area $C_{eff} \cong 0.9\ \%$ and in turn to an enhancement factor $EF_{eff} \cong 75000$ which is further improved with respect to the case of lithographic nanoantenna arrays [60,61] and of sample A. This result highlights the importance of non-linear amplification of the vibrational signal when increasing the density of the active sites, which can be attributed to the strong near-field localization in nanoscale inter-antenna gaps.

The homogeneity of the detected vibrational enhancement over a macroscopic area has been also demonstrated by probing the molecular monolayer with a conventional large spot IR spectrometer (diameter of the optical spot of about 3 mm). The vibrational signal detected under large-area probing of the ODT monolayer (Fig. 5b - black curve), clearly shows full quantitative agreement with respect to the micro-spectroscopic measurement (Fig. 5b - blue curve), demonstrating the high degree of homogeneity of the plasmonic antennas arrays. This reproducible and stable SEIRA response, in parallel with the highly stable Fano line highlights the strong potential of these SO nanorod-antenna arrays for large-area amplitude and phase-sensitive IR spectroscopy and biosensing.

5.2 Conclusions

During my PhD program I worked on the cost-effective engineering of self-organized nanorod antennas featuring dichroic plasmonic functionalities in the Near- and Mid-IR spectral range. The exploitation of the novel SO nanopatterning approach combining ion induced wrinkling in glasses with glancing angle metal evaporation has been further developed for tailoring the morphology and the optical response of quasi-1D Au nanorod antennas supporting the selective excitation of a

broadband LSP resonance in the Near-IR for longitudinal polarization. This enables the highly sensitive detection of molecular monolayers active in the IR functional group window tuned with the low-frequency tail of the plasmonic resonance. Under this condition highly sensitive SEIRA spectroscopy has been performed on self-assembled monolayers of ODT molecules coating the plasmonic templates. The high density and efficiency of active hot-spots on the SO nanorod arrays allows to detect homogenous Fano lineshapes with amplitude reaching up to the 5.7 % and enhancement factors per antenna in the range of 10^4 - 10^5, demonstrating improved performances with respect to state of the art lithographic nanoantennas. Remarkably the broadband nature of the plasmonic resonance enables high stability of the Fano lineshape even on different samples, thus enabling large area amplitude- and phase-sensitive IR spectroscopy, multiplexed biosensing and cost-effective biomedical applications.

5.3 Experimental

Glass nanopatterning

Standard microscope glass slides (soda lime glass) are heated up to 685 K, near their glass transition temperature, and irradiated with a defocused ion source (Ar^+) of energy of 800 eV at the incidence angle θ=30° with respect to the normal direction to the surface. During the ion irradiation process the glass surface is kept electrically neutral by exploiting the thermoionic electron emission from a tungsten filament negatively biased with respect to the sample at V_{bias}=-13 V. Under this condition highly ordered faceted nanopatterns can be achieved if the ion irradiation is prolonged for 1800 s (i.e. ion fluence of $1.4x10^{19}$ ions/cm^2), as shown by the AFM topography of Figure 1a,b.

Sample preparation for SEIRA measurements

The Au nanorod arrays have been treated with oxygen plasma at 150 W at 0.4 mbar for 3 min to provide a clean gold surface for sulfur binding of the Octadecanthiol (ODT, $CH_3(CH_2)_{16}CH_2SH$) molecules. These procedures were performed by the group of Prof. Pucci in Heidelberg University. According to a literature recipe, the samples were exposed to a 1 mM solution of ODT (Sigma-Aldrich, purity: 98%) in ethanol for exactly 24 h [19,33]. Under this condition, the ODT/Au sulfur bonding promotes the formation of a SAM monolayer on top of the nanorod arrays. In order to

avoid unbound ODT on the surface, the samples were carefully rinsed afterwards and dried them with nitrogen gas. This procedure results in a uniform coating with a thickness of around 2.8 nm [33] of the IR active ODT which in principle is below the detection limit for an IR transmittance measurement [47]. To provide optimal measurement conditions, resulting in flat baselines, the references (glass substrates) were treated in the same way as the samples. By doing so, influences due to the solvent or the plasma cleaning procedure on the substrate cancel out in the measurements.

Microscopic and Standard IR-Spectroscopy

The optical response of the samples was investigated in the NUV–VIS range by my group in Genova using a compensated deuterium-halogen lamp (DH-2000-BAL, Mikropak) fiber-coupled to a linear polarizer and pinhole (with a diameter of 5 mm) acting also as a sample holder, placed at the focus of the optical beam. The polarization of the incoming light, incident on the back side of the sample, can be selected as parallel (TE-pol) or perpendicular (TM-pol) with respect to the Au NWs' long axis. A lens positioned at the opposite side of the sample, aligned with the illumination beam, focuses the radiation transmitted through the sample into a second optical fiber. Then, the signal is detected by a high-resolution solid-state spectrometer (HR4000 Ocean Optics) connected to a computer for the acquisition of the spectra. All spectra presented in this chapter were normalized to the optical transmittance of a bare glass substrate.

The microscopic IR measurements have been carried out by the group of Professor Pucci in Heidelberg by using a Bruker Hyperion 1000 IR microscope, coupled to a Bruker Tensor 27 FTIR spectrometer in transmittance geometry. A polarizer within the beam path allows to align the electric field component of the incoming IR radiation either along the nanorods' long axis (parallel) or perpendicular to it. In order to avoid disturbing absorptions of water vapor or carbon dioxide in the measurement, the whole beam path was purged with dry air. The signal was detected by using a mercury cadmium telluride (MCT) detector which was kept at liquid nitrogen (LN_2) temperature We used a spectral resolution of 2 cm^{-1} and an aperture size of 104.2 μm in diameter for the measurements. Each spectrum is averaged over several hundred scans in order to provide a high signal to noise ratio, allowing the careful analysis of the molecular ODT vibrational signature. In order to obtain only information from the gold nanorods, relative measurements were carried out,

which means that the measurements of the structured sample were referenced to the measurements of the reference glass substrate. IR spectroscopic measurements, using an aperture with a diameter of 3.0 mm, were done by using a Bruker IFS66v/S spectrometer in transmittance geometry. In this case, the whole beam path was evacuated to 5 mbar to avoid atmospheric distortions. For the measurements, a resolution of 2 cm^{-1} and either perpendicular or parallel polarized light were chosen. Several hundred scans were averaged in order to obtain a high signal to noise ratio, measured with an MCT detector, kept at LN_2 temperature. As already explained for the microscopic measurements, relative measurements have been carried out.

References

1. Stuart, B. *Infrared spectroscopy: fundamentals and applications*. (J. Wiley, 2004).

2. Iverson, N. M. *et al.* In vivo biosensing via tissue-localizable near-infrared-fluorescent single-walled carbon nanotubes. *Nature Nanotechnology* **8**, 873–880 (2013).

3. Åkerholm, M. & Salmén, L. Interactions between wood polymers studied by dynamic FT-IR spectroscopy. *Polymer* **42**, 963–969 (2001).

4. Baker, M. J. *et al.* Using Fourier transform IR spectroscopy to analyze biological materials. *Nature Protocols* **9**, 1771–1791 (2014).

5. Huber, A. J., Keilmann, F., Wittborn, J., Aizpurua, J. & Hillenbrand, R. Terahertz Near-Field Nanoscopy of Mobile Carriers in Single Semiconductor Nanodevices. *Nano Letters* **8**, 3766–3770 (2008).

6. Giliberti, V. *et al.* Heterogeneity of the Transmembrane Protein Conformation in Purple Membranes Identified by Infrared Nanospectroscopy. *Small* **13**, 1701181 (2017).

7. Brown, L. V. *et al.* Fan-Shaped Gold Nanoantennas above Reflective Substrates for Surface-Enhanced Infrared Absorption (SEIRA). *Nano Letters* **15**, 1272–1280 (2015).

8. Woessner, A. *et al.* Highly confined low-loss plasmons in graphene–boron nitride heterostructures. *Nature Materials* **14**, 421–425 (2015).

9. Lundeberg, M. B. *et al.* Thermoelectric detection and imaging of propagating graphene plasmons. *Nature Materials* **16**, 204–207 (2017).

10. Huber, M. A. *et al.* Femtosecond photo-switching of interface polaritons in black phosphorus heterostructures. *Nature Nanotechnology* **12**, 207–211 (2017).

11. Giordano, M. C. *et al.* Phase-resolved terahertz self-detection near-field microscopy. *Optics Express* **26**, 18423 (2018).

12. Eisele, M. *et al.* Ultrafast multi-terahertz nano-spectroscopy with sub-cycle temporal resolution. *Nature Photonics* **8**, 841–845 (2014).

13. Griffiths, P. R. & De Haseth, J. A. *Fourier transform infrared spectrometry*. (Wiley-Interscience, 2007).

14. Pryce, I. M., Kelaita, Y. A., Aydin, K. & Atwater, H. A. Compliant Metamaterials for Resonantly Enhanced Infrared Absorption Spectroscopy and Refractive Index Sensing. *ACS Nano* **5**, 8167–8174 (2011).

15. Shankar, S. S. *et al.* Biological synthesis of triangular gold nanoprisms. *Nature Materials* **3**, 482–488 (2004).

16. Li, D., Müller, M. B., Gilje, S., Kaner, R. B. & Wallace, G. G. Processable aqueous dispersions of graphene nanosheets. *Nature Nanotechnology* **3**, 101–105 (2008).

17. Yang, H., Yang, S., Kong, J., Dong, A. & Yu, S. Obtaining information about protein secondary structures in aqueous solution using Fourier transform IR spectroscopy. *Nature Protocols* **10**, 382–396 (2015).

18. Hoffmann, F. Infrared reflection-absorption spectroscopy of adsorbed molecules. *Surface Science Reports* **3**, 107 (1983).

19. Enders, D. & Pucci, A. Surface enhanced infrared absorption of octadecanethiol on wet-chemically prepared Au nanoparticle films. *Applied Physics Letters* **88**, 184104 (2006).

20. Maier, S. A. *Plasmonics: Fundamentals and Applications*. (Springer US, 2007). doi:10.1007/0-387-37825-1.

21. Ciraci, C. *et al.* Probing the Ultimate Limits of Plasmonic Enhancement. *Science* **337**, 1072–1074 (2012).

22. D'Andrea, C. *et al.* Optical Nanoantennas for Multiband Surface-Enhanced Infrared and Raman Spectroscopy. *ACS Nano* **7**, 3522–3531 (2013).

23. Bisio, F. *et al.* Plasmonics in Self-Organized Media. in *Encyclopedia of Nanotechnology* (ed. Bhushan, B.) 1–17 (Springer Netherlands, 2015). doi:10.1007/978-94-007-6178-0_100979-1.

24. Giordano, M. C. *et al.* SERS Amplification from Self-Organized Arrays of Plasmonic Nanocrescents. *ACS Applied Materials & Interfaces* **8**, 6629–6638 (2016).

25. Magnozzi, M., Ferrera, M., Mattera, L., Canepa, M. & Bisio, F. Plasmonics of Au nanoparticles in a hot thermodynamic bath. *Nanoscale* **11**, 1140–1146 (2019).

26. Fleischman, D. *et al.* High Spectral Resolution Plasmonic Color Filters with Subwavelength Dimensions. *ACS Photonics* **6**, 332–338 (2019).

27. Neubrech, F. *et al.* Resonant Plasmonic and Vibrational Coupling in a Tailored Nanoantenna for Infrared Detection. *Physical Review Letters* **101**, (2008).

28. Wu, C. *et al.* Fano-resonant asymmetric metamaterials for ultrasensitive spectroscopy and identification of molecular monolayers. *Nature Materials* **11**, 69–75 (2012).

29. Neubrech, F. *et al.* Spatial Extent of Plasmonic Enhancement of Vibrational Signals in the Infrared. *ACS Nano* **8**, 6250–6258 (2014).

30. Rodrigo, D. *et al.* Mid-infrared plasmonic biosensing with graphene. *Science* **349**, 165–168 (2015).

31. Dong, L. *et al.* Nanogapped Au Antennas for Ultrasensitive Surface-Enhanced Infrared Absorption Spectroscopy. *Nano Letters* **17**, 5768–5774 (2017).

32. Adato, R. & Altug, H. In-situ ultra-sensitive infrared absorption spectroscopy of biomolecule interactions in real time with plasmonic nanoantennas. *Nature Communications* **4**, (2013).

33. Huck, C. *et al.* Gold Nanoantennas on a Pedestal for Plasmonic Enhancement in the Infrared. *ACS Photonics* **2**, 497–505 (2015).

34. Neubrech, F., Huck, C., Weber, K., Pucci, A. & Giessen, H. Surface-Enhanced Infrared Spectroscopy Using Resonant Nanoantennas. *Chemical Reviews* **117**, 5110–5145 (2017).

35. Huck, C. *et al.* Surface-Enhanced Infrared Spectroscopy Using Nanometer-Sized Gaps. *ACS Nano* **8**, 4908–4914 (2014).

36. Koppens, F. H. L. *et al.* Photodetectors based on graphene, other two-dimensional materials and hybrid systems. *Nature Nanotechnology* **9**, 780–793 (2014).

37. Giordano, M. C., Viti, L., Mitrofanov, O. & Vitiello, M. S. Phase-sensitive terahertz imaging using room-temperature near-field nanodetectors. *Optica* **5**, 651 (2018).

38. Brar, V. W., Jang, M. S., Sherrott, M., Lopez, J. J. & Atwater, H. A. Highly Confined Tunable Mid-Infrared Plasmonics in Graphene Nanoresonators. *Nano Letters* **13**, 2541–2547 (2013).

39. Aćimović, S. S. *et al.* LSPR Chip for Parallel, Rapid, and Sensitive Detection of Cancer Markers in Serum. *Nano Letters* **14**, 2636–2641 (2014).

40. Yavas, O. *et al.* Self-Calibrating On-Chip Localized Surface Plasmon Resonance Sensing for Quantitative and Multiplexed Detection of Cancer Markers in Human Serum. *ACS Sensors* **3**, 1376–1384 (2018).

41. Proietti Zaccaria, R. *et al.* Plasmonic Color-Graded Nanosystems with Achromatic Subwavelength Architectures for Light Filtering and Advanced SERS Detection. *ACS Applied Materials & Interfaces* **8**, 8024–8031 (2016).

42. Repetto, D. *et al.* SERS amplification by ultra-dense plasmonic arrays on self-organized PDMS templates. *Applied Surface Science* **446**, 83–91 (2018).

43. Barelli, M., Repetto, D. & de Mongeot, F. B. Infrared Plasmonics via Self-Organized Anisotropic Wrinkling of Au/PDMS Nanoarrays. *ACS Applied Polymer Materials* **1**, 1334–1340 (2019).

44. Frank, B. *et al.* Large-Area 3D Chiral Plasmonic Structures. *ACS Nano* **7**, 6321–6329 (2013).

45. You, A. Y. F. *et al.* Raman spectroscopy imaging reveals interplay between atherosclerosis and medial calcification in the human aorta. *Science Advances* **3**, e1701156 (2017).

46. Albro, M. B. *et al.* Raman spectroscopic imaging for quantification of depth-dependent and local heterogeneities in native and engineered cartilage. *npj Regenerative Medicine* **3**, (2018).

47. Enders, D., Rupp, S., Küller, A. & Pucci, A. Surface enhanced infrared absorption on Au nanoparticle films deposited on SiO2/Si for optical biosensing: Detection of the antibody–antigen reaction. *Surface Science* **600**, L305–L308 (2006).

48. Cataldo, S. *et al.* Hole-Mask Colloidal Nanolithography for Large-Area Low-Cost Metamaterials and Antenna-Assisted Surface-Enhanced Infrared Absorption Substrates. *ACS Nano* **6**, 979–985 (2012).

49. M. C. Giordano, M. Tzschoppe, M. Barelli, J. Vogt, C. Huck, F. Canepa, A. Pucci, F. Buatier de Mongeot, Self-Organized Nanorod Arrays for Large-Area Surface Enhanced Infra-Red Absorption. *Accepted by ACS Applied Materials & Interfaces*

50. Aas, L. M. S. *et al.* Optical properties of biaxial nanopatterned gold plasmonic nanowired grid polarizer. *Optics Express* **21**, 30918 (2013).

51. Della Valle, G. *et al.* Self-organized plasmonic metasurfaces for all-optical modulation. *Physical Review B* **91**, (2015).

52. Basiri, A. *et al.* Nature-inspired chiral metasurfaces for circular polarization detection and full-Stokes polarimetric measurements. *Light: Science & Applications* **8**, (2019).

53. Yu, N. & Capasso, F. Flat optics with designer metasurfaces. *Nature Materials* **13**, 139–150 (2014).

54. Peinado, A. *et al.* IR-Mueller matrix ellipsometry of self-assembled nanopatterned gold grid polarizer. *Applied Surface Science* **421**, 728–737 (2017).

55. Giordano, M. C. & de Mongeot, F. B. Anisotropic Nanoscale Wrinkling in Solid-State

Substrates. *Advanced Materials* **30**, 1801840 (2018).

56. Weber, D. *et al.* Longitudinal and transverse coupling in infrared gold nanoantenna arrays: long range versus short range interaction regimes. *Optics Express* **19**, 15047 (2011).

57. Adato, R., Aksu, S. & Altug, H. Engineering mid-infrared nanoantennas for surface enhanced infrared absorption spectroscopy. *Materials Today* **18**, 436–446 (2015).

58. Guo, Z. *et al.* On the chain length dependence of CH3 vibrational mode relative intensities in sum frequency generation spectra of self assembled alkanethiols. *Surface Science* **602**, 3551–3559 (2008).

59. Fano, U. Effects of Configuration Interaction on Intensities and Phase Shifts. *Physical Review* **124**, 1866–1878 (1961).

60. Vogt, J. *et al.* Impact of the plasmonic near- and far-field resonance-energy shift on the enhancement of infrared vibrational signals. *Physical Chemistry Chemical Physics* **17**, 21169–21175 (2015).

61. Tzschoppe, M., Huck, C., Vogt, J., Neubrech, F. & Pucci, A. Impact of Metal-Optical Properties on Surface-Enhanced Infrared Absorption. *The Journal of Physical Chemistry C* **122**, 15678–15687 (2018).

CHAPTER 6

Large area blazed nanogratings for unidirectional Surface Plasmon Polariton excitation and SERS detection

Introduction

Surface plasmons polaritons (SPP) are electromagnetic modes propagating at the interface between a conductive and an insulating material due to resonant oscillations of conduction electrons plasmas. Their propagating nature makes them interesting for waveguiding applications, which are not enabled by Localized Surface Plasmons (LSP) [[1–3] and references therein]. SPP modes can be excited by photons under selected conditions, thus confining their energy in subwavelength volumes at the interface producing an electric field enhancement which esponentially decays away from it. This property makes these optical mode intertesting for enhanced spectroscopies such as Surface Enhanced Raman Spectroscopy (SERS) and Plasmon Enhanced Fluorescence (PEF) [[4–8]]. The sensitivity of the SPP resonance to the refractive index of the sorrounding dielectric medium enables optical refractive index sensor devices, already employed in commercial applications [[9]]. However, photon-SPP coupling is not possible by direct illumination, as already discussed in depth in section 1.3.2 of this thesis, and particoular strategies have to be adopted [[2,3]]. One of these strategies consists in using diffraction gratings at the metal/dielectric interface to modulate the incoming photons wavevector to couple them to the SPP one thus allowing the mode excitation [[5,7,8,10–12]].

In this chapter I demonstrate how the self-organized rippled soda-lime glass templates, prepared by the innovative wrinkling-enhanced Ion Beam Sputtering (IBS) method described in the previous chapters (and in detail in section 1.2.3 [[13]]), can operate as large area, subwavelenght, quasi-1D blazed grating enabling the unidirectional excitation of propagating Surface Plasmon Polariton modes at the interface with thin conductive films conformally grown on top, in IMI (insulator-metal-insulator) configuration [16]. Such a sample is tested in SERS measurements for detection of methylene blue molecules. I demonstrate how the SERS gain is strongly correlated with the electric field enhancement produced by the excitation of SPP modes by comparing SERS

and co-localized micro-extinction measurements. It will be shown how the large area self-organized SPP launching platform is very versatile as simply chosing the conductive material to grow of top of the rippled glass template allows the tailoring of the plasmonic response in a wide spectral range, going from the near UV to the near IR, and possibly beyond considering semiconductive materials. This makes these semi-transparent, large area, self-organized plasmonic systems interesting for a broad range optoelectronic applications.

6.1 Results and discussion

Fabrication of the rippled Au/soda-lime gratings

The nanorippled soda-lime glass template, described in section 1.2.3 and chapter 3, 4 and 5 of this thesis, fabricated by hot IBS, has been prepared for SPP plasmonic functionalization. A soda-lime glass sample (20 × 20 × 1 mm) is irradiated with a defocused Ar^+ iom beam at a low energy of 800 eV and at $\theta = 30°$ incident angle with respect to the sample surface normal. The resulting quasi 1-D ripped pattern with wavevector parallel to the ion beam direction (Fig. 1a) is characterized by a steep asymmetric sawtooth profile, with a pronounced ripples vertical dynamic of about 80 nm (Fig. 1b) and periodicity of around 200 nm [13]. The ripples periodicity is assessed by the 2D self-correlation function of AFM images obtained by means of the WSxM software (Fig. 1d), by calculating the distance between the self-correlation function maximum and the first neighboring peak along the line profile of Fig. 1e. As discussed in the previous chapters of the thesis, the ridges directly exposed to the ion beam develop a broad facet slope distribution peaked at about -50°. On the contrary, the ridges opposed to the ion beam develop wider facets with a narrow slope distribution peaked at +35° (see section 1.2.3). The ripples profile in asimmetric and thus the nanostructured glass surface can be considered as self-organized (SO), quasi 1D, blazed (or slanted) subwavelentgh diffraction grating.

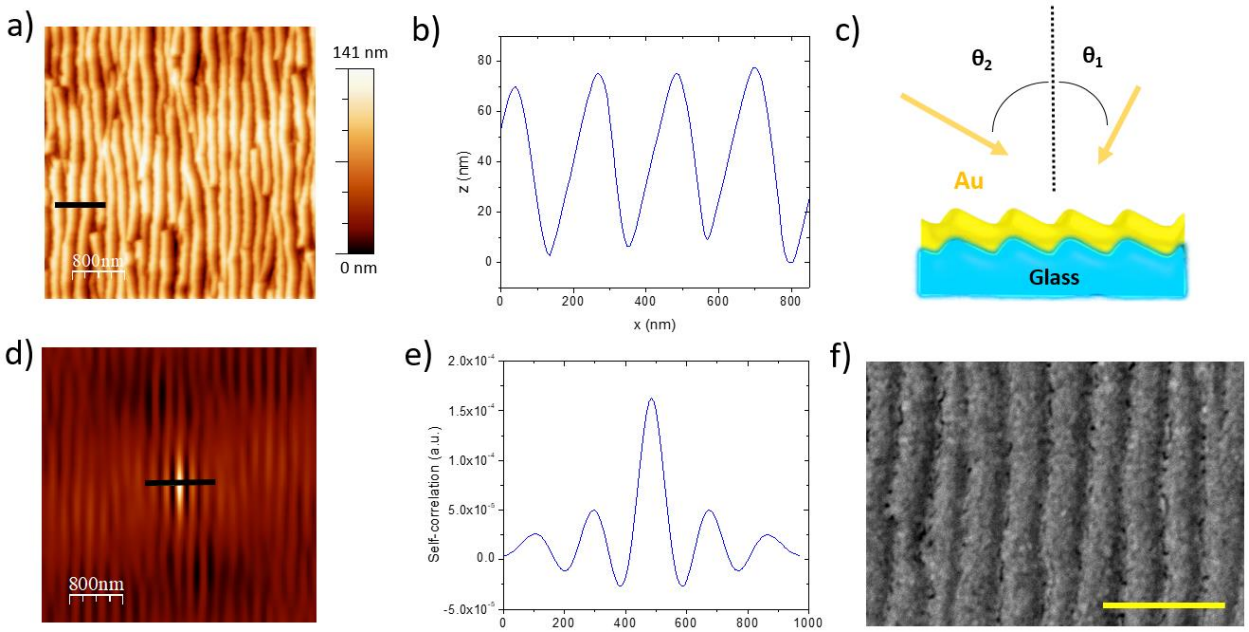

Figure 1: *a) AFM topography of the rippled glass surface. b) AFM line profile corresponding to the black bar in panel a). c) Cross section sketch of the two step Au deposition process on the asymmetric sawtooth rippled profile of the soda-lime glass surface. d) 2D self-correlation function of the AFM image of panel a). e) Self-correlation function line profile corresponding to the black bar in panel d). f) Top view SEM of the Au covered rippled surface, acquired in the backscattered electrons channel, with acceleration voltage of 15kV. The yellow bar corresponds to 500 nm.*

Au is then deposited on the rippled glass template by grazing angle thermal deposition. To grow a uniform thin Au film on the asymmetric rippled surface, the deposition is performed in two steps. The first deposition step is performed at the angle θ_1=15° with respect to the sample surface normal, over the right side of the ripple profile (Fig. 1c). In this condition the Au beam forms a 20° angle with respect to the local surface normal of the "wide" facets. At the same time an angle of 65° is formed between the Au beam and the local surface normal of the "steep" facets. Thus during the first deposition step the Au thickness deposited on the left side of the ripple can be estimated as $h_{\text{left-1}}=h_0 \times \cos 20°$, while on the right side the thickness is $h_{\text{right-1}}=h_0 \times \cos 20°$, where h_0 is the equivalent Au thickness on a flat substrate. During the experiment h_0 is the parameter which gets actually measured by means of a quartz microbalance. The second Au deposition step is performed at the angle θ_2=30° with respect to the sample normal over the left side of the ripple profile (Fig. 1c). Now the Au beam forms a 20° angle with respect to the "steep" facets and a 65° angle with respect to the "wide" facets local surface normals; the situation is now opposite

compared to θ_1 conditions and $h_{\text{left-2}}=h_0 \times \cos 65°$ while $h_{\text{right-2}}=h_0 \times \cos 20°$. To grow an approximately uniform Au layer over the asymmetric slope modulate ripple profile it's sufficient to impose a desired thickness h and solve one of the following equations for h_0:

$$\begin{cases} h_{\text{left}-1} + h_{\text{left}-2} = h_0 \times \cos 20° + h_0 \times \cos 65° = h \\ h_{\text{right}-1} + h_{\text{right}-2} = h_0 \times \cos 65° + h_0 \times \cos 20° = h \end{cases}$$

In this way a thin film of Au with thickness h=25 nm was conformally grown on the rippled glass surface. The top-view Scanning Electron Microscopy (SEM) image in Fig. 1e shows how gold covers the sample surface. At this point the rippled Au film/soda-lime glass template can be considered as a IMI (insulator-metal-insulator) SO blazed diffraction grating where the rippled modulations constitute the quasi-1D grating grooves.

SPP shift with grating periodicity

The coupling of light with SPPs at the metal/dielectric interfaces is enabled by the grating-mediated momentum transfer of incoming photons, required for the plasmonic excitation to take place (see section 1.3.2 of this thesis for theoretical insight and Refs. [2,3]).

Such possibility is investigated by normal incidence linearly polarized optical transmission measurements (Fig. 2a).

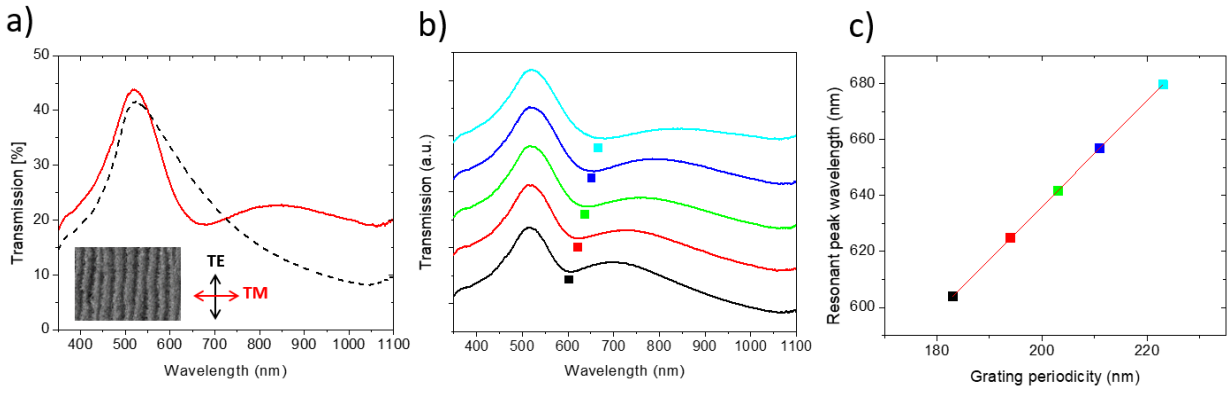

Figure 2: *a) Normal incidence transmission measurements of a function of polarization. TM polarization corresponds to the continuous red curve, while TE polarization corresponds to the black dashed curve, as sketched in the panel inset. b) TM normal incidence transmission spectra acquired for different periodicity of the Au/soda-lime blazed grating; 183 nm (black curve), 194*

nm (red curve), 203 nm (green curve), 211 nm (blue curve), 223 nm (cyan curve). c) Plot of resonant wavelength vs. the grating periodicity.

For TE polarization (Fig. 2a, dotted black curve) the electric field oscillates parallel to the diffraction grating grooves (ripples long axis); in the considered spectral range, the sample transmission curve resembles the one of a Au flat thin film, similarly to what we observed in the case of disconnected Au nanowire (NW) arrays on rippled polydimethylsiloxane (chapter 2) and rippled soda-lime glass (chapter 3). For TM polarization (Fig. 2a – continuous red curve) the electric field oscillates orthogonally to the diffraction grating grooves (ripples short axis) and a strong dichroism is observed as transmission shows a broad minimum centered at the wavelength λ of about 660 nm. At variance with the case of disconnected NWs, the transmission minimum for TM polarization cannot be associated with the excitation of a Localized Surface Plasmon resonance (LSP – see section 1.3.1) because in this case the Au layer forms a continuous conformal coating; the transmission dip is instead attributed to the excitation of a propagating SPP along the continuous thin rippled Au film, enabled by the momentum exchange generated by the photon-grating interaction. To further investigate the phenomenon, we can exploit a natural feature of our hot IBS fabrication process which leads to the formation of SO glass templates with a periodicity gradient due to a slightly different ionic dose at different sample locations. Indeed, the IBS irradiation is performed at non-normal incidence and this creates a slight modulation of ion dose over the sample length along the ion beam incident direction, because of different point to point distance from the ion source: considering a periodicity Λ=200 nm in the central area of the glass template (Fig. 1a) we can get a grating periodicity modulation of about ±15% moving from the top to the bottom of the sample along the projection of the ion beam. In Fig. 2b we show TM transmission spectra acquired at different samples coordinates and we associate to each spectra a different grating periodicity at the optical spot, evaluated by means of AFM microscopy. In Fig. 2c the transmission dip minimum of each curve is plotted against the corresponding grating periodicity. The SPP resonant wavelength (transmission minimum) redshifts linearly and monotonically starting from the smaller considered periodicity (Λ=183 nm – black curve in Fig. 2b) to the bigger one (Λ=230 nm – cyan curve in Fig. 2b). As the grating periodicity gets bigger a smaller momentum, defined by $k_G = n\frac{2\pi}{\Lambda}$, is exchanged in the photon-grating interaction where n is an integer number either positive or negative. A monotonic redshift of SPP resonance is thus

expected with increasing grating periodicity.

SPP shift with light beam angle of incidence

To further investigate and strengthen the attribution of the observed optical mode to a SPP mode, I performed transmission measurements as a function of the sample tilt relative to the light beam. The sample is illuminated from the glass side and the signal is coaxially collected in extinction configuration. The sample is tilted forming an angle θ between the incident light beam and the surface normal (Fig. 3a). The sample rotation is performed counter-clockwise, that is reducing the angle formed by the incident light beam and the local surface normal of the wide facets of the rippled Au/glass template (Fig. 3a). In Fig. 3b transmission spectra are plotted for different sample tilts.

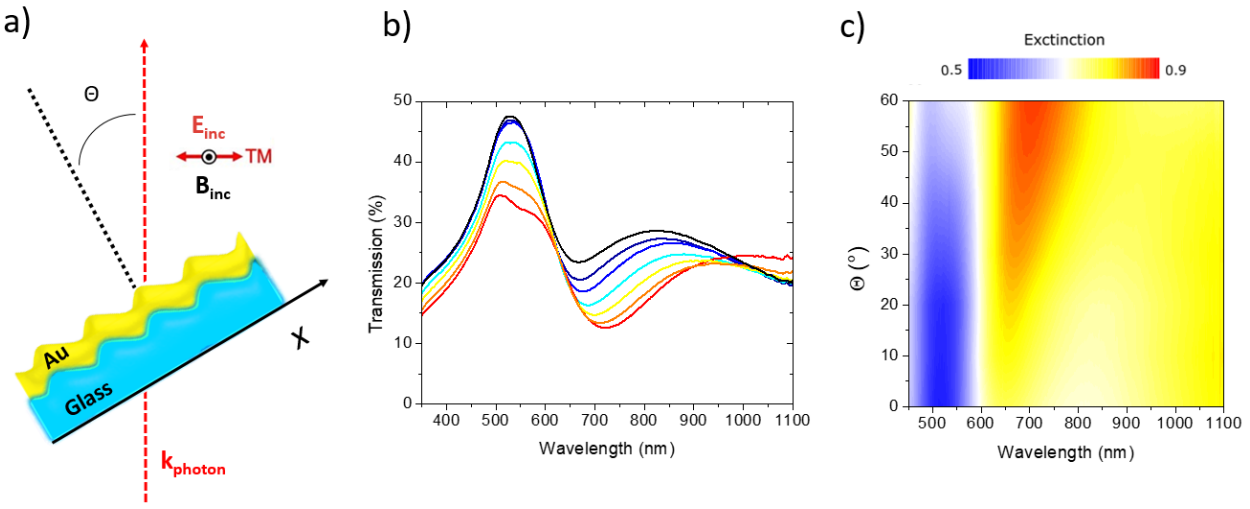

Figure 3: *a) Sketch of the tilted transmission (T) measurements configuration. The red arrow* k_{photon} *represents the light beam incoming from the glass side. Θ is the angle formed between the light beam and the normal to the flat sample surface. The x arrow defines the axis along the metal dielectric interfaces. In the inset the direction of oscillation of the incoming electric field* E_{inc} *(red arrow) and the out of plane magnetic field* B_{inc} *(black dot) are represented. b) TM transmission measurements as a function of Θ; 0° (black curve), 10° (royal blue curve), 20° (blue curve), 30° (cyan curve), 40° (yellow curve), 50° (orange curve), 60° (red curve). c) Extinction maps (calculated from the transmission spectra as* $\frac{1-T(\%)}{100}$*) as a function of both wavelenght and tilt angle Θ.*

The transmission dips redshift monotonically with sample tilt, confirming the propagating nature of the observed optical mode. For the highest tilt θ=60° (red curve in Fig. 3b) an additional, weak relative transmission minimum is observed at about λ=540 nm. In Fig. 3c the wavelenght dependent extinction map (computed as $\frac{1-T(\%)}{100}$) is plotted against both wavelenght λ and sample tilt θ. The non-dispersive blueish extinciton band centered at about 530 nm is clearly associated with the spectral edge at the onset of Au interband transitions, while the strong and dispersive red band describes the SPP mode which intensifies and broadens with increasing sample tilt.

The monotonic redshift of the SPP resonance with increasing sample tilt (i.e. with increasing projection of photon wavevector k_{ph} in the positive x-direction) suggests the counter-propagating nature of the SPP mode with respect to the incident light beam direction. This trend can be reconciled considering that the grating allows to exchange momentum $k_G = n\frac{2\pi}{\Lambda}$ in discrete units and the effective wavector component k_x along the *x* axis can be derived according to the well-known relation (Eq. 40 in section 1.3.2 of this thesis): $k_x = |k_{ph}| \sin\theta + n\frac{2\pi}{\Lambda}$ where k_{ph} is the modulus of photon wavevector, θ is the angle formed by the light beam with the normal to the flat sample surface (Fig. 3a), λ is the periodicity of the Au/soda-lime grating in the region of the optical spot and n is an integer number, either positive or negative. In particular, given the wavevector of the photon in correspondence to the SPP mode and the periodicity Λ of the grating, one observes that for negative n values k_x decreases for increasing values of θ.

Comparison of the experimental data with a simple effective medium model

In order to achieve a qualitative comparison of the observed trends in Fig. 4 we plot the SPP dispersion relations derived for a thick flat Au slab using the conventional expression $k_{SPP} = \frac{\omega}{c}\sqrt{\frac{\varepsilon_1\varepsilon_2}{\varepsilon_1+\varepsilon_2}}$ where ε_1 is the real part of Au the dielectric functions and ε_2 is the one of the dielectric layer facing the Au slab. The SPP branch corresponds to the counter-propagation of the SPP at Au-dielectric interface with effective refractive index n_i=2.4 – light blue line (the dashed line is the dispersion relation of light in the dielectric medium). The experimental SPP points, associated to the transmission dips of Fig. 3b, are plotted in terms of $k_x = |k_{ph}| \sin\theta + n\frac{2\pi}{\Lambda}$ assuming n=-1, i.e. incoming photons with positive momentum k_x couple with a SPP with negative k_x, via exchange

of grating coupled negative momentum $k_{G,-1} = -\frac{2\pi}{\Lambda}$.

I stress that the qualitative comparison of Fig. 4 is just intended show the general trend of SPP dispersion since one should take into account that the Au film is so thin (t=25 nm) that coupling between plasmon polaritons propagating at the two interfaces of the slab cannot be neglected. A quantitative analysis of our data following such approach goes beyond the scopes of my work but it is nevertheless possible to derive some useful hints by comparing with results derived for Ag films [14,15]. In these examples significant coupling and hybridization of the SPP modes occurs for Ag film thickness below 91 nm. In particular one observes that the antisymmetric SPP mode (termed Long-Range SPP) increasingly redshifts form the normal SPP branch when film thickness decreases (see e.g. Fig. 3 of ref. [14]). Additional features which must be considered in explaining the experimental redshift of the SPP energy are related to the fact that the real metal interface is corrugated at both sides while the SPP dispersion relation refers to and ideal flat film.

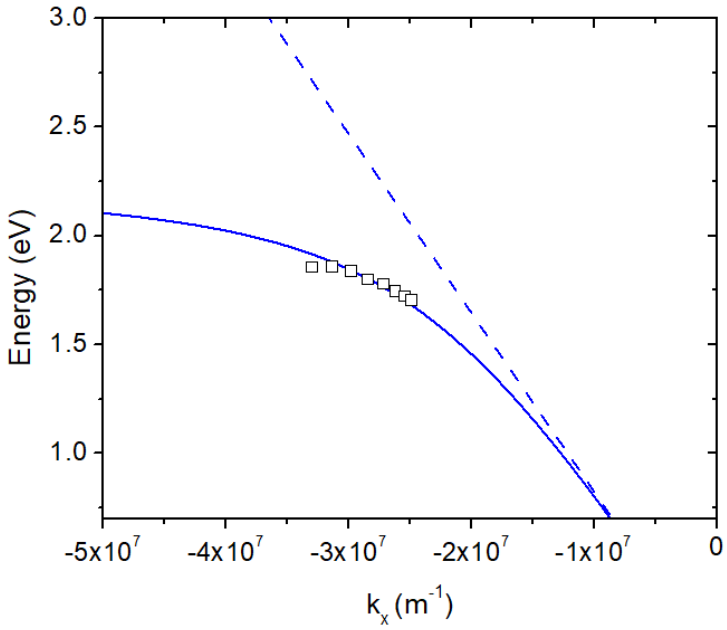

Figure 4: *Dispersion relation of a SPP propagating at the Au/dielectric interface (solid blue curve) and light line of a photon travelling in the dielectric medium (dashed blue curve). Experimental data is plotted as squares.*

SERS measurements

As well as for localized plasmon resonances confined at nanoparticles, also near the interface of a

metal supporting an SPP one can experience enhancement of the electric field confined in the vertical direction (see section 1.3.2). With this in mind we recurred to SERS/micro-extinction measurements in order to probe the SPP near field enhancement on the rippled Au/soda-lime blazed grating. For this purpose, I was hosted by the laboratories of Consiglio Nazionale delle Ricerche – Istituto per i processi Fisico-Chimici (CNR-IPCF) in Messina, Italy) under the supervision of Prof. Pietro Giuseppe Gucciardi to perform such experiments. The sample is kept in a methylene blue (MB) 10^{-4} M solution for an hour and then rinsed in de-ionized water for 10 minutes. SERS measurement are then performed with polarized pump lasers of both 638 and 785 nm of wavelentgh in TM configuration, using a 100x objective, at different sample coordinates. Co-localized optical micro-extinction measurements are contextually performed at the same coordinates by simply switching to a 10x objective for collection and to a polychromatic lamp source, illuminating the sample from the glass side in TM polarization. SERS signal of MB is then measured under equivalent conditions on a flat Au film with a thickness of 150 nm, to be used as reference. To compute the SERS gain of the rippled Au grating at the different sample coordinates, we selected the characteristic MB Raman peak at 1625 cm^{-1} integrating the total counts under the peak and dividing by the integrated counts of the same MB peak measured on the reference flat Au film, paying attention to normalize the result to the same laser power and integration time. The so defined SERS gain, plotted as a function of the sample coordinates for the 638 and 785 nm pump lasers, shows a monotonic increasing trend as reported in Fig. 5a and Fig. 5b respectively.

As previously discussed, the SPP resonance spectrally shifts when moving at different sample coordinates due to a spatial dependence of the SO grating periodicity (Fig. 2b). It's thus possible to nicely correlate the intensity of the plasmonic extinction strength at the pump lasers frequency, which is responsible for the SERS near field enhancement, with the co-localized SERS gains. After background subtraction the extinction values at the pump lasers wavelenghts of 638 nm and 785 nm are then plotted as a function of sample position in Fig. 5c and Fig. 5d, respectively. Remarkably, the intensity of TM extinction and of the co-localized SERS gain are very strongly correlated for both pump laser wavelengths as a function of sample coordinates thus confirming that the observed SERS signal is indeed matched with the strength of the SPP induced electric near field enhancement at the SO rippled Au/soda-lime blazed grating.

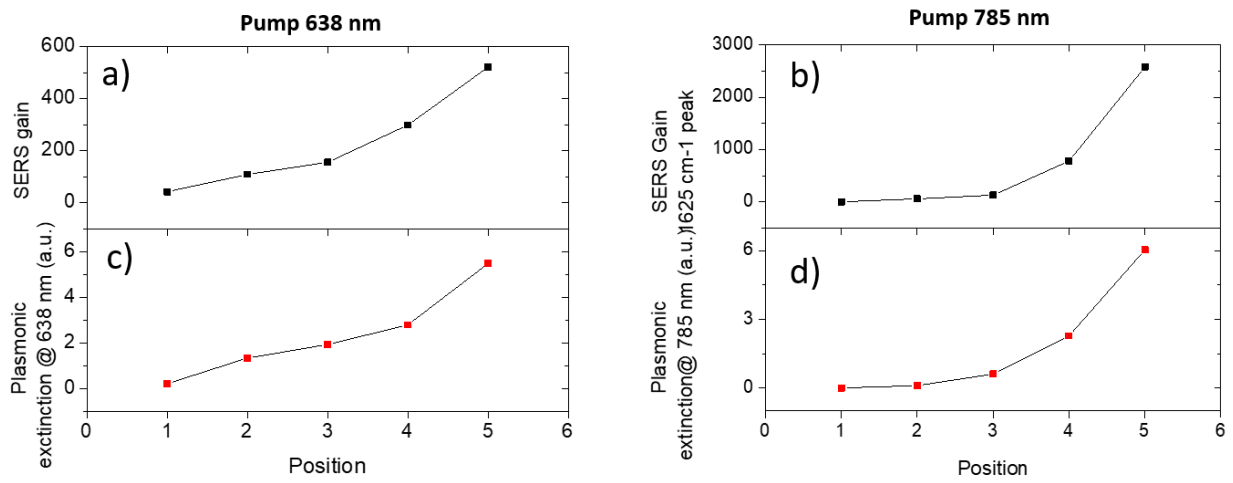

Figure 5 *– a,b) SERS gain of MB molecules signal with 638 and 785 nm pump lasers, respectively, in different sample coordinates. c,d) Plasmonic extinction values at 638 and 785 nm, respectively, as a function of sample coordinates, derived from Raman co-localized transmission measurements.*

It must be noticed that when using the pump laser at 638 nm one also excites an electronic transition in MB molecules. This is known to greatly enhance the cross section of Raman emission already on the flat Au film, so that Surface Enhanced Resonant Raman Spectroscopy (SERRS) is actually achieved an indeed the maximum reported SERRS gain for MB with the 638 nm laser turns out to be relatively small, in the order of 10^2. On the other hand, when using the pump laser at 785 nm excitation is non-resonant with the MB electronic transitions and conventional SERS is performed: in this case the maximum gain turns out to be in the order of $3x10^3$, a substantial figure which compares well with SERS substrates exploiting localized plasmon resonances at disconnected nanoparticles. We can thus consider the present observations of relevance in view of bio-sensing applications since it is possible to reduce the NIR laser pump power (and in turn, reduce sample damage and fluoresce background) while still keeping relevant the SERS gain in the near infrared range of the spectrum.

We can easily demonstrate the tunability and generality of our large-area, self-organized SPP launching platform by growing a thin film of another conductive material, silver instead of gold, on top of the glass rippled template. The thickness of the Ag film is kept at 25 nm as in the Au case. Optical transmission measurements with polarized light at normal incidence are reported in Fig. 6 for a grating wavelength of about 180 nm.

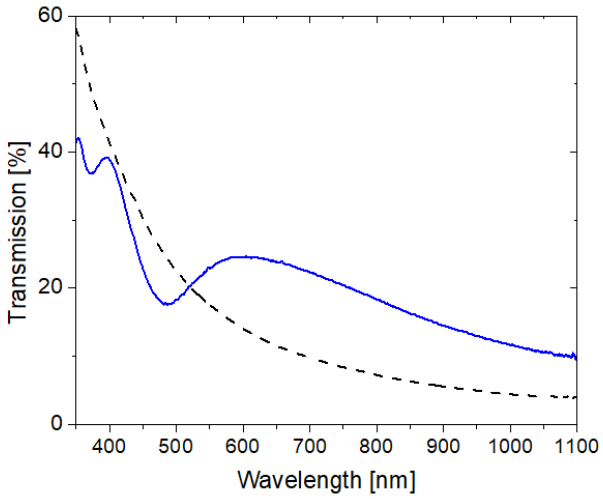

Figure 6 - *Normal incidence transmission measurements of a function of polarization for the rippled Ag/soda-lime glass SO blazed grating. The solid blue curve corresponds to TM polarization while the black dashed curve to TE polarization.*

For TE polization (electric field parallel to the grating grooves - black dashed curve in Fig.6) we can again observe the typical behaviour of an Ag thin film, with the onset of interband transition blueshifted with respect to the Au case (Fig. 2a), out of the measured spectral range. For TM polarization (electric field orthogonal to the grating grooves – blue solid curve in Fig. 6) we observe the excitation of an SPP associated with the transmission dip centered at about 490 nm. It is worth to note that in the Au case, for a similar grating periodicity of about 180 nm, the SPP resonance is found at 603 nm (black curve in Fig. 2b). By replacing Au with Ag a blueshift of almost 110 nm of the SPP resonance is obtained, due to the higher plasma frequency of silver compared to gold, keeping all the other morphological parameters fixed. This demonstrates the wide tunability of the plasmonic properties of our SO rippled thin metal film/soda-lime gratings in the near UV and visible range of the spectrum by simply choosing a metal with a higher electron density. Following a similar approach one could imagine shifting the SPP excitation in the NIR-IR range by growing on top of the rippled dielectric template a thin film with a reduced free carrier density like e.g. in the case of semiconductors with variable doping.

6.2 Conclusions

In this chapter I demonstrated how self-organized rippled soda-lime glass templates, prepared by an innovative hot Ion Beam Sputtering method, can operate as large area, subwavelenght, quasi-1D blazed gratings enabling the excitation of propagating Surface Plasmon Polariton modes at the interface with thin conductive films (Au and Ag) conformally grown on top of them. A rippled Au/soda-lime grating sample showed remarkable SERS activity in the detection of methylene blue molecules. I demonstrated how the SERS gain is strongly correlated with the electric field enhancement produced by the excitation of counter-propagating SPP modes by comparing SERS and co-localized micro-extinction measurements. The SERS gain observed employing a 785 nm pump laser is particularly striking, making the sample interesting for bio-sensing applications with low fluorescence background. The large area self-organized SPP launching platform is very versatile since, by simply choosing the conductive film conformally grown of top of the rippled template, allows to tailor the plasmonic response in a wide spectral range extending from the near UV to the near IR, and possibly beyond considering the use of semiconducting materials.

6.3 Experimental

Sample fabrication

A soda-lime glass is heated up to 680 K, and irradiated with a defocused ion source (Ar^+) of energy of 800 eV at the incidence angle θ=30° with respect to the normal direction to the surface. During the ion irradiation process the glass surface is kept electrically neutral by exploiting the thermoionic electron emission from a tungsten filament negatively biased with respect to the sample at V_{bias}=-13 V. Under this condition highly ordered faceted nanopatterns with asymmetric faceted sawtooth profile can be achieved if the ion irradiation is prolonged for 1800 s at the pressure of 4×10^{-4} mbar (i.e. ion fluence of $1.4x10^{19}$ ions/cm^2). See section 1.2.3 of this thesis for more details. After the rippled pattern is formed on the glass surface, thermal Au deposition is performed on the rippled template at the pressure of about 10^{-5} mbar in the two step process described in the "results and discussion" section, to grow an Au thin film of approximately homogenous thickness on the slope modulated glass surface.

Morphology characterization

The rippled glass template morphology was characterized by means of the atomic force

microscope Nanosurf S Mobile. The average periodicity and slope of the glass ripples were computed from the statistical analysis of AFM topographies by means of WSxM software. Top view SEM images were acuired in back scattered electrons by a thermionic Hitachi VP-SEM SU3500, operating with15 kV accelarating voltage.

Optical characterization

For transmission measurement perfomed at normal incidence, the radiation emitted by a compensated deuterium-halogen lamp (DH-2000-BAL, Mikropak) is fiber-coupled to a linear polarizer and pinhole (with a diameter of 5 mm) acting also as a sample holder, placed at the focus of the optical beam. The polarization of the incoming light, incident on the back side of the sample, can be selected as parallel (TE-pol) or perpendicular (TM-pol) with respect to the Au NWs' long axis. A lens positioned at the opposite side of the sample, aligned with the illumination beam, focuses the radiation transmitted through the sample into a second optical fiber. Then, the signal is detected by a high-resolution solid-state spectrometer (HR4000 Ocean Optics) connected to a computer for the acquisition of the spectra. For non-normal incidence transmission measurements the sample is placed on a stage provided of a tilting movement and placed on the optical beam path using the same set-up described for the normal incidence case. All the titlted transmission spectra are normalized to the optical transmittance of a bare glass substrate tilted at the corresponding sample tilt.

SERS and co-localized extincion measurements

Samples (rippled Au/soda-lime glass and reference flat Au thin film on bare soda-lime glass) are kept in a 10^{-4} MB solution for an hour and the rinsed in de-ionized water for 10 minutes. SERS and optical micro-exticntion measurments are performed with a Horiba XploRA Nano. For SERS pump lasers of both 638 and 785 nm of wavelengt have been employed, using a 100 x objective. Micro-extinciton measurments have been performed co-locally switching the source to a polychromatic lamp illuminating the sample from below and switching to a 10x objective for signal collection.

References

(1) Han, Z.; Bozhevolnyi, S. I. Radiation Guiding with Surface Plasmon Polaritons. *Reports on Progress in Physics* **2013**, *76* (1), 016402. https://doi.org/10.1088/0034-4885/76/1/016402.

(2) Maier, S. A. *Plasmonics: Fundamentals and Applications*; Springer: New York, 2007.

(3) Zayats, A. V.; Smolyaninov, I. I.; Maradudin, A. A. Nano-Optics of Surface Plasmon Polaritons. *Physics Reports* **2005**, *408* (3–4), 131–314. https://doi.org/10.1016/j.physrep.2004.11.001.

(4) Wang, J.; Lin, W.; Cao, E.; Xu, X.; Liang, W.; Zhang, X. Surface Plasmon Resonance Sensors on Raman and Fluorescence Spectroscopy. *Sensors* **2017**, *17* (12), 2719. https://doi.org/10.3390/s17122719.

(5) Kalachyova, Y.; Mares, D.; Lyutakov, O.; Kostejn, M.; Lapcak, L.; Švorčík, V. Surface Plasmon Polaritons on Silver Gratings for Optimal SERS Response. *The Journal of Physical Chemistry C* **2015**, *119* (17), 9506–9512. https://doi.org/10.1021/acs.jpcc.5b01793.

(6) Anker, J. N.; Hall, W. P.; Lyandres, O.; Shah, N. C.; Zhao, J.; Van Duyne, R. P. Biosensing with Plasmonic Nanosensors. *Nature Materials* **2008**, *7* (6), 442–453. https://doi.org/10.1038/nmat2162.

(7) Neff, H.; Oliveira, L. C.; Rodrigures, E. P.; Thirstrup, C.; Lima, A. M. N. Enhanced Directed Radiative Surface Plasmon Emission from Periodically Corrugated Noble Metal Films. *Plasmonics* **2018**, *13* (6), 2021–2027. https://doi.org/10.1007/s11468-018-0718-2.

(8) Gillibert, R.; Sarkar, M.; Bryche, J.-F.; Yasukuni, R.; Moreau, J.; Besbes, M.; Barbillon, G.; Bartenlian, B.; Canva, M.; Chapelle, M. L. de la. Directional Surface Enhanced Raman Scattering on Gold Nano-Gratings. *Nanotechnology* **2016**, *27* (11), 115202. https://doi.org/10.1088/0957-4484/27/11/115202.

(9) Xu, Y.; Bai, P.; Zhou, X.; Akimov, Y.; Png, C. E.; Ang, L.; Knoll, W.; Wu, L. Optical Refractive Index Sensors with Plasmonic and Photonic Structures: Promising and Inconvenient Truth. *Advanced Optical Materials* **2019**, *7* (9), 1801433. https://doi.org/10.1002/adom.201801433.

(10) Dan'ko, V.; Dmitruk, M.; Indutnyi, I.; Mamykin, S.; Myn'ko, V.; Shepeliavyi, P.; Lukaniuk,

M.; Lytvyn, P. Au Gratings Fabricated by Interference Lithography for Experimental Study of Localized and Propagating Surface Plasmons. *Nanoscale Research Letters* **2017**, *12* (1). https://doi.org/10.1186/s11671-017-1965-4.

(11) Yu, C.-C.; Ho, K.-H.; Chen, H.-L.; Chuang, S.-Y.; Tseng, S.-C.; Su, W.-F. Using the Nanoimprint-in-Metal Method to Prepare Corrugated Metal Structures for Plasmonic Biosensors through Both Surface Plasmon Resonance and Index-Matching Effects. *Biosensors and Bioelectronics* **2012**, *33* (1), 267–273. https://doi.org/10.1016/j.bios.2012.01.021.

(12) Gao, L.; Lemarchand, F.; Lequime, M. Comparison of Different Dispersion Models for Single Layer Optical Thin Film Index Determination. *Thin Solid Films* **2011**, *520* (1), 501–509. https://doi.org/10.1016/j.tsf.2011.07.028.

(13) Giordano, M. C.; de Mongeot, F. B. Anisotropic Nanoscale Wrinkling in Solid-State Substrates. *Advanced Materials* **2018**, *30* (30), 1801840. https://doi.org/10.1002/adma.201801840.

(14) Berini, P. Long-Range Surface Plasmon Polaritons. *Advances in Optics and Photonics* **2009**, *1* (3), 484. https://doi.org/10.1364/AOP.1.000484.

(15) Inagaki, T.; Motosuga, M.; Arakawa, E. T.; Goudonnet, J. P. Coupled Surface Plasmons in Periodically Corrugated Thin Silver Films. *Physical Review B* **1985**, *32* (10), 6238–6245. https://doi.org/10.1103/PhysRevB.32.6238.

(16) M. Barelli, P.G. Gucciardi, F. Buatier De Mongeot, Large area blazed nanogratings for unidirectional Surface Plasmon Polariton excitation and SERS detection . *in preparation*

Conclusions

The focus of my PhD project consisted in the development of self-organized, large area, industrially scalable physical methods based on wrinkling instabilities to nanopattern and functionalize tunable plasmonic polymeric PDMS and solid-state glass surfaces, both transparent, non-toxic and cheap materials, for applications of significant technological interest in photonics and bio-sensing.

I achieved anisotropic wrinkling of PDMS polymer templates recurring to air plasma treatment on pre-stretched samples. The rippled templates are employed for the confinement of anisotropic, highly ordered, self-organized Au nanowires. For polarized light in the direction orthogonal to the NW long axis, Localized Surface Plasmon Resonance of both dipolar and multipolar nature are excited. The possibility to efficiently tune the Au structures LSPR into the infrared range of the spectrum due to retardation effects makes these flexible samples excellent candidates for biosensing application like e.g. in Surface Enhanced Raman Spectroscopy (SERS).

The wrinkling nanopatterning mechanism typical of soft organic matter can enhance the nanopatterning of solid state, inorganic glass subject to hot Ion Beam Sputtering (IBS) near their glass transition threeshold, providing excellent rigid nanorippled faceted templates for the large area confinement of plasmonic structures. I exploited these exceptional surfaces for different plasmonic functionalizations.

I engineered the confinement of plasmonic dimers on the nanorippled glass templates in the so called gap-plasmon configuration, showing magnetic dipole resonances with broadband tuning and subradiant features, by employing plasmon hybridization methods. The high sensitivity of the plasmonic resonances to small variations of dimers' morphology required a challenging precise control of the configuration parameters during the self-organized fabrication. To the best of my knowledge, this is the first demonstration of such capability obtained by a large-area, self-organized fabrication technique. Taking into account the potentials of the subradiant high-field-enhancement, plasmonic resonances for nonlinear nanospectroscopies and plasmon-enhanced photon harvesting in solar and photovoltaic cells, these findings pave the way for a further

development of the field.

I exploited the wrinkling enhanced faceted glass templates to confine anisotropic cross-polarized detuned plasmonic nanoantennas showing passive, broadband color routing capabilities. These large area metasurfaces exhibit highly directional and wavelength selective properties which are widely tunable and not related to complex and/or restrictive collective geometries and morphological parameters, greatly relaxing the fabrication demands and related critical issues. Since the scattering directivities of the proposed beam splitters are competitive with the figures of merit of lithographically patterned nanoantennas, these results can enable large-area, real world metasurfaces to be operated as flat optics broadband color routers, with potential impact on a wide range of applications from telecom photonics, to optical nanosensing.

I worked on the modification of the hot IBS soda-lime glass nanopatterning process to enable the engineering of short aligned Au nanorod arrays. Such functionalized surfaces show polarization-sensitive broadband plasmonic modes tuned across the Near- and Mid-IR spectral region (2500 cm^{-1} - 5000 cm^{-1}), resonant with the so-called *functional group window*. Under this condition superior Surface Enhanced Infra-Red Absorption (SERIA) sensitivity at the monolayer level over macroscopic sensor areas was demonstrated, with figures of merit competitive with lithographically made antennas.

I demonstrated how the enhanced IBS self-organized rippled soda-lime glass templates can operate as large area, subwavelenght, quasi-1D blazed gratings enabling the tunable excitation of propagating Surface Plasmon Polariton modes at the interface with thin conductive films (Au and Ag) conformally grown on top of them. A rippled Au/soda-lime grating sample showed remarkable SERS activity in the detection of methylene blue molecules. I demonstrated how the SERS gain is strongly correlated with the electric field enhancement produced by the excitation of counter-propagating SPP modes by comparing SERS and co-localized micro-extinction measurements.
Moreover, I obtained interesting preliminary results in the functionalization of the wrinkling-enhanced IBS rippled templates for plasmonic hot electrons mediated photocatalysis, for the guided growth of crystalline PLLA films and other interesting results in numerous external collaboration. These results however are not discussed in this thesis as still a work-in-progress.